Anisotropy of electron radiation damage in metal crystals

Peter Vajda

Equipe de Recherches du CNRS, Laboratoire de Chimie Physique, Universite de Paris—Sud, F—91405 Orsay, France

The principles of interaction of energetic electrons with atoms are reviewed with emphasis on effects due to the crystalline structure of the target. Computer "experiments" and analytic models that simulate the collision processes in a crystalline lattice are described and analyzed. The experimental part discusses, first, the techniques used for the investigation of point defects in single crystals. Then, the available experimental results on defect production and recovery in metal crystals are reviewed in detail, and basic information, such as threshold energies for displacement in the main crystallographic directions and electrical resistivities of Frenkel pairs, is extracted. Finally, it is shown how interatomic potentials can be deduced from the experimental results.

CONTENTS

INTRODUCTION

The problem of radiation damage in materials has become increasingly important during the past decade. It has been emphasized in conjunction with questions related to energy technologies, primarily with regard to fission and to fusion reactors, but also in the solar cell domain. In fact, the interaction of energetic particles with the solid materials in a reactor leads to their modification, which is often unwanted and sometimes prejudicial to its functioning: swelling of materials, void creation in them, embrittlement. The deleterious effects of radiation on devices has been a steady preoccupation of space technologists because of the sensitivity of semiconducting and insulating materials to structure defects. Another technological area experiencing practically exponential growth these days—ion implantation—is equally concerned with this problem. By bombarding a solid with an ion of an energy of 10^4– 10^6 eV one is not just implanting a chemical impurity in the material, but "doping" the latter at the same time with hundreds or thousands of lattice defects.[1]

At the same time, it has also become increasingly clear that, in order to understand the mechanisms of radiation damage in structural materials, one has first to obtain a realistic picture of the basic processes responsible for the production of point defects (vacancies and interstitials) by energetic radiation, and for their subsequent behavior. On the other hand, it is evident that the clearest information about the physical proces-

---

[1] There exist excellent reviews on these topics; among the most recent ones are Vook *et al.* (1975) and Dearnaley *et al.* (1973).

ses concerning these simple defects can be obtained by studying their comportment in monocrystalline materials, where the macroscopic physical properties reflect closely those on an atomic scale. This fact and the advent of new measuring techniques specific to single crystals, such as channeling, diffuse x-ray scattering, and high-voltage electron microscopy, are to a large extent responsible for the increasing interest shown in recent years in the study of radiation damage in monocrystals.

It is the physical aspect which I want to treat in some detail in this article, and I shall thus emphasize the experimental results contributing most to our knowledge of the fundamental processes in question. In restricting myself to the analysis of electron radiation experiments, I am already selecting this type of simple defect production, which is characteristic of electrons in the energy range of 10^5–10^6 eV; moreover, electrons are relatively easy to align into a narrow parallel beam, and their relatively low energy loss rate in materials (as compared with heavier charged particles) is a condition for uniform damage production across the thickness of a specimen such as is used, for example, in resistivity measurements. Furthermore, there exists a large body of data on electron radiation damage in polycrystalline material to which the single-crystal experiments provide the necessary complementary details, thus enabling a fruitful juxtaposition.

The restriction of the subject to metals is somewhat arbitrary, since the basic atomic displacement mechanisms are more dependent on the crystal lattice characteristics than upon the electronic structure of the material, although phenomena like ionization and bond breaking can also lead to the creation of point defects in ionic and semiconducting crystals, even when the energy of the impinging electrons is too low for a direct displacement. It is more in order to preserve a self-imposed coherence in the type of analyzed experiments that these latter materials shall be mentioned here only marginally.

Numerous conferences and books have been devoted to the description of radiation damage in solids. Several of the reviews in this field treat aspects of the subject covered in this article and are representative of the state of the art until the late 1960's (Chadderton, 1965; Corbett, 1966; Nelson, 1968; Thompson, 1969; Sosin and Bauer, 1969). Since that time, a considerable amount of new results have been obtained in several laboratories (in particular, at the KFA Jülich, and at Orsay), which—after a thorough analysis of the data—have made possible the construction of models for damage production in different crystallographic systems. Thus a restatement of the situation seemed desirable.

In the following paper, Sec. I reviews basic notions concerning the interaction of energetic electrons with an atom with emphasis on effects due to the crystalline structure of the target. Section II treats the computer "experiments" which simulate secondary collision processes in a crystal lattice. Here various analytic models trying to reproduce the computer data and early experimental results will also be described. Section III discusses the experimental techniques used in the study of defects in single crystals. Section IV presents the experimental results on defect production and the recovery of irradiated monocrystals; the whole section will be arranged according to the lattice structure of the metals, and corresponding models will be presented simultaneously. Finally, Sec. V deals with the application of experimental results for deduction of a basic parameter in radiation damage theory, the interatomic potential.

I. BASIC NOTIONS

In this section, I shall give the necessary background for an understanding of the processes which occur during the passage of energetic electrons through a crystalline specimen. These processes can be divided into two main groups:

(1) the interactions of the incident electrons with the target;
(2) the interactions of a lattice atom, which has received a certain kinetic energy and momentum in a collision with an electron, with its environment.

The first group of processes deals with inelastic and elastic collisions of incident electrons with target electrons and atoms, respectively; mention will also be made of radiative losses, which, however, are only important at higher electron energies. All these processes lead to modifications in the initially monoenergetic and unidirectional incident beam, such as energy loss and multiple scattering (straggling), and are treated as corrections to the principal problem of interest here: the interaction of the recoil atom with the neighboring lattice atoms [group (2) processes]. If the recoil energy of the knocked-on atom is high enough, exceeding a certain threshold T_d, it may end up in an interstitial position leaving a vacancy behind, thus becoming a displaced atom. It is at this moment that the specific characteristic of a crystal lattice, its discreteness, comes into play, leading to a directional dependence of T_d, which is eventually observed as anisotropy of the variation of some macroscopic physical property under irradiation.

A. The primary interactions

An incident electron loses energy during its passage through matter by collisions with target electrons, collisions with target atoms, and through radiation. The most important contributions are the ionization losses due to inelastic collisions with electrons. The stopping power for fast electrons with an initial energy E and for not too high energy transfers $\eta(\lesssim 10^5$ eV) is

$$-\frac{dE}{dx}(E)=\frac{2\pi e^4N}{\beta^2 m_0c^2}\left[\ln\frac{2\beta^2 m_0 c^2\eta}{(1-\beta^2)I^2(Z)}-\beta^2\right], \qquad (1.1)$$

where Z and x are the atomic number and the thickness of the penetrated matter respectively, N the total number of electrons per cm^3, I the average ionization potential of the target atoms, $\beta=v/c$, m_0 and e the rest mass and the charge of the electron, respectively. Landau (1944) has made an estimate of the electron energy distribution $L(x,E)$ for a beam of particles at the sample thickness x, from which it results that, for thin foils of thickness t, $L(t,E)$ is sufficiently narrow to allow the use of a mean electron energy at $x=t/2$

$$\bar{E}=E-(dE/dx)t/2\,. \tag{1.2}$$

In using expression (1.2), one has to apply a correction for multiple scattering due to small-angle elastic collisions with the target nuclei. This phenomenon tends, on the one hand, to increase the actual path length of the electron in the substance, and on the other hand, to widen the originally unidirectional beam into a cone whose opening angle depends on the electron energy and on the sample thickness, among other factors. The first problem can be settled by adopting an x_{eff} such that

$$x_{\mathrm{eff}}=x[1+(\delta/t)] \tag{1.3}$$

where the correction factor δ can be calculated using the work of Yang (1951) and Hebbard (1955). The second consequence of multiple scattering is more than just a correction [cf. Baranov (1972) and the comment on it, Vajda (1974)], as it is an essential feature of defect production in single crystals and tends to smear out particularities of the atomic displacement process (we shall come back to this later). The angular distribution of the electrons can be represented by a Gaussian (Mott and Massey, 1949)

$$P(\alpha)=(2/\pi\alpha)\exp(-\alpha^2/2\langle\alpha^2\rangle)\,, \tag{1.4}$$

where $\langle\alpha^2\rangle=2\theta_1^2\ln(65.3\beta\gamma\,\theta_1 Z^{-1/3})$ and $\theta_1^2=4\pi N_0 xZ^2e^4/m_0^2v^4\gamma^2$; N_0 is the number of atoms per cm^3 and $\gamma=(1-\beta^2)^{-1/2}$. To illustrate the importance of this effect, Table I presents the angular dispersion in the case of an actual experiment (Maury *et al.*, 1973a): 20μ thick specimens of Co, Zn, and Cd were irradiated with electrons of various energies, which had first passed through a 5.6-μ thick window of a Ni–Co alloy and through 2mm of He gas at the irradiation temperature (~5 K). One can see that bombarding a zinc or a cobalt specimen with electrons just above threshold (0.5 MeV) will cover practically all the crystallographic directions and thus obscure any expected anisotropy. In this sense, it can be more profitable to work with heavier elements, which have higher displacement thresholds, such as cadmium where $E_d\approx 0.6$ MeV. More examples are given in Fig. 1, computed by Bauer and Sosin (1966) for gold foils of various thicknesses and for two electron energies near the threshold of 1.4 MeV.

Simultaneously with ionization losses, fast electrons also lose energy through bremsstrahlung. For electron energies above a critical value E_{cr}, this mechanism becomes predominant. According to Bethe and Heitler (1934), the ratio A_{BH} between radiation and ionization losses is

$$A_{\mathrm{BH}}=\left(\frac{dE}{dx}\right)_r\Big/\left(\frac{dE}{dx}\right)_i\approx\left(\frac{Z}{1600}\right)\cdot\left(\frac{E}{mc^2}\right). \tag{1.5}$$

Thus the critical energy for aluminum ($Z=13$) is $E_{\mathrm{cr}}^{\mathrm{Al}}\approx 63$ MeV, that for molybdenum ($Z=42$)$E_{\mathrm{cr}}^{\mathrm{Mo}}\approx 20$ MeV. Hence one can neglect radiation losses for electrons in the range of 1 MeV, as has been done in this study.

TABLE I. Angular dispersion of electrons at different levels for $x_0=20$-μ thick specimens of Co, Zn, and Cd in degrees. Before hitting the samples, the beam passed through 5.6-μ Havar and through 2 mm He gas at 5 °K (Maury *et al.*, 1973a).

	Zinc			Cobalt			Cadmium		
E/MeV	0	$x_0/2$	x_0	0	$x_0/2$	x_0	0	$x_0/2$	x_0
0.7	9	14	18	8	14	18	10	17	24
0.5	11	18	23	10	18	24	14	24	31
0.4	14	22	28	13	22	29	17	29	38

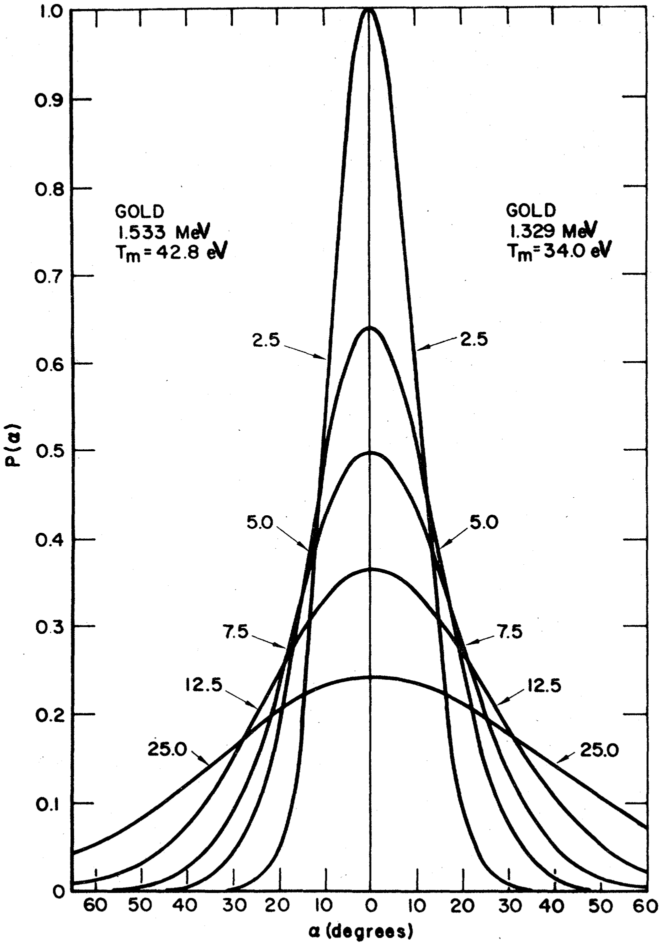

FIG. 1. Multiple-scattering distribution $P(\alpha)$ for gold foils of various thicknesses (numbers next to each curve, in μ) at electron energies of 1.533 MeV and of 1.329 MeV (Bauer and Sosin, 1966).

We shall next consider the elastic scattering process leading eventually to atomic displacement. From classical mechanics, taking into account the conservation laws of energy and momentum, one obtains a relation between ψ, the electron scattering angle, and θ, the atomic recoil angle (cf. Fig. 2)

$$\theta=(\pi/2)-(\psi/2)\,, \tag{1.6}$$

and

$$T=T_m\sin^2(\psi/2)=T_m\cos^2\theta \tag{1.7}$$

relating the energy transferred to the struck atom and the scattering angle. T_m is the maximum transmitted energy in a head-on collision.

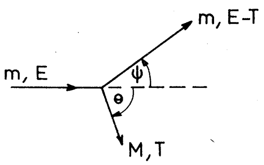

FIG. 2. The scattering of an energetic electron by an atom.

$$T_m = [4mM/(m+M)^2]E\,; \tag{1.8a}$$

which, in the case of electrons with $m \ll M$ and $E \ll Mc^2$, becomes

$$T_m = (560.8/A)\epsilon(\epsilon+2) \text{ in eV}\,, \tag{1.8b}$$

where A is the atomic mass and $\epsilon = E/mc^2$. To calculate the number of recoil atoms displaced after having received the energy T, we need the displacement cross section

$$\sigma_d(E) = \int_{\alpha_2}\int_{\varphi_2} d\Omega_2 \left(\int_{\alpha_1}\int_{\varphi_1} \left[\frac{P(\alpha_1)d\alpha_1 d\varphi_1}{2\pi} \right] \times \frac{d\sigma(T,E)}{d\Omega_2} p(T,\alpha_2,\varphi_2) \right) \tag{1.9}$$

in the polar system $\Omega_1 = (\alpha_1, \varphi_1)$ of the scattered electron and $\Omega_2 = (\alpha_2, \varphi_2)$ of the recoil atom. The relation between the recoil angle θ of Eq. (1.6) and $(\alpha_1, \varphi_1), (\alpha_2, \varphi_2)$ is

$$\cos\theta = \sin\alpha_1 \sin\alpha_2 \cos(\varphi_2 - \varphi_1) + \cos\alpha_1 \cos\alpha_2\,. \tag{1.10}$$

The cross section (1.9) contains the angular dispersion function $P(\alpha_1)$ from Eq. (1.4) normalized such that $\int_0^\pi P(\alpha_1)d\alpha_1 = 1$. For the differential cross section $d\sigma/d\Omega_2$ we can assume that, in the case of relativistic electrons, the interaction is practically Coulombian. This permits the application of Rutherford's formula

$$\frac{d\sigma}{d\Omega_2} = \left(\frac{d\sigma}{d\Omega_2}\right)_R = \left(\frac{Ze^2}{mc^2}\right)^2 \beta^{-4}\gamma^{-2}\cos^{-3}\theta\,. \tag{1.11a}$$

As a function of the transmitted energy T, this becomes

$$\frac{d\sigma}{dT} = \pi\left(\frac{Ze^2}{mc^2}\right)^2 \beta^{-4}\gamma^{-2} T_m^{-1}\left(\frac{T}{T_m}\right)^{-2}\,. \tag{1.11b}$$

Equations (1.11) are only valid in the classical limit. A quantum-mechanically rigorous treatment has been employed by Mott (1929; 1932), whose rather complex results can be approximated for light elements ($Ze^2/hc = Z/137 \ll 1$) following McKinley and Feshbach (1948) by multiplying Rutherford's cross section (1.11a) with a corrective function

$$\left(\frac{d\sigma}{d\Omega_2}\right)_{MF} = \left(\frac{d\sigma}{d\Omega_2}\right)_R B(\cos\theta)\,, \tag{1.11c}$$

where the correction function $B(y)$ is

$$B(y) = 1 - \beta^2 y^2 + \pi\frac{Ze^2}{hc}\beta y(1-y)\,. \tag{1.12}$$

For heavier elements, this approximation underestimates the exact Mott series; for numerical applications, one can use Oen's tables (1965), where the ratio of the Mott to McKinley–Feshbach cross sections is given for a large interval of scattering angles and energies.

From Eq. (1.11b) it follows that collisions with a small energy transfer are greatly favored (proportionality to T^{-2}), most electrons will lose only little energy, and their scattering will be strongly peaked in the forward direction. This is also seen from (1.11a) considering (1.6). Thus, in contrast to neutron irradiation, the *average* knock-on energy of the recoil atoms will be quite close to the displacement threshold, diminishing the role of multiple-defect creation.

B. The fate of the knock-on atom

The displacement cross section (1.9) introduced in the previous section contains one as yet undefined quantity: $p(T, \alpha_2, \varphi_2)$. Since this function depends only on the characteristics of the recoil atom (its energy and direction), we are thus abandoning the primary event and entering the field of secondary interactions engendered by the primary knock-on atom. The function $p(T, \alpha_2, \varphi_2)$ is simply the probability of an atom's having received the energy T in the direction (α_2, φ_2) to become displaced. It is most conveniently expressed in the form of a step function, so that

$$\begin{aligned} p(T,\alpha_2,\varphi_2) &= 0 \text{ for } T(\theta) < T_d(\alpha_2,\varphi_2) \\ &= 1 \text{ for } T(\theta) \geq T_d(\alpha_2,\varphi_2)\,. \end{aligned} \tag{1.13}$$

Here $T_d(\alpha_2, \varphi_2)$ is called the threshold energy surface for displacement and is the principal physical quantity needed for the determination of the cross section (1.9). In polycrystalline specimens, one obtains the observed probability by integrating the step function (1.13) over the space

$$P_d(T) = \frac{\int p(T,\alpha_2,\varphi_2)d\Omega_2}{\int d\Omega_2}\,. \tag{1.14a}$$

Computer simulations of the collision dynamics (discussed in more detail in the next chapter) have shown that $T_d(\alpha_2, \varphi_2)$ contained distinct minima corresponding to specific low-index crystallographic directions; this means that displacements occurred preferentially in these directions. Thus it was suggested that the function $P_d(T)$ could be reasonably well approximated by a finite sum of step functions:

$$P_d(T) = \Sigma_i\, p_i(T)\delta\Omega_i / \Sigma_i\, \delta\Omega_i\,, \tag{1.14b}$$

where the $\delta\Omega_i$'s are the solid angles around those low-index directions. The number i and the relative heights of the step functions were to be obtained by comparison with experiment.

1. Focusing

The low-index directions, which give minima in $T_d(\alpha_2, \varphi_2)$ as noted in the preceding section, are also the dense crystallographic directions of the lattice. Now, it had already been suggested rather early that energy and momentum transfer were particularly favorable along such dense directions. Silsbee (1957) was the first to show that, in the case of a linear row of atoms defined by their hard-sphere radius R and the interatomic spacing S, focusing collisions will occur when the angular ratio

$$\Lambda = \beta_{i+1}/\beta_i \leq 1\,. \tag{1.15a}$$

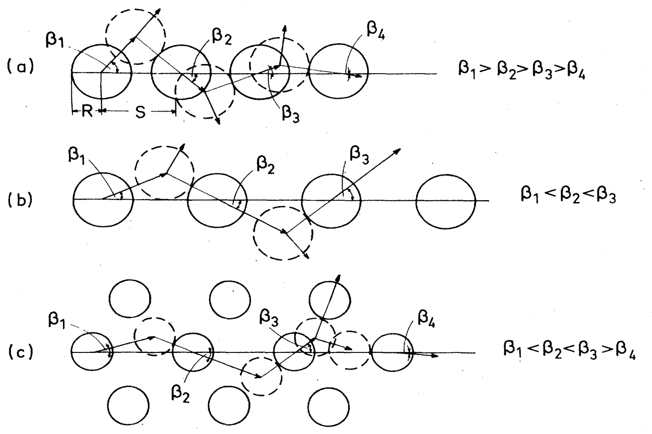

FIG. 3. (a) Focusing and (b) defocusing collisions in a linear row of atoms; (c) assisted focusing.

Figure 3 shows the situation for focusing and for defocusing. Equation (1.15a) can also be restated in terms of R and S, since the hard-sphere radius is defined through the potential as the distance of closest approach in a binary atomic collision and is thus energy dependent

$$\Lambda(E)=S/2R(E)-1\leqslant 1\,. \tag{1.15b}$$

One notes that focusing only occurs for not too high energies (several tens of eV), since $R(E)$ quickly becomes too small. For realistic collisions, the notion of a hard-sphere radius has to be modified, since the collision takes place before the actual "touching" of the atoms, due to the range of the interaction potential. Lehmann and Leibfried (1961) have treated this problem in the case of a Born–Mayer-type exponential repulsive potential of the form

$$V(r)=A\exp(-br) \tag{1.16}$$

and derived an expression for the correction distance Δ

$$\Delta=(2/b)\ln 2 \tag{1.17}$$

which depends only on the potential constant b, i.e., on the hardness of the potential.

Another form of directional collision is the so-called assisted focusing. Here one has to take into account also the neighboring rows of atoms, since they form a kind of lens system, which forces the propagating atom to remain in its sequence. Then, even if the focusing condition (1.15b) is not fulfilled, the fact that it will lose energy to a lens atom will eventually reduce its scattering angle β [Fig. 3(c)].

Focusing sequences are expected in the densest crystallographic directions: $\langle 110\rangle$ in the fcc lattice, $\langle 111\rangle$ in the bcc lattice, $\langle 11\bar{2}0\rangle$ in the hcp lattice; assisted focusing will be observed rather in loosely spaced directions such as $\langle 100\rangle$ for fcc, $\langle 100\rangle$ and $\langle 110\rangle$ for bcc crystals. Sometimes, as for example in the case of the $\langle 111\rangle$ row in a bcc lattice, pure Silsbee focusing is supported by assisted focusing due to close-lying atoms in neighboring rows. In systems with lower symmetry, as in an hcp crystal, one can have mixed lens effects leading to assisted focusing: when the propagating atom passes alternately through two different types of potential rings. Here, the atom does not stay in the same row, but moves in a slight zigzag around some mean direction. (More details will be given in Sec. III, when discussing the various displacement models.)

2. Multiple defect production

When the energy T received by the knock-on atom exceeds twice the threshold energy for displacement, $T>2T_d$, one can expect, in principle, to have more than one displaced atom as a result of one electron–atom collision event. Several authors have tried to calculate the number of displaced atoms as a function of transmitted energy $\nu(T)$. The most frequently employed model is that established by Kinchin and Pease (1955), in which the authors assumed the atomic collisions to be of a hard-sphere type and to occur statistically, i.e., independently of a crystallographic direction. They obtained the simple expression

$$\begin{aligned}\nu(T)&=0 \text{ for } T<T_d\,,\\ &=1 \text{ for } T_d<T<2T_d\,,\\ &=T/2T_d \text{ for } T>2T_d\,.\end{aligned} \tag{1.18}$$

For polycrystalline material and for not too high T, the estimate by Kinchin and Pease is fairly satisfactory. For large transmitted energies, as they occur in fast-neutron and in heavy-ion collisions, expression (1.18) seems to overestimate the actual defect density (cf. Lucasson, 1975), but this does not pose any problem in the electron energy range of interest here.

A more serious difficulty arises from the assumption that the threshold energy T_d is isotropic. As has already been mentioned in previous sections, the threshold energy surface is certainly not a simple sphere, but presents strong anisotropies around specific low-index directions. This could have consequences in the production of defects in monocrystalline material and is a problem which has not been tackled up to now. In fact, the difficulty here stems in part from the angular dispersion of the electrons: one might in a certain direction still be in the region $T<2T_d(\alpha_2^i,\varphi_2^i)$, but in another (easier) direction—with a smaller $T_d(\alpha_2^j,\varphi_2^j)$—be able to attain values where multiple defect production becomes effective. Hence the interest in near-threshold studies, since the correction for this effect does not exceed several percent for $T<(4\text{ to }5)T_d$.

II. DISPLACEMENT MODELS

A. Computer simulations[2]

1. Face-centered cubic lattice (Cu)

The first computer-simulated investigation of radiation damage events in a crystalline lattice was performed by Gibson *et al.* (1960) on copper. The atoms were allowed to interact with two-body, central re-

---

[2] An excellent review on the simulation of radiation damage in crystals has been published recently by V. M. Agranovich and V. V. Kirsanov, 1976.

pulsive forces represented by the Born–Mayer potential (1.16). Kinetic energies up to 400 eV were transmitted to lattice atoms and the corresponding equations of motion solved for a system of several hundreds of atoms.

Among numerous interesting results, such as the establishment of the interstitial split along a cubic axis of the lattice—the ⟨100⟩ "dumbbell"—as the stable interstitial configuration in the fcc system, and the existence of an orientation-dependent stability region for the Frenkel pairs—i.e., a nonspherical spontaneous recombination volume, the most important conclusions of this work were:

(a) Collision chains occurred in both ⟨110⟩ and ⟨100⟩ directions; the former correspond to the event predicted by Silsbee (1957), the latter to assisted focusing discussed in the previous section. The energy dependence of the focusing parameter Λ [Eq. (1.15)] was determined for both types of chains: ⟨110⟩ chains defocused above approximately 30 eV, ⟨100⟩ chains above ~40 eV. A chain with an energy above 25–30 eV carried both matter and energy and formed an interstitial atom near its end. Roughly 2/3 eV were spent per step in a perfectly focused ⟨110⟩ chain.

(b) The threshold energy for permanently displacing an atom was lowest (~25 eV) in or around the ⟨100⟩ direction, and very close to this value near the ⟨110⟩ direction. A much higher T_d, ~85 eV, was found for the ⟨111⟩ threshold. Thus the displacement probability $P_d(T)$ as defined through Eqs. (1.14) would rise from zero at 25 eV to unity at 85 eV. Figure 4 represents schematically the threshold energy contour for creating a stable Frenkel pair along the border of the fundamental triangle.

(c) Energy transfers near the threshold produced different types of Frenkel pairs, and it was suggested that it was, in principle, possible to correlate the substages of Stage I recovery with the annealing of these variously created pairs. Thus the close-lying values for $T_d\langle 100\rangle$ and $T_d\langle 110\rangle$ should imply that the relative number of distant (⟨110⟩ type) and close (⟨100⟩ type) Frenkel pairs would not depend much on the energy of the recoil.

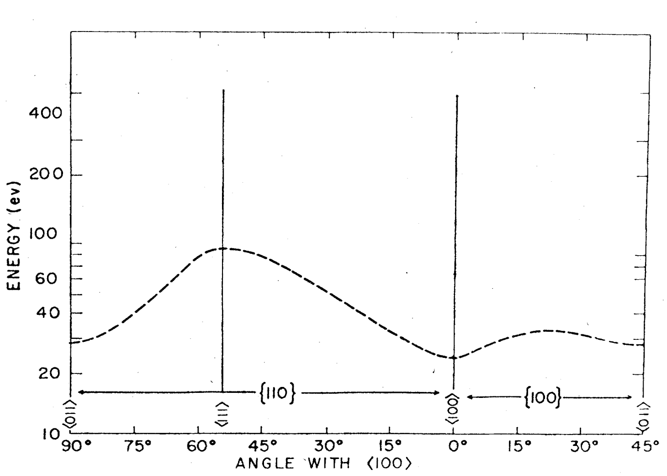

FIG. 4. Threshold energy contour in a copper lattice (Gibson *et al.*, 1960).

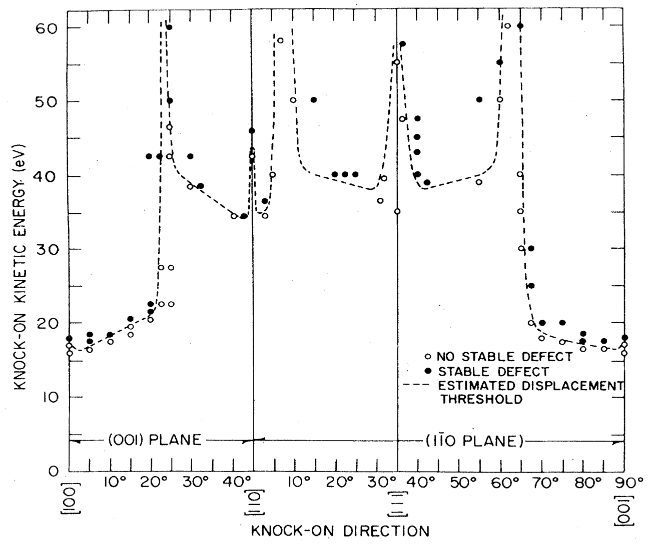

FIG. 5. Threshold energy contour in an α-iron lattice (Erginsoy *et al.*, 1964).

2. Body-centered cubic lattice (α-Fe)

Qualitatively similar results to those for copper were obtained in an analogous computer experiment by Erginsoy *et al.* (1964), who simulated collision events in an α-Fe lattice. Again, a Born–Mayer interatomic potential was used for the interactions; its parameters were fitted so as to match the experimental elastic constants of the metal.

As in the case of copper, the split interstitial configuration was found to be the stable one, but this time as a ⟨110⟩ dumbbell. Similarly, an anisotropic instability region around a vacancy was found, with maximum extension into the ⟨111⟩ directions.

Collision chains were prominent in the focusing ⟨111⟩ and the assisted ⟨100⟩ directions, the former having the smallest energy loss rate per step and the largest range. Focusing occurred below 28 eV for ⟨111⟩ chains, and below 18 eV for ⟨100⟩ chains.

A highly anisotropic displacement threshold energy was deduced from the calculations. As is clearly shown by Fig. 5, deep and wide minima of 17 eV occur around the ⟨100⟩ directions, while two other, shallower minima (34 and 38 eV) are found in a ring a few degrees off the ⟨110⟩ and the ⟨111⟩ directions. Figure 6 gives a view of the threshold energy surface across the stereographic triangle showing the shape and the size of the principal displacement "windows." As a consequence of these results, the integrated displacement probability function rises in two steps, beginning from zero at 17 eV up to ~1/3 at 34 eV, then, taking into account the contributions of the ⟨110⟩ and ⟨111⟩ processes, in a second step until ~2/3, and reaching unity only at higher transmitted energies.

Thus the main difference between the fcc and the bcc lattices as concerns the displacement processes seems to be that the threshold energy surface in bcc lattices contains minimum regions of two different displacement thresholds, while in fcc copper the depth of the minima was comparable. The resulting two-step $P_d(T)$ function

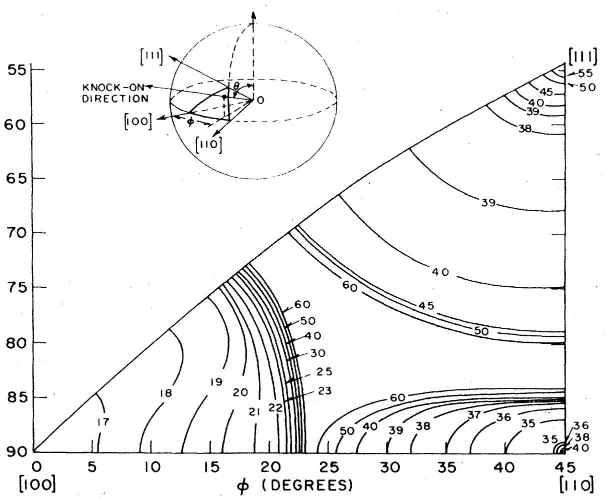

FIG. 6. Threshold energy surface in α-iron in the fundamental triangle (Erginsoy *et al.*, 1964).

is its experimental expression. This phenomenon and its relation to the lattice symmetry will be discussed in connection with the experimental data presented in Sec. IV.

Until now, collision dynamics have been discussed assuming, as an initial condition, an ideal positioning of the atoms at their lattice sites, i.e., at a hypothetical 0°K temperature. Thermal vibrations leading to a perturbation of the lattice regularity should tend to uniformization of the displacement mechanisms and to sphericalization of the threshold energy surface. For bcc α-iron, Agranovitch and Kirsanov (1970) have performed such a calculation including thermal displacements of the atoms and taking into account the spatial correlation between them; the investigated temperature interval was 0 to 848 K. For a rigid lattice, the authors reproduced Erginsoy's results, in particular as concerns the energy-dependent collision chain ranges in the directions $\langle 111\rangle$ and $\langle 100\rangle$. Taking into account the quantum-mechanical zero-point vibrations at 0 K already changes considerably the energy loss mechanism: more energy is dissipated per collision during the initial phase, thus reducing the chain length. Figure 7 shows the situation for an initial knock-on energy of 50 eV in the two principal chain directions and at different temperatures. Though for the higher temperatures the results are not significant, since the model does not consider any annealing processes and is thus not compatible with a realistic experiment, it appears clearly that the thermal vibrations do smear out the effects of lattice anisotropy. The threshold energies for displacement in the $\langle 100\rangle$ and $\langle 111\rangle$ directions at 0 K, taking into account zero-point vibrations, were computed by the authors to $T_d\langle 100\rangle = 18$ eV and $T_d\langle 111\rangle = 26$ eV, i.e., closer to each other than those at a hypothetical 0 K (17 and 34 eV, respectively).

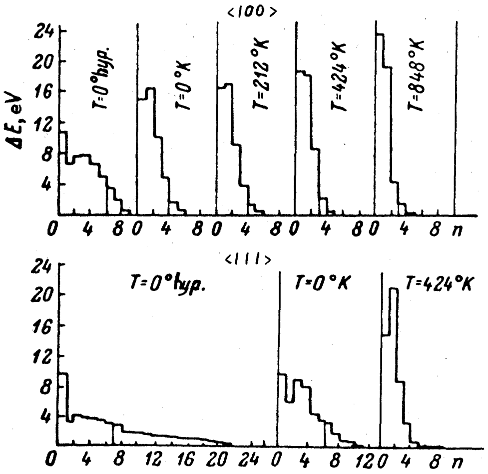

FIG. 7. Energy loss rate per collision step of a 50 eV knock-on in a $\langle 100\rangle$ and in a $\langle 111\rangle$ chain, as a function of crystal temperature (Agranovich and Kirsanov, 1970).

3. Composite structures

In this section, I shall briefly mention the results of the computer simulations performed by Chadderton and Torrens (1965) in various structures, with attention to the observation of ordered collision phenomena.

a. Potassium chloride

This alkali halide lattice is a face-centered cubic structure with singly charged potassium and chlorine ions situated alternately at the lattice points of a simple cubic lattice, and is typical for ionic binding. The ions are close-packed, thus in principle favoring focusing collision chains. Indeed, strong assisted focusing in the $\langle 110\rangle$ direction was observed for a 80 eV potassium ion in the (100) plane, while $\langle 100\rangle$ focusing occurred too, but was much less intense.

b. Lead iodide

This lattice is characterized by a certain amount of covalent binding; it possesses hexagonal structure and consists of sandwiches of planes parallel to the basal (0001) plane, each sandwich being composed of a plane of lead atoms squeezed between two planes of iodine atoms. The atomic packing is somewhat looser than in KCl. For a knocked-on lead atom (80 eV) in a $(11\bar{2}0)$ plane, there was strong assisted focusing (due to two iodine atoms) in the $\langle 10\bar{1}1\rangle$ direction and some additional assisted focusing in the $\langle 0001\rangle$ direction; the latter was rather short ranged due to the asymmetry of the adjacent-atom lenses.

B. Analytic models

1. Threshold energy surfaces

From the computer experiments, as well as from simple geometrical symmetry considerations, it followed quite naturally that one could try to construct a threshold energy surface based on a few fundamental displacement mechanisms. Soon after Silsbee's (1957) discovery of the preferential propagation of energy along dense lattice directions it had been proposed to attribute the observed experimental threshold energies to displacements into such "easy" directions. The first attempt to treat the problem analytically was

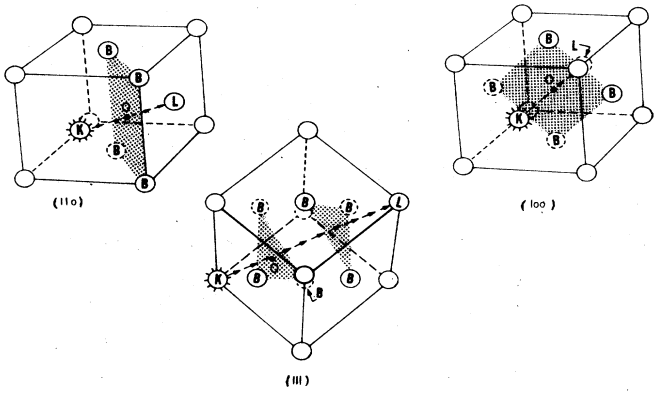

FIG. 8. Diagram of the three fundamental ejection processes in an fcc lattice showing the lenses formed by the ring atoms B on the path of the knock-on atom K (Sosin, 1962).

undertaken by Sosin (1962), who had extended Leibfried's work (1959) on focusing chains to include a calculation of the displacement cross section [Eq. (1.9)]. He considered displacements in the three ejection directions ⟨100⟩, ⟨110⟩, and ⟨111⟩ in an fcc lattice and applied the calculations to copper. The geometry of the displacement processes is illustrated in Fig. 8: the atom K, after having received momentum from the incoming electron, is projected across different lenses formed by the ring atoms B towards the atom L. The collision processes between atoms K and B are treated in the impulse approximation using central forces between them given by the gradient of a Born–Mayer potential of the form (1.16). The energy lost to a B-type atom is

$$\epsilon_0 = (\pi/2) r b (A^2/T) \exp(-2rb) , \qquad (2.1)$$

where r are the center-to-atom distances in the respective lenses. The total energy T_1 lost to the ring is, therefore, $T_1\langle 100\rangle = 4\epsilon_0\langle 100\rangle$, $T_1\langle 110\rangle = 4\epsilon_0\langle 110\rangle$, and $T_1\langle 111\rangle = 3\epsilon_0\langle 111\rangle$, respectively. In the more general case, when the atom K initially makes an angle β with the main crystallographic directions, expression (2.1) has to be modified; for instance, for displacements around a ⟨110⟩ axis, it becomes

$$\epsilon_\beta\langle 110\rangle = \epsilon_0\langle 110\rangle \cosh[(2/\sqrt{3})ab\tan\beta] \qquad (2.2)$$

with a as half the distance between the atoms K and L. The collision between K and L is nearly a head-on collision, and is calculated by a simple two-body, hard-sphere approach, with an energy-dependent hard-sphere radius (cf. Sec. I.B.1)

$$R = (1/2b)\ln(2A/T_2) , \qquad (2.3)$$

where T_2 is the energy transferred to atom L. The sum of $(T_1 + T_2)$ is then the threshold energy for displacement. Instead of using a certain R for the calculation of T_2, Sosin adopted a T_d in the experimentally established range for copper, 17 to 22 eV, and deduced a $T_2 = T_d - T_1$ from it, thus determining R. He then integrated the cross section (1.9) as a function of transferred energy T (using the potential of Gibson, 1960), in particular in a cone around the 12 ⟨110⟩ directions, assuming them to be the directions of minimum T_d. (The probability function P_d contained in the cross section was constructed using spherical geometry around ⟨110⟩.) A comparison of the obtained set of cross sections with existing polycrystal data on copper restricted the possible choice, yielding a best fit with $T_d = 19$ to 20 eV. Despite the fact that other displacement mechanisms were neglected, especially the ⟨100⟩ displacements, which also have a low T_d (Gibson, 1960), the fit was quite satisfactory, indicating the predominance of the ⟨110⟩ processes.

A further extension of this approach was undertaken by Jan and Seeger (1963), who treated the full angular space of an fcc crystal. They calculated displacement cross sections using a threshold energy surface in the form of a cubic harmonic of the sixth order

$$\begin{aligned} T_d(\theta,\varphi) = {} & (2T_{110} - T_{100}) + 2(T_{100} - T_{110}) \\ & \times [\sin^4\theta(\cos^4\varphi + \sin^4\varphi) + \cos^4\theta] \\ & + 9(T_{100} - 4T_{110} + 3T_{111}) \sin^4\theta \cos^2\theta \sin^2\varphi \cos^2\varphi \end{aligned} \qquad (2.4)$$

putting the axis $\theta = 0$ in the ⟨100⟩ direction and using T_{100}, T_{110}, and T_{111}—the threshold energies in the three main crystal directions—as parameters. They were able to fit experimental polycrystal data on copper using two different sets of thresholds: (a) $-T_{100} = 14.7$ eV, $T_{110} = 30.6$ eV, $T_{111} = 70.3$ eV, or (b) $-T_{100} = 34$ eV, $T_{110} = 15.0$ eV, $T_{111} = 52.1$ eV. It is interesting to note that in both cases the minimum T_d is ~15 eV, but that in the first case $T_d^{\min} = T_d\langle 100\rangle$ and in the second case it is $T_d^{\min} = T_d\langle 110\rangle$. For both fits, the threshold in the second principal direction was about twice $T_d^{\min}$. This is a serious difficulty; moreover, it is in contradiction with both the computer results of Gibson *et al.* (1960) and with recent single-crystal experiments (Jung *et al.*, 1973; cf. also Sec. IV), who gave $T_d\langle 110\rangle \approx T_d\langle 100\rangle$. Furthermore, it was not possible to obtain a reasonable fit with expression (2.4) to single-crystal results on the bcc metals tantalum (Jung and Schilling, 1972) and molybdenum (Maury *et al.*, 1975), although it should, in principle, be applicable to any crystal with cubic symmetry. Evidently, the cubic harmonic is an

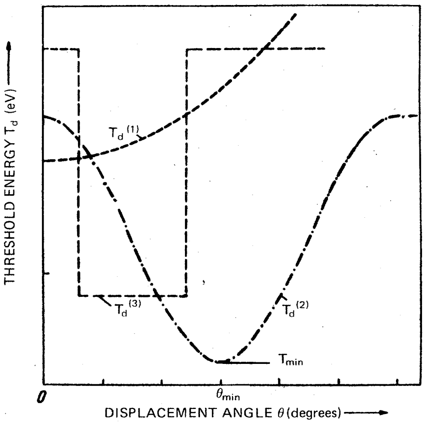

FIG. 9. Various types of threshold energy surfaces in the vicinity of the ⟨110⟩ axis in an fcc crystal (see text) (Wollenberger and Wurm, 1965).

inadequate description of the T_d surface.

One can try to refine the method used by Jan and Seeger (1963) by modifying their smooth T_d surface through the introduction of additional structures. This was done by Wollenberger and Wurm (1965), who took into account the computer findings of Erginsoy *et al.* (1964) concerning the singularities in the symmetry axes ⟨110⟩ and ⟨111⟩, with minima in their immediate neighborhood (cf. Fig. 5). The displacement cross section σ [Eq. (1.9)] was calculated using the variously shaped threshold energy surfaces depicted in Fig. 9. $T_d^{(1)}$ is a parabolically increasing function and is representative for a smooth shape analogous to that of Jan and Seeger (1963). The two others possess a minimum close to a main axis: $T_d^{(2)}$ is a $\cos^2$ function and can be described by

$$\left.\begin{aligned} T_d^{(2)} &= (T_{\max} - T_{\min})\cos^2\left(\frac{\pi}{2}\,\frac{\theta}{\theta_{\min}}\right) + T_{\min} && \text{for } \theta \leqslant 2\theta_{\min} \\ T_d^{(2)} &= \text{const} = T_l && \text{for } \theta \geqslant 2\theta_{\min} \end{aligned}\right\} \tag{2.5}$$

$T_d^{(3)}$ is a square-well function. It was found that the cross sections were only slightly dependent on the absolute value of $T_{\max}$ but very strongly on the value of $\theta_{\min}$: increasing $\theta_{\min}$ from 12° to 15°, e.g., in copper, led to an increase of σ by about 50% near its maximum. Using a function of the type of $T_d^{(2)}$ or $T_d^{(3)}$, Wollenberger and Wurm were able to reproduce the experimental data of Bauer and Sosin (1964), who had found a very low threshold in copper (~10 eV) and had explained it by subthreshold collision events (see Sec. IV for details).

The multiple scattering in a realistic crystal with non-negligible thickness tends to smear out the effect of the singularities discussed by Wollenberger and Wurm (1965), especially for energies near the threshold. Their experimental observability, therefore, remains questionable. This induced Gettys (1966) to go back to a simple form of the T_d surface with the minima along major crystallographic axes. He confined himself to near-threshold collisions and gave his surface the form

$$T_d(\theta) = T_0 + C\sin^2\theta\,, \tag{2.6}$$

where T_0 is the threshold in the direction of the selected symmetry axis ($\theta = 0°$). Here C is a parameter describing the displacement energy in the vicinity of a limiting cone with an angle θ_0 for which displacement is still possible; C will be roughly $T_{\max}$, which defines θ_0 through $\sin^2\theta_0 \approx 1 - T_0/T_{\max}$. The simplicity of Eq. (2.6) makes possible the calculation of the displacement cross section σ_d, but comparison with experiment is limited due to the restriction to energies close to the threshold (cf. also the discussion of copper data in Sec. IV).

2. Focusing collisions

A certain amount of information about the threshold energies for displacement can be drawn from calculations of the focusing condition (1.15), if one assumes that interstitial transport occurs mainly in correlated collision chains. Besides the threshold energy, such calculations yield information on the number of collision chains produced by a primary knock-on, and on their range, which can be of importance for the production of interstitials outside displacement cascades, the production of defects at dislocations, etc. Details will not be gone into here; I shall only refer to work in this direction accomplished by Leibfried (1959) on fcc crystals and to Balarin's 1962 investigation of hexagonal graphite. The influence of thermal vibrations on focusing was treated by, among others, Sanders and Fluit (1964) and Pugatcheva (1967).

III. EXPERIMENTAL METHODS

A. Electrical resistivity

Most experimental observations of electron radiation damage in metallic crystals have been made by the classical method of measuring the variation of the residual electrical resistivity due to the introduction of defects. The experimental irradiation conditions—thin specimens (≤20 to 30 μm) to reduce multiple scattering of the electrons, and low irradiation temperatures (in the liquid helium range) to avoid recovery due to thermal migration of defects—are also favorable for the performance of precise residual resistivity measurements. One disadvantage is that, for thin and pure specimens, one has to take into account the size effect in conduction-electron scattering, the correction for which is not always simple, due to the lack of experimental knowledge of the electron mean free path (for details and numerical tables see Dworschak *et al.*, 1967, 1969).

In an isotropic material and at low enough temperatures, the resistivity change rate per incident particle is proportional to the energy-dependent cross section $\sigma(E)$

$$\Delta\rho(E)/n = \rho_F\sigma(E)\,. \tag{3.1a}$$

Here, the proportionality factor ρ_F is the characteristic resistivity of a unit concentration of Frenkel pairs and is *per se* an important physical property, of interest to determine; n is the electron fluence, hence the product $n\sigma(E)$ represents the concentration of created Frenkel pairs.

In a single crystal, with an *a priori* anisotropic cross section $\sigma_i(E)$, one obtains

$$\Delta\rho_i(E)/n = \rho_F\sigma_i(E)\,, \tag{3.1b}$$

where the index i stands for a specific crystallographic direction. The experimental procedure consists in irradiating thin single-crystal foils oriented parallel to a chosen crystal plane along a certain direction ⟨i⟩ and in measuring the corresponding $\Delta\rho_i(E)$ as a function of the electron energy E. Assuming a fixed value for ρ_F, which—in a first approximation—is supposed to be orientation independent, one obtains directly the cross sections $\sigma_i(E)$. [In highly anisotropic material, e.g., hexagonal metals with a large c/a ratio (Zn, Cd) one should rather avoid placing the contacts in such a way that the measuring current passes along a particularly "singular" direction like the c axis.] From Eq. (1.9) and considering (1.13) one can thus, in principle, calculate the threshold energy $T_d\langle i\rangle$ in the direction ⟨i⟩. A simpler way is to assume a "reasonable" shape for $T_d(\theta, \varphi)$ deduced from lattice symmetry considerations, to compute the corresponding $\sigma(\theta, \varphi)$, and to compare these latter quantities with the experimentally determined $\Delta\rho_i$, where $\langle i \rangle = (\theta, \varphi)$. The parameters of $T_d(\theta, \varphi)$ can than be obtained from the best fit with experiment. Because the displacement probability, unlike that in polycrystals, is no longer a parameter (with an energy-dependent step height), but reaches unity as soon as $T \geq T_d$ [Eq. (1.13)], one immediate result of the above fit is a numerical value for ρ_F.

Additional information can be drawn from the study of the low-temperature annealing of the electrical resistivity change. Recovery during Stage I is supposed to be due to a self-interstitial atom's annihilating with its own vacancy (Frenkel-pair recovery) or with another one (recovery of a freely migrating interstitial). Thus, observations of how the recovery substages of Stage I vary as a function of the sample orientation and of electron energy can lead to conclusions concerning the special type of collision mechanism responsible for the defect which is annealing in the substage in question.

B. High-voltage electron microscopy

One method of observing directly the introduction of defects into crystals is high-voltage electron microscopy. If the electron energy is high enough, isolated vacancies and interstitials are produced; if they have sufficient mobility they will migrate and either annihilate at various sinks (and by recombination) or agglomerate into clusters. When these clusters attain a certain minimum size (in general, a few tens of Å) they become visible; by varying the microscope voltage one can determine the threshold energy for their appearance and relate it to the threshold energy for interstitial formation. Irradiation of single-crystal specimens perpendicular to specific crystal planes will thus give information on a possible anisotropy of the defect production mechanisms.

An advantage of electron microscopy is the use of very thin foils (~ 1000 Å), permitting a uniform damage distribution through the thickness even at the lowest near-threshold energies, and avoiding the problem of multiple electron scattering. A disadvantage is the relatively high dose needed to create visible clusters; this and the fact that one deals with secondary defects formed by agglomeration of the primary point defects, creates some problems for the interpretation of the data. In fact, early experiments, which had been performed at room temperatures, were interpreted through the thermal migration of interstitials to form interstitial clusters and then loops. With the advent of liquid helium stages in microscopy one began to observe clusters when defect migration due to thermal activation was no longer possible; this led to a reformulation of the model so as to consider at high defect concentration the statistical overlapping of the interaction volumes of like defects, as well as to take into account dynamic processes resulting from the collision event when interstitials meet to form clusters (Urban, 1972). Very recent observations of both interstitial and vacancy clusters well below the respective migration temperatures (Urban and Seeger, 1974; Urban and Jäger, 1975) are attributed to radiation-induced diffusion of point defects *during* the electron irradiation itself.

C. Diffuse x-ray scattering

A very important contribution to our knowledge about point defects has been made by the Jülich group headed by W. Schilling, who have applied the technique of diffuse x-ray scattering for their investigations (a good survey of this method is given by Ehrhart, Haubold, and Schilling, 1974). Assuming a statistical distribution of defects and linear superposition of the strain fields around the defects (low defect densities), the diffuse scattering intensity is proportional to the defect concentration c and to the square of the scattering amplitude $F(\mathbf{k})$, where $\mathbf{k}$ is the scattering vector:

$$S_{\text{diff}} = c\,|F(\mathbf{k})|^2 . \tag{3.2}$$

Here $F(\mathbf{k})$ is called the "defect structure factor" and consists of two contributions: one is the scattering factor of the defect itself, the other is due to the displacement field around the defect; it is thus very typically dependent on the defect structure. By measuring the angular distribution of S_{diff} at low temperatures one can determine the structure of interstitial atoms in an irradiated crystal. (The vacancy contribution to the scattering can be corrected for relatively easily, assuming that the vacancy structure is well known and that the strain field around it is much smaller than that around an interstitial.) This technique has allowed an unambiguous determination of the dumbbell as the stable interstitial configuration in various fcc, bcc, and hcp metals (Ehrhart, 1975).

In the context of this article, we are primarily interested in the possibility of determining, by means of this method, the absolute concentration of Frenkel pairs and hence the Frenkel-pair resistivity ρ_F [Eq. (3.1)]. In fact, near the lattice vectors in the reciprocal space, $\mathbf{k} \approx \mathbf{h}$ (Huang scattering), the structure factor $F(\mathbf{k})$ becomes proportional to the elastic displacement field around the defect, which can be described by the dipole force tensor P_{ij}. It follows that the Huang intensity is proportional to the square of P, where $P = \mathrm{Tr} P_{ij}$ characterizes the defect strengths

$$S_{\text{Huang}} \propto cP^2 . \tag{3.3}$$

The quantity P also determines the lattice parameter change; in a cubic crystal one has

$$\Delta a/a = \tfrac{1}{3}\Delta V/V = cP/[3V_c(C_{11} + 2C_{12})] , \tag{3.4}$$

where $\Delta V/V$ is the corresponding volume change, V_c the atomic volume, and C_{11}, C_{12} are elastic constants. Hence one obtains linear proportionality

$$\Delta a/a \propto cP . \tag{3.5}$$

From (3.3) and (3.5) we see that simultaneous measurements of S_{Huang} and $\Delta a/a$ yield an absolute value for c. It follows then immediately from Eq. (3.1) that the measurement of the residual resistivity increment $\Delta\rho$ gives a value for ρ_F

$$\rho_F = \Delta\rho / n\sigma = \Delta\rho / c \,. \tag{3.6}$$

Further defect characteristics which can be obtained from a combination of measurements of diffuse x-ray scattering and of lattice parameter changes are the volume changes $\Delta V_i / V_c$ and $\Delta V_v / V_c$, due to the introduction of an interstitial or a vacancy, respectively (for details see Ehrhart, Haubold, and Schilling, 1974).

D. Elastic properties

Some relatively indirect evidence for anisotropy of defect creation under irradiation can be drawn from internal friction experiments. For example, in a dislocation damping experiment one measures the ultrasonic attenuation in a crystal. According to Granato and Lücke (1956), dislocations can be treated as strings of a length L vibrating in a viscous medium under an applied oscillatory stress of a frequency f. Then the logarithmic decrement Δ can be expressed as

$$\Delta = K 2\pi f \tau / [1 + (2\pi f)^2 \tau^2] \,, \tag{3.7}$$

where both K and τ are proportional to L^2. A $\log\Delta(\log f)$ plot of Eq. (3.7) describes the frequency dependence of the damping; it exhibits a maximum which shifts as K and τ vary with irradiation conditions. This maximum, Δ_m, and the frequency, f_m, at which it is observed are directly related to K and τ^{-1}, respectively. Thus by determining K and τ for an unirradiated crystal and for a crystal after irradiation along various orientations one obtains the variation of the dislocation length L. In fact, L will decrease with radiation due to the introduction of point defects which act as pinning centers on the dislocation lines and immobilize them. The density of these pinning centers per cm^3 is then Λ / L, where Λ is the dislocation density per cm^2. The problem with this type of experiment is the need to use bulk crystals for the internal friction measurements, thus excluding electrons as incident particles for anisotropy studies because of beam straggling and absorption. Gamma rays can, in principle, be used when collimated, but one has to employ very strong gamma sources, since the interaction with the crystal atoms and the resulting defect density is rather small. Moreover, the interaction occurs mainly through secondary Compton electrons, which do not have one defined energy and are themselves subject to multiple scattering.

Another type of internal friction measurement using the orientation dependence of the relaxation peaks associated with interstitials (low-frequency experiments) gives valuable information on the strain field around an interstitial and, through this, on its configuration. The evolution of this strain field during annealing can give an indication of the mechanisms acting during thermal recovery. (Interesting examples of such an analysis were given in a review talk by Okuda, 1975.)

Similarly, investigations of the elastic aftereffect can provide insight into the structure of defects. By measuring the growth and decay of the anelastic strain $\Delta\epsilon$, produced by the relaxing defects in an irradiated crystal during application and after removal of a constant stress, one can determine the relaxation strength $\Delta^* \equiv \Delta\epsilon / \epsilon_0$ (ϵ_0 is the instantaneous elastic strain) and the time constant τ for defect relaxation at various temperatures. (For a description see Spirič, 1975.) The study of relaxation in differently oriented crystals irradiated below Stage I recovery provides information about the symmetry of the interstitial; its temperature dependence provides information about the defect evolution.

E. Magnetic anisotropy

In magnetic materials, one can use still other methods for the study of the defect symmetry. A general survey has been given by Dautreppe (1969), so I shall only mention here a technique developed recently by Forsch (1970) and applied to single crystals. If one places a single-crystal disc in a static magnetic field **H** strong enough to suppress its domain structure, and lets it rotate so that the axis of rotation is perpendicular to the field, one will receive a signal in a pickup coil. This is due to the fact that the crystal anisotropy tries to align the magnetization vector **M** in the easy direction, while the external field tries to align it along the field direction, thus giving rise to an oscillation of **M** around **H**. Introduction of anisotropic defects in the specimen leads, in principle, to an increase of anisotropy. Although this variation is rather small, it can be separated from the crystal anisotropy by preferentially aligning the defects through a magnetization of the specimen parallel to one of the anisotropy axes of the defect. Varying the magnetization direction with respect to the crystal axes will vary the amplitude of the pickup signal and provide information about the defect orientation.

IV. EXPERIMENTAL RESULTS

A. Damage production

1. Face-centered cubic lattice

a. Copper

The early studies of defect production in metal crystals were all done on copper. The first results were reported by Bauer and Sosin (1964), who investigated the electron energy dependence of the resistivity change rate in samples of different orientations. Figure 10 shows their results for crystals irradiated perpendicularly to the (100) and to the (110) plane, respectively. The observed anisotropy lies within experimental error, and the principal feature is the tail at low energies giving an apparent threshold at ~10 eV. This is much lower than predicted by the computer experiments and also than determined through measurements on polycrystals: 15 to 20 eV (Lucasson, 1961, Sosin 1962). Although—after a thorough analysis of several possible mechanisms—the authors attributed the low T_d to subthreshold displacements via interaction of a focuson with a light impurity atom (they had proposed beryllium), it was tempting to see here a manifestation of some particular displacement mechanism characteristic of the copper lattice itself. Thus Wollenberger and Wurm (1965) suggested a special form of the threshold energy surface with a minimum of 9 eV near the ⟨110⟩ axis to fit the data of Bauer and Sosin (cf. Fig. 11). Indeed, as will be

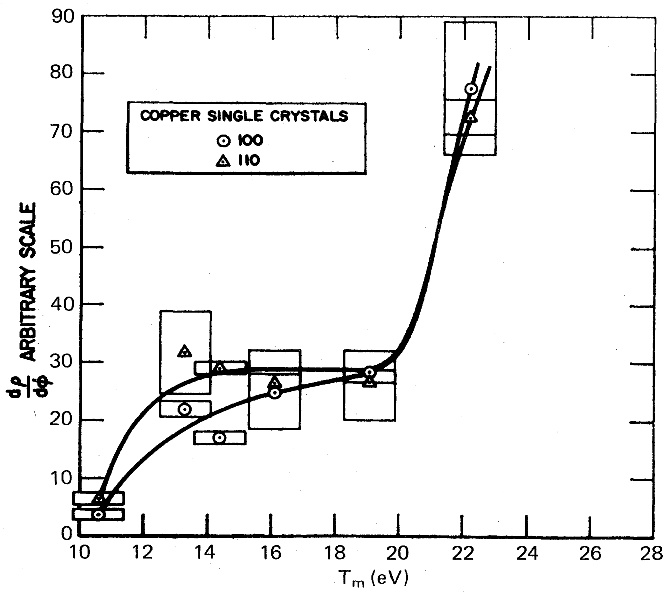

FIG. 10. Resistivity change rates for two copper crystals as a function of the maximum recoil energy to a Cu atom (Bauer and Sosin, 1964).

shown below, later detailed investigations (Jung *et al.*, 1973) have indicated a threshold energy minimum off the ⟨110⟩ direction, but this relatively shallow minimum ($T_d = 19$ to 21 eV) rather lends support to the indirect mechanism proposed by Bauer and Sosin (1964) for their low T_d (see also the discussion by Bauer and Sosin, 1966).

The first studies really devoted to a search for anisotropy in defect production predicted by the computer model of Gibson *et al.* (1960) were the experiments by Kamada *et al.* (1964) and by Sosin and Garr (1965). Kamada and co-workers (1964) irradiated specimens with orientations near the ⟨110⟩ and ⟨111⟩ directions and observed a crossing of the damage-rate curves (Fig. 12).

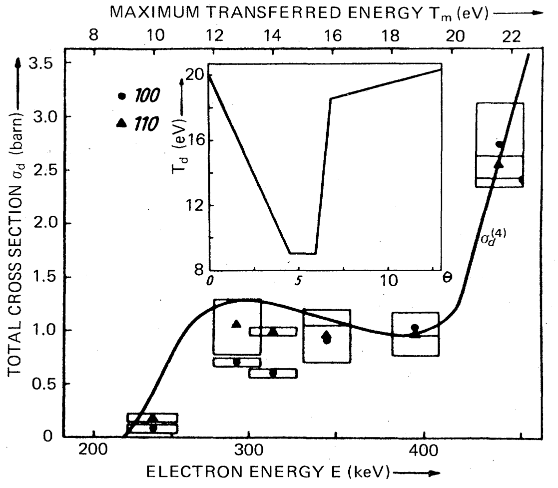

FIG. 11. Displacement cross section as a function of energy for the T_d surface given in the insert, fitting the experimental results by Bauer and Sosin (1964) for copper (Wollenberger and Wurm, 1965).

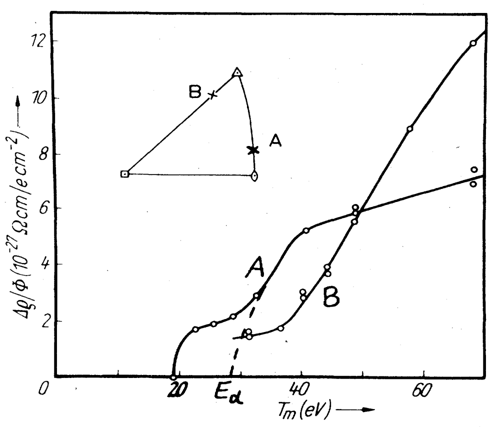

FIG. 12. Resistivity change rates as a function of energy for two copper crystals (orientations indicated in the insert) (Kamada *et al.*, 1964).

Unfortunately, they have not reported experiments on samples with ⟨100⟩ orientation, which—in view of its low predicted T_d—should give more directly interpretable results than the more "difficult" ⟨111⟩ direction (cf. Sec. II). The observed threshold near 20 eV was attributed by them to focuson-impurity interaction, while the subthreshold displacements of Bauer and Sosin (1964) were relegated to focuson–dislocation interaction. A true threshold in the ⟨110⟩ direction was deduced by Kamada *et al.* (1964) by extrapolating their measured data above the first bending towards zero-production rate: $T_d^{\langle 110\rangle} = 28$–30 eV. (The difficulties of such an extrapolation in the possible presence of subthreshold effects was discussed by Bauer, 1964). Kamada *et al.* did not try to interpret the differences in production rate for the two sample orientations, which is, indeed, difficult assuming such a high $T_d^{\langle 110\rangle}$. Qualitatively, they can be understood from the computer results with two close-lying low values for $T_d^{\langle 110\rangle}$ and $T_d^{\langle 100\rangle}$ and a higher $T_d^{\langle 111\rangle}$. Then the high production rates of the near-(111) sample at higher transmitted energies would be due to displacements occurring at angles θ from the incident electron direction, where the low-T_d mechanisms in the numerous easy directions ⟨100⟩ and ⟨110⟩ begin to work. (This is sometimes called the "cos² effect" because of the amount of transmitted energy, $T = T_m \cos^2\theta$.) The θ-dependence of the scattering cross section, Eq. (1.11a), also contributes to this increase in the production rate.

Sosin and Garr (1965) irradiated copper crystals in the three fundamental directions; their results are presented in Fig. 13. Because of nonuniform specimen thickness, the authors reirradiated the original samples after reduction of their thickness (curves B). They concluded from these curves that the thresholds in the ⟨110⟩ and ⟨100⟩ directions were essentially the same: $T_d^{\langle 100\rangle} \approx T_d^{\langle 110\rangle} \approx 19$ eV. The low apparent threshold in the ⟨111⟩ direction is, as in the Kamada data (1964), in fact due to displacements in the two other principal directions; the lower production rate at higher energies [curve B for the (111) sample] is a consequence of a higher $T_d^{\langle 111\rangle}$. The somewhat greater initial thickness of the (111) sample ($\sim 15\mu$ as compared to less than 10μ for the others) explains the higher production rate in the ⟨111⟩ direc-

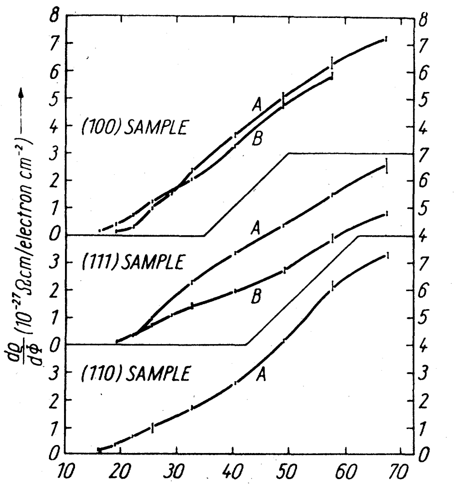

FIG. 13. Resistivity change rates as a function of energy for three orientations in copper. The A curves were the original irradiations, the B curves were obtained after a sample-thickness reduction (Sosin and Garr, 1965).

tion (curve A) as due to displacements under a big enough angle to cause ⟨110⟩ and ⟨100⟩ recoils ($\cos^2$ effect). Incidentally, the even greater thickness (35μ) of the specimens in the experiments of Kamada *et al.* (1964) is certainly one more reason for their high ⟨111⟩ production rates (cf. Fig. 12).

Gettys (1966) has tried to reproduce the near-threshold data for the (110) samples of Kamada and Sosin by applying the simple threshold energy surface defined in Sec. II, Eq. (2.6). The general energy dependence of the displacement cross section corresponds relatively well to the experimental damage rates, but the influence of the sample thickness is contrary to the observations: σ decreases with increasing thickness, while the Kamada results (1964) with 35-μ thick specimens lie in the range $T_m = 20$ to 25 eV, about twice as high as Sosin and Garr's (1965) with their 10 μ samples. Thus it appears oversimplified to construct $\sigma(\theta, \varphi)$ considering only displacements near one major axis at a time.

The most extensive work on copper has been done by Jung *et al.* (1973), who irradiated a few single-crystal foils in many crystal directions (by rotating them with respect to the incident beam) and measured the changes in residual electrical resistivity. After correction for multiple electron scattering, beam energy degradation, and the varying foil thickness, they obtained an energy-dependent damage rate as a function of lattice direction (Fig. 14). [Because of accelerator limitations, it was not possible to obtain data below 1 MeV, which is quite a bit above the copper threshold; the results of Sosin and Garr (1965) in the main crystal directions joined, however, the data of Jung *et al.* (1973) smoothly in the low-energy range.] In order to obtain from the damage rates the orientation dependence of the threshold energy $T_d(\Omega)$, they first calculated theoretical damage rates for different test functions $T_d(\Omega)$, in analogy to Eq. (3.1b), according to

$$\frac{\Delta\rho}{n}(\Omega, E) = \rho_F \int_{T(E,\,\Omega-\Omega')>T_d(\Omega')} \frac{d\sigma}{d\Omega'}(E, \Omega-\Omega')\, d\Omega' .$$

Here, the integration is done over all angles Ω' around the direction of incidence Ω, where the transmitted energy $T(E, \Omega - \Omega')$ along Ω' exceeds the threshold energy T_d in this direction. The authors divided the fundamental triangle into regions of 5×5° and established a fitting program with the resulting 39 $T_d(\Omega)$ as parameter. By variation of $T_d(\Omega)$, they attempted a fit first for the principal crystallographic directions and then for the intermediate ones, and for different electron energies. The best fit is shown in Fig. 15: we notice, as expected, the low-T_d regions around the ⟨110⟩ and the ⟨100⟩ orientations (22–23 eV and 20–22 eV, respectively) and the higher T_d around ⟨111⟩ (40–50 eV). The striking new feature, which had not been predicted by the computer simulations, is the minimum in T_d off the main axes: ~10° off ⟨110⟩ (19–21 eV), and ~25° off ⟨100⟩ (19–22 eV). This resembles somewhat the threshold energy surfaces suggested by Wollenberger and Wurm (1965) (cf. Fig. 9 and the insert of Fig. 11), though the present minima are much shallower. Another instructive view is given in Fig. 16. which represents a cut through the threshold energy surface of Fig. 15 along the border of the fundamental triangle. The broken line represents the predictions of the computer simulations and shows the remark-

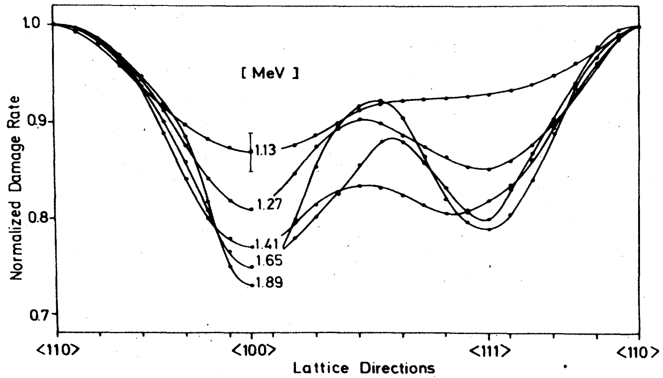

FIG. 14. Damage rates normalized to ⟨110⟩ in copper as a function of crystal orientation, for various electron energies (Jung *et al.*, 1973).

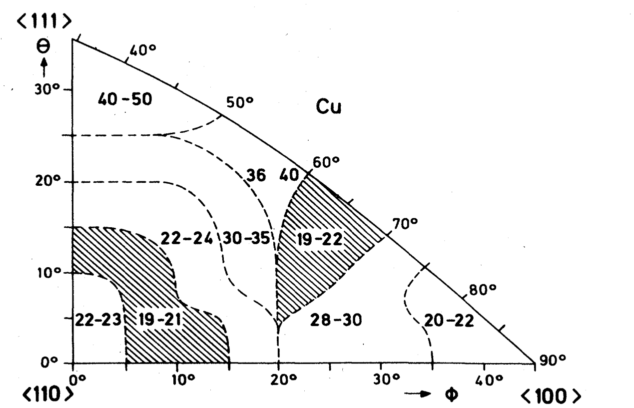

FIG. 15. Threshold energy profile in the fundamental triangle of copper, showing the T_d range in each specific region. The minimum-T_d regions are shaded (Jung *et al.*, 1973).

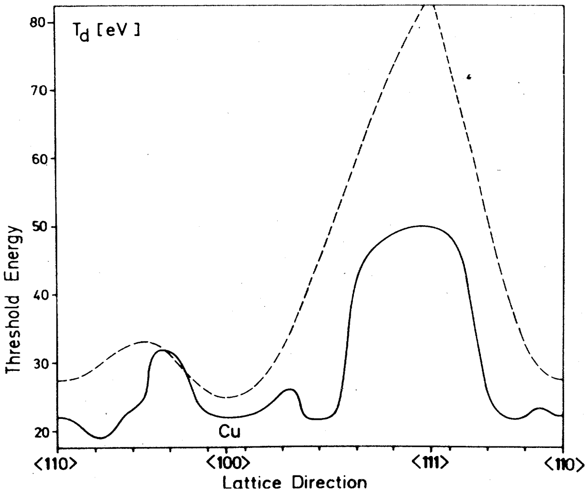

FIG. 16. Threshold energy contour in copper; the broken line corresponds to the computer calculations of Gibson *et al.* (1960) (Jung *et al.*, 1973).

ably good qualitative correspondence of the two results.

As was shown in Sec. III, an additional result of a fit of theoretical displacement cross sections to experimental resistivity change rates is the Frenkel-pair resistivity ρ_F. In the above case of copper, Jung *et al.* (1973) deduced a $\rho_F^{\mathrm{Cu}} = (1.7\pm 0.3)\ 10^{-4}\Omega$ cm per unit concentration of Frenkel pairs. This compares quite well with the value established by Ehrhart and Schlagheck (1974) from combined measurements of diffuse x-ray scattering and electrical resistivity change (cf. Sec. III.C): $\rho_F^{\mathrm{Cu}} = (2.0\pm 0.4)10^{-4}\Omega$ cm/FP.

The first threshold determinations from observation of loop formation in an electron microscope were made on copper by Makin (1970). He found rather close values for the three principal crystallographic directions: $T_d^{\langle 100\rangle} = 21.6$ eV, $T_d^{\langle 110\rangle} = 19.2$ eV, $T_d^{\langle 111\rangle} = 23.6$ eV. The two former values are in good agreement with those determined from electrical resistivity measurements, but $T_d^{\langle 111\rangle}$ is far too low. This apparent contradiction is again due to the $\cos^2$ effect. As was pointed out by Jung *et al.* (1973), a consequence of this effect is that a minimum $T_d = 19$ eV at 10° off the $\langle 110\rangle$ direction (cf. Fig. 15) would lead to effective thresholds in the main crystal directions $T_d^{\langle hkl\rangle} = 19\ \mathrm{eV}/\cos^2\Delta$, as given in Table II. It is evident that Makin's $T_d^{\langle 111\rangle} = 23.6$ eV is an *apparent* threshold only, reflecting the fact that irradiating a foil perpendicularly to the (111) plane will first produce displacements along the easy directions with $T_d \approx 19$ eV. Only the lowest measured T_d is likely to be a true threshold in a specific direction. This is a serious limitation for the interpretation of electron-microscope observations in terms of true threshold energies.

TABLE II. Comparison of the effective threshold energies along the main crystal axes derived from the T_d surface of Fig. 15 with the apparent thresholds determined by Makin (1970); Δ is the angle between $\langle hkl\rangle$ and the position of the T_d minimum (Jung *et al.*, 1973).

$\langle hkl\rangle$	Δ/deg [a]	$T_d^{\mathrm{eff}} = \dfrac{19\ \mathrm{eV}}{\cos^2\Delta}$	T_d^{app}/eV [b]
$\langle 110\rangle$	5–10	19.1–19.6	19.2
$\langle 100\rangle$	20–25	21.5–23.1	21.6
$\langle 111\rangle$	20–25	21.5–23.1	23.6

[a] Jung *et al.*, 1973.
[b] Makin, 1970.

The same remark has to be made with respect to the results presented by Mitchell *et al.* (1975) on electron-microscope irradiations of a series of metals including copper. They found a minimum T_d in the $\langle 110\rangle$ direction: $T_d^{\langle 110\rangle} = 18$ eV, in good agreement with previous measurements. The other thresholds $T_d^{\langle 100\rangle} = 27$ eV, and $T_d^{\langle 111\rangle} = 29$ eV, are probably, again, only apparent thresholds. A further complicating factor in both this and Makin's experiment (1970) is the high irradiation temperature (300 K). It is possible that the creation of some Frenkel pairs is more favorable than that of others due to differing degrees of virtual stability during irradiation. Thus a $\langle 110\rangle$ long-range collision is more likely to yield a free interstitial ending up in an observable loop than a $\langle 100\rangle$ displacement with the same low-temperature threshold; in order to attain the same stability, a $\langle 100\rangle$ knock-on would have to go farther away and, therefore, require a higher transmitted energy.

Finally, qualitative information on the anisotropy of the defect production rate in copper has been provided by Akita and Fiore (1973), who have measured the ultrasonic attenuation due to dislocation damping in (100) and (110) crystals irradiated with Co-60 gamma rays. Their results are shown in Fig. 17: the decrease in damping due to the introduction of point defects is strongest for the (110) sample, implying a larger damage rate in this direction. An analysis (cf. Sec. III.D) of the data yields a dislocation length ratio of annealed to irradiated specimens

$$L_{\mathrm{ann}} : L_{\langle 100\rangle} : L_{\langle 110\rangle} \approx 1.0 : 0.66 : 0.52\,,$$

which gave a ratio of the defect densities N (proportional to L^{-1})

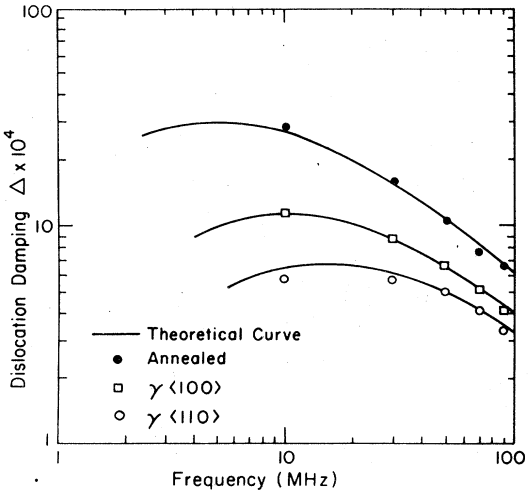

FIG. 17. Dislocation damping as a function of frequency for annealed and irradiated copper crystals (Akita and Fiore, 1973).

$$N_{\rm ann} : N_{\langle 100\rangle} : N_{\langle 110\rangle} \approx 1.0 : 1.52 : 1.92\,.$$

Thus roughly 25% more defects were created by ~1 MeV gammas in the ⟨110⟩ direction, consistent with a minimum replacement energy in this direction.

b. Silver

There are practically no data on defect studies with electrons in monocrystalline silver. Preliminary results have been reported by Mitchell *et al.* (1975), who bombarded (110) specimens in an electron microscope. Black-spot damage was observed at 700 kV, but not at 650 kV; the authors propose a ⟨110⟩ threshold of $E_d^{\langle 110\rangle} = 675$ keV corresponding to a $T_d^{\langle 110\rangle} = 23$ eV.

c. Gold

A detailed investigation of the atomic displacement process in single crystals of gold was undertaken by Bauer, Anderman, and Sosin (1969). They irradiated 5–13-μ thick foils of the orientations ⟨110⟩, ⟨100⟩, and ⟨111⟩ by electrons in the range 1.4 to 2.2 MeV. The striking feature of this experiment was that the damage rates were practically the same for all crystallographic orientations in the whole investigated energy range (Fig. 18). This is, indeed, somewhat unexpected since it could imply an essentially isotropic threshold energy surface, in contradiction with both the model calculations and the experimental results for copper (see previous section). Thus the authors deduced from Fig. 18: $T_d^{\langle 100\rangle} \sim T_d^{\langle 110\rangle} \sim T_d^{\langle 111\rangle} \approx 36$ eV. This is, however, only valid under the assumption of local minima in these directions. From the computer model for copper it followed that such minima were present in the ⟨110⟩ and the ⟨100⟩ directions, but that ⟨111⟩ was a local maximum. Thus $T_d^{\langle 111\rangle} \sim 36$ eV could be due to the manifestation of the $\cos^2$ effect caused by glancing collisions into the easy directions. On the other hand, one notices near the threshold of 1.4 MeV a bending in the ⟨110⟩ damage rate. This phenomenon was attributed by the authors to subthreshold collisions, which would be predominant in the case of the ⟨110⟩ direction, suggesting a defocusing mechanism at impurities. Such a bending phenomenon could, however, also be explained by a lower threshold energy for displacement in the ⟨110⟩ direction, so that one observes near 1.4 MeV the onset of another displacement mechanism with a higher threshold, this time with $T_d \sim 36$ eV. To decide on this question one would have to irradiate at even lower energies, in order to pursue the bending towards a possible lower threshold or to a plateau. The latter would indicate a real subthreshold mechanism. Moreover, it is essential to calculate the displacement cross sections for *all* angles and to fit the experimental data assuming a model T_d surface, as was done by Maury *et al.* (1973b) for several hcp metals. This would give information on the size of the extrema in this surface and, in particular, yield an absolute value for $T_d^{\langle 111\rangle}$.

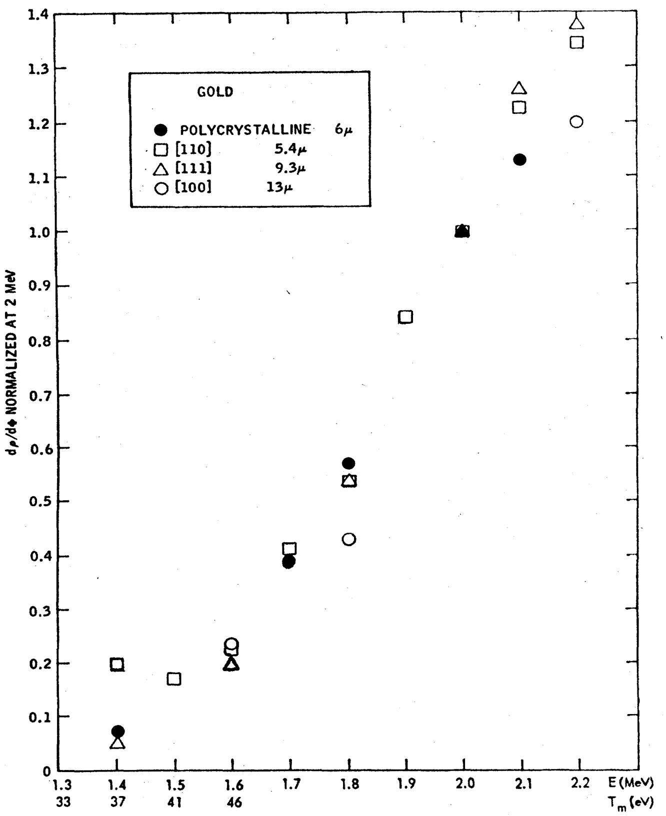

FIG. 18. At 2 MeV normalized resistivity change rates for gold crystals as a function of energy (Bauer *et al.*, 1969).

Recently, Hancock and Lomer (1974) have repeated this experiment with 10–20-μ thick gold foils of the orientations ⟨100⟩ and ⟨110⟩. Again, no significant anisotropy in the defect production rate was noticed,

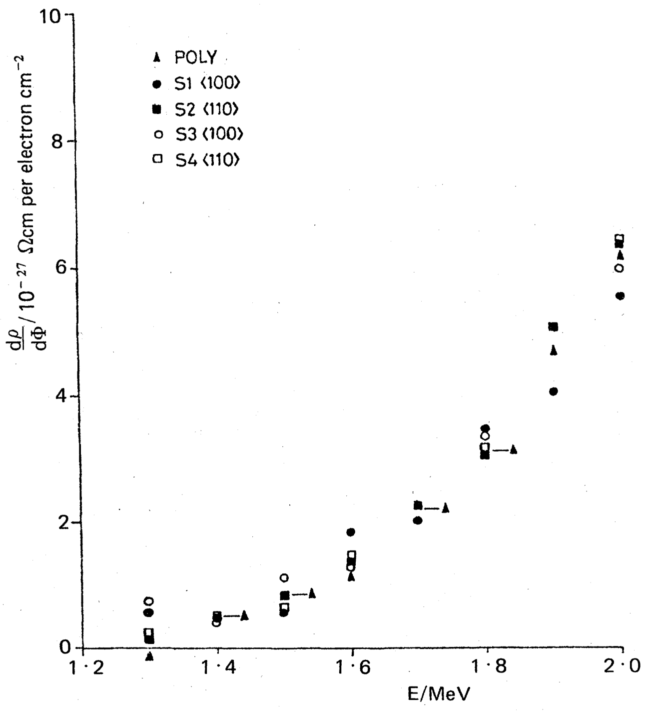

FIG. 19. Absolute resistivity change rates of mono- and polycrystalline gold as a function of energy (Hancock and Lomer, 1974).

and a simultaneously irradiated polycrystal gave the same results (Fig. 19). The authors concluded to an essentially isotropic displacement energy equal to $T_d = 40 \pm 2$ eV. Subthreshold events seem also to play a role, but this time it is the (100) specimen which exhibits bending near the threshold. A step function analysis of the data gave a Frenkel-pair resistivity of $\rho_F^{\mathrm{Au}} \sim 1.2 \times 10^{-4}\Omega$ cm/FP. This value is rather low when compared to other metals, but can be understood considering the anomalous annealing behavior of gold where the recovery seems to begin even below 2 K (Gwozdz, 1973): thus one measures only a part of the originally produced damage and ρ_F corresponds to the remaining percentage. On the other hand, a recent determination of the interstitial concentration in electron-irradiated gold at 5 K by diffuse x-ray scattering (Ehrhart and Segura, 1975), together with the measurement of the induced resistivity change, gave a $\rho_F^{\mathrm{Au}} = (3.2 \pm 0.3) \times 10^{-4}\Omega$ cm/FP.

d. Beta-cobalt

Hexagonal close-packed (α-cobalt) and face-centered cubic (β-cobalt) grains do often coexist in polycrystalline cobalt foils. This fact was made use of by Howe (1970), who irradiated both cobalt phases in an electron microscope. I report in this section the results on fcc β cobalt. Varying the incident beam energy at room temperature, Howe observed a threshold for loop formation in the $\langle 110 \rangle$ and the $\langle 100 \rangle$ direction, from which he deduced a $T_d^{\langle 110 \rangle} = 23 \pm 0.5$ eV and $T_d^{\langle 100 \rangle} = 30 \pm 1$ eV. No other data on β cobalt are available, but comparison with copper indicates that the former value might well be a local minimum in the threshold energy surface. As to the value for $T_d^{\langle 100 \rangle}$, it seems too high for another local minimum. Anticipating the discussion of hcp α cobalt in Sec. IV.A.3., it should be mentioned here that the threshold in the closest-packed direction $\langle 11\bar{2}0 \rangle$, 23 eV, and the one in the assisted focusing direction $\langle 10\bar{1}0 \rangle$, 30 eV, are quite in analogy with the roughly corresponding fcc directions $\langle 110 \rangle$ and $\langle 100 \rangle$. Definite conclusions, however, are only to be drawn after a complete angular integration of the displacement cross section.

e. Nickel

For nickel, there exists a thorough electron-microscopic study of damage production in (100), (110), and (111) crystals. Bourret (1971) has investigated the energy dependence of the loop formation in these crystals and obtained apparent thresholds: $T_d^{\langle 110 \rangle} = 23 \pm 2$ eV, $T_d^{\langle 100 \rangle} = 31 \pm 1.5$ eV, $T_d^{\langle 111 \rangle} = 28 \pm 1.5$ eV. Unlike other investigators, (Makin 1970, Mitchell *et al.* 1973, Howe 1970) he did not identify these thresholds with the true T_d's but attempted a computer analysis of the data by calculating the displacement cross section with an appropriate threshold energy surface. For the latter he used Jan and Seeger's (1963) T_d surface [cf. Eq. (2.4)]. The best fit to experiment was obtained with the parameters $T_{110} = 21 \pm 1$ eV, $T_{100} = 38 \pm 3$ eV, and $T_{111} > 60$ eV, these values being the true threshold energies in the respective directions (but keeping in mind the reservations concerning Jan and Seeger's T_d surface made in Sec. II.B). Figure 20 shows the experimental points together with the matching cross sections.

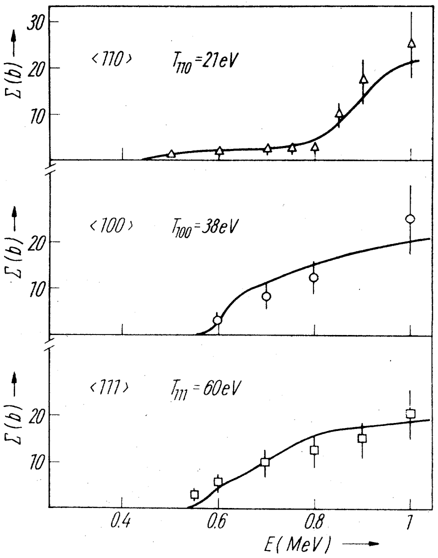

FIG. 20. Comparison between calculated cross sections using the T_d surface of Jan and Seeger (1963) and experiment for various nickel crystals (Bourret, 1971).

The fit is satisfactory, although one must bear in mind that the threshold for producing free interstitials (as they are observed in an electron microscope) is not necessarily the same as the threshold for producing stable Frenkel pairs (as in resistivity measurements). Considering all this, it is quite comforting that the easiest displacement direction is once more $\langle 110 \rangle$ and that $T_d^{\langle 111 \rangle}$ seems to be a local maximum.

f. Platinum

At the same time as they investigated copper, Jung *et al.* (1973) made a study of the threshold energy surface of platinum. The measured orientation dependence of the resistivity change rate is shown in Fig. 21. A computer analysis of these data, in which a variable T_d

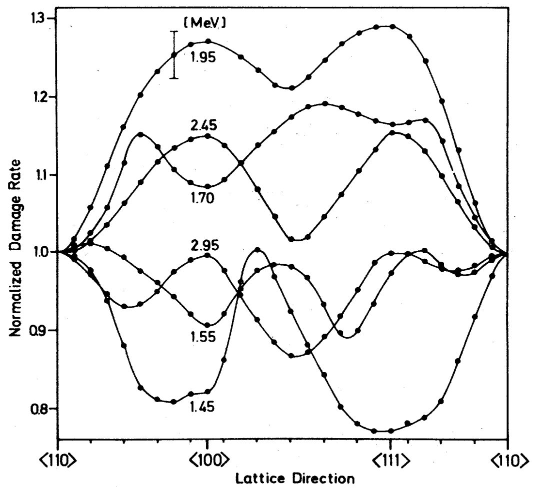

FIG. 21. Damage rates normalized to $\langle 110 \rangle$ in platinum as a function of crystal orientation, for various electron energies (Jung *et al.*, 1973).

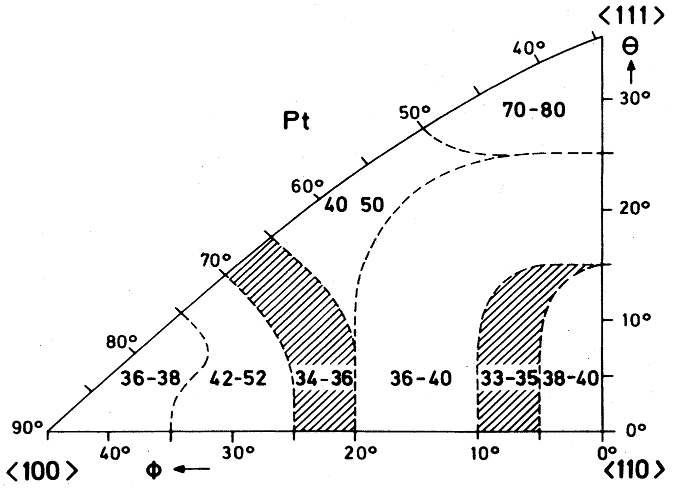

FIG. 22. Threshold energy profile in the fundamental triangle of platinum, showing the T_d range in each particular region; the minimum-T_d regions are shaded (Jung *et al.*, 1973).

surface was used to calculate the displacement cross sections in each direction (cf. Sec. IV.A.1.*a*), gave the best fit with the parameters indicated in Fig. 22. As in the case of copper, we note the ring shaped region with a minimum $T_d = 34$–36 eV 20°–25° off the ⟨100⟩ direction ($T_d^{\langle 100\rangle} = 36$–$38$ eV), and another one with a $T_d = 33$–35 eV ~ 10° off the ⟨110⟩ direction ($T_d^{\langle 110\rangle} = 38$–$40$ eV). A cut along the border of the fundamental triangle of Fig. 22 is presented in Fig. 23. Comparison with the computer data on copper (broken line) confirms the closely-lying low T_d values in the ⟨110⟩ and ⟨100⟩ directions as well as the maximum at ⟨111⟩; the results of the computer model exhibit, however, much less structure, in particular lacking the minimum T_d belts around ⟨110⟩ and ⟨100⟩.

As in the case of copper, the authors were able to deduce from their analysis a Frenkel-pair resistivity for platinum: $\rho_F^{\mathrm{Pt}} = (9.5 \pm 0.5) \times 10^{-4} \Omega$ cm/FP.

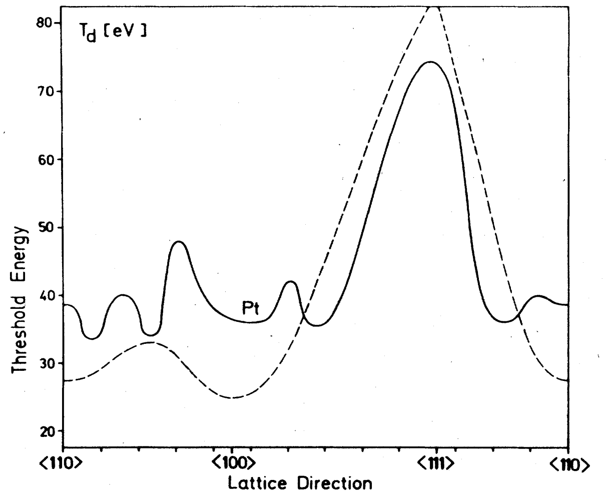

FIG. 23. Threshold energy contour in platinum; the broken line corresponds to the computer results on copper from Gibson *et al.* (1960) (Jung *et al.*, 1973).

g. Aluminum

No damage rate studies have been undertaken up to now in aluminum crystals, partly because of the experimental difficulties connected with the low mass and, hence, low threshold displacement energy in Al. One way to avoid the inherent multiple scattering problem would be to do electron-microscope investigations, which use foils of (for this effect) negligible thickness.

The only useful data in this context stem again from a combination of diffuse x-ray scattering and lattice parameter measurements on electron-irradiated Al crystals (Ehrhart and Schilling, 1973), in which the absolute concentration of the created defects was determined as a side result. By a simultaneous measurement of the increase in residual electrical resistivity, the authors were able to determine the Frenkel-pair resistivity for aluminum: $\rho_F^{\mathrm{Al}} = (3.9 \pm 0.6) \times 10^{-4} \Omega$cm/FP.

2. Body-centered cubic lattice

a. Vanadium

Only raw data have been reported concerning the threshold determinations in vanadium crystals. Kenik and Mitchell (1975) irradiated (100), (110), and (111) specimens in an electron microscope and observed the onset of black spot formation at $E_d^{\langle 100\rangle} = 475$ keV, $E_d^{\langle 110\rangle} = 575$ keV, and $E_d^{\langle 111\rangle} = 525$ keV, corresponding to the apparent thresholds $T_d^{\langle 100\rangle} = 30$ eV, $T_d^{\langle 110\rangle} = 39$ eV, and $T_d^{\langle 111\rangle} = 35$ eV. Here $T_d^{\langle 100\rangle} = 30$ eV could be a local minimum, although it is somewhat higher than the T_d determined for polycrystalline vanadium (Miller and Chaplin, 1974), ~ 26 eV. The latter discrepancy could be due to the higher temperature (300 K) of the electron microscope experiment, as there would be a higher transmitted energy required to create the “free” interstitial observed later in the black spots (cf. also the discussion on copper in Sec. IV.A.1.*a*).

b. Chromium

In a study analogous to that of vanadium, Mitchell *et al.* (1975) determined the apparent thresholds for the three principal orientations in chromium: $T_d^{\langle 100\rangle} = 21$ eV, $T_d^{\langle 110\rangle} = 34$ eV, $T_d^{\langle 111\rangle} = 24$ eV. Comparison with polycrystal data (Biget, Vajda, 1975) shows that $T_d^{\min} = 21$ eV is lower than $T_d^{\mathrm{poly}} = 28 \pm 1$ eV. On the other hand, recently obtained data on Cr single crystals (Biget *et al.*, 1977b) indicate that $T_d^{\min} = 28$ eV. Furthermore, it is most probably $T_d^{\min} = T_d^{\langle 100\rangle}$.

c. Alpha-iron

A direct consequence of the computer experiments by Erginsoy *et al.* (1964) on bcc α-iron was the investigation of the directional dependence of defect production in iron crystals by Lomer and Pepper (1967). The authors used (100) and (111) specimens and measured the increase of their residual resistivity after electron bombardment in the energy range 0.3 to 2.0 MeV. Because of uncertainties in the determination of the geometrical form factor of the samples, they only compared the shape of the obtained production curves; this

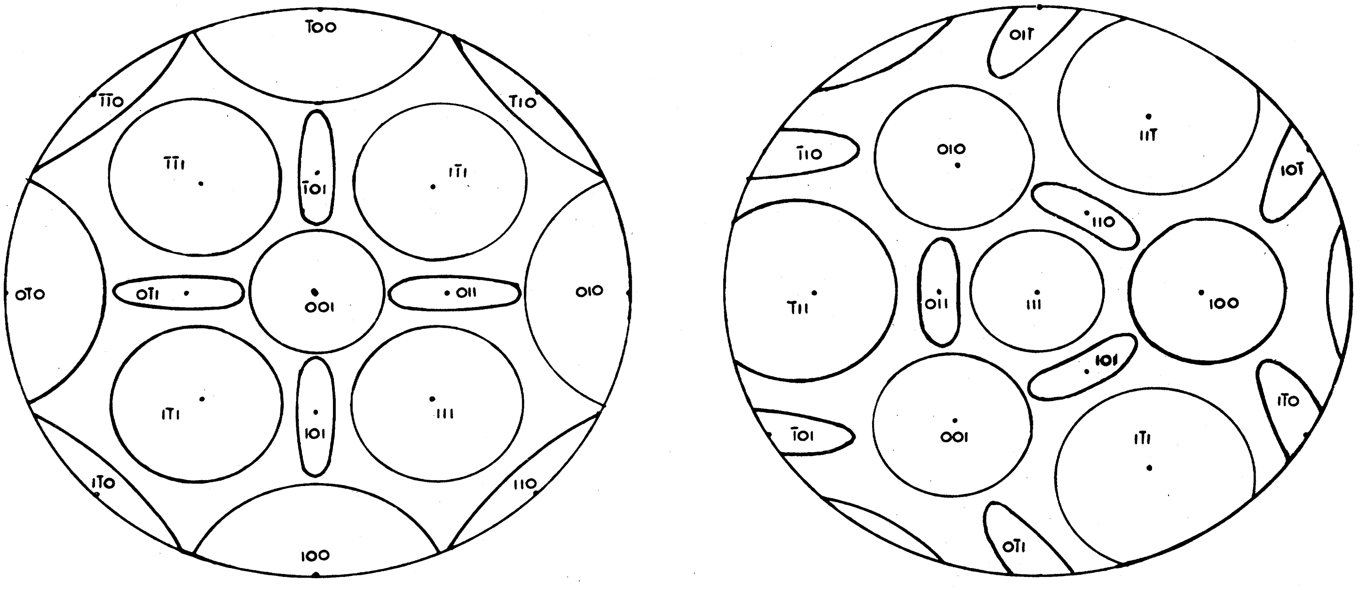

(a) (b)

FIG. 24. Stereographic projection of the displacement energy surface in α-iron; (a) view along ⟨100⟩, (b) along ⟨111⟩ (Lomer and Pepper, 1967).

removed the possibility of relating the absolute values of the resistivity change rates to theoretical cross sections and of calculating the Frenkel-pair resistivity ρ_F. It enabled them, nevertheless, to determine a threshold energy surface using the geometrical model for displacements in a bcc lattice shown on stereograms in Fig. 24; the model is a result of an adaptation of the computer findings (cf. Fig. 6). The cross sections computed with this surface, using as parameters the $T_d^{\langle hkl \rangle}$ in the three principal directions, gave a best fit to the experimental energy dependence with $T_d^{\langle 100\rangle}=20$ eV, $T_d^{\langle 110\rangle}=T_d^{\langle 111\rangle}=30$ eV; the normalized results are displayed in Fig. 25. This is in good qualitative agreement with the averaged values of the computer predictions—$T_d^{\langle 100\rangle}=17$ eV, $T_d^{\langle 110\rangle}=35$ eV, $T_d^{\langle 111\rangle}=38$ eV—in that $T_d^{\langle 100\rangle}$ is a local minimum and $T_d^{\langle 110\rangle}\approx T_d^{\langle 111\rangle}$; the relative depth of the ⟨100⟩ minimum is, however, larger in the computer model. An interesting feature of this experiment, which is reproduced in the calculated cross sections, is the hump at low energies in the case of the ⟨100⟩ irradiation. This is readily understood when we consider the T_d surface of Fig. 24 with a T_d minimum in the ⟨100⟩ direction. Immediately above threshold the production rate will increase with energy as long as the knock-on energy contour lies within the central (100) displacement region of Fig. 24(a). A further increase of transmitted energy will lead into regions with higher displacement threshold, outside the (001)-circle. Thus the displacements being still limited to the easy (100) region, the actual number of knock-on atoms will decrease due to the T^{-2} dependence of the cross section [cf. Eq. (1.11b)].

Since it was desirable to obtain absolute production rates and also to determine experimental ⟨110⟩ production curves for comparison, Maury *et al.* (1976) undertook an electron irradiation of iron crystals of the three principal orientations. The measured resistivity change rates in the energy range 0.35–1.7 MeV are exhibited in

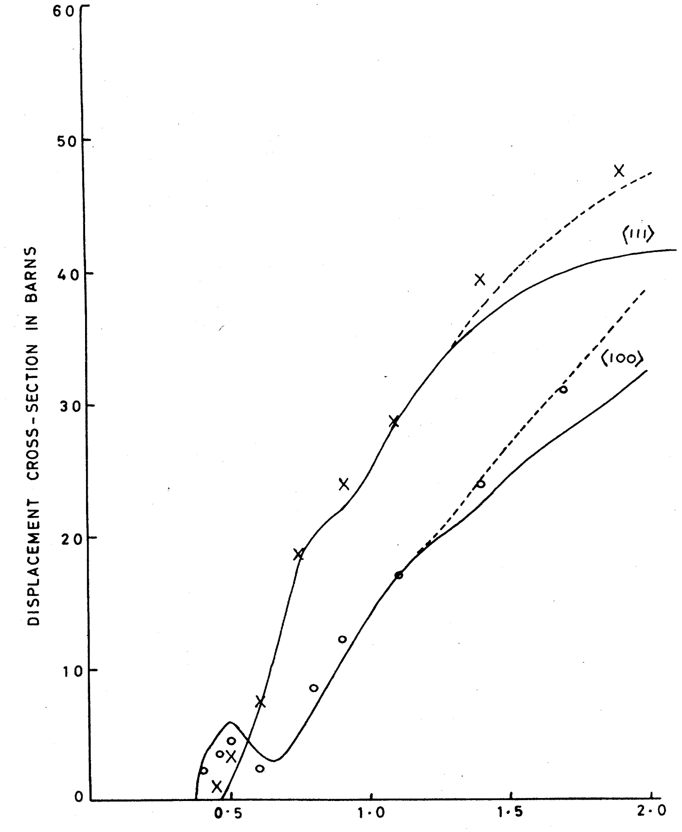

FIG. 25. Theoretical displacement cross sections calculated with the T_d surface of Fig. 24 using $T_d^{\langle 100\rangle}=20$ eV, $T_d^{\langle 110\rangle}=T_d^{\langle 111\rangle}=30$ eV; the dotted lines are the estimated corrections due to multiple displacements. The experimental points have been normalized to the cross sections at 1.1 MeV (Lomer and Pepper, 1967).

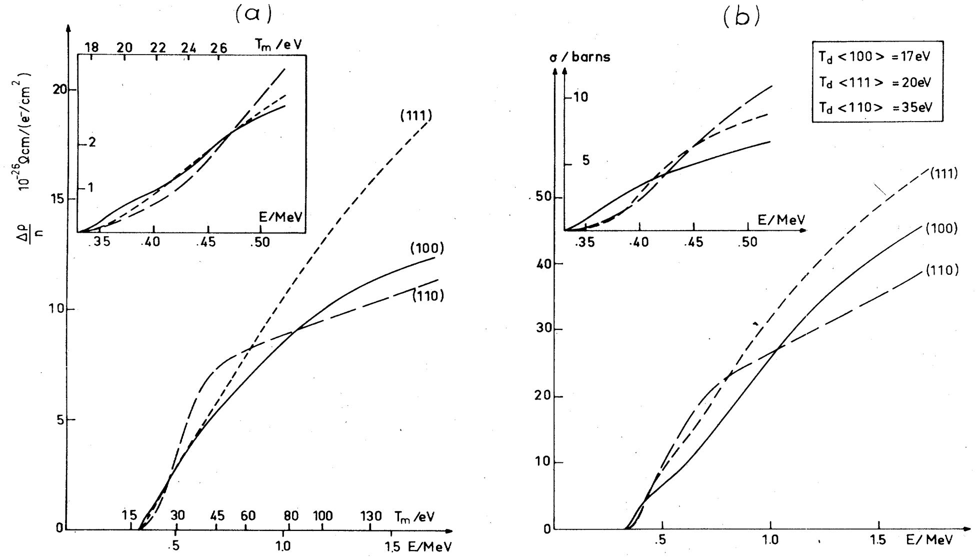

FIG. 26. Resistivity change rates (a) and displacement cross sections (b) in iron, obtained with the best-fit set of T_d's indicated in the insert (Maury *et al.*, 1976).

Fig. 26(a): one notes that the (100) specimen possesses the minimum E_d. In order to understand the energy dependence of defect production for the various crystals, a computer model was employed which uses a potential-lens image of the bcc cell and is described in more detail in the following section on molybdenum. The theoretical displacement cross sections derived in this way were matched to the experimental curves of Fig. 26(a) using the threshold energies in the principal directions as parameters. Fig. 26(b) represents the best fit obtained with the following thresholds: $T_d^{\langle 100\rangle} = (17 \pm 1)$ eV, $T_d^{\langle 111\rangle} = (20 \pm 1.5)$ eV, and $T_d^{\langle 110\rangle} = (30-35)$ eV. This is in good agreement with the preceding work on α-iron for the minimum displacement threshold in the ⟨100⟩ direction and, in particular, its absolute value. The threshold in the ⟨111⟩ direction is, however, lower than predicted and also lower than $T_d^{\langle 110\rangle}$, a result which is, on the other hand, in excellent agreement with the following observations on molybdenum. This latter fact and the good fit to the experimental data [Figs. 26(a) and (b)] lend support to an easier displacement mechanism in the ⟨111⟩ direction. The hump observed by Lomer and Pepper (1967) is also there, but in a strongly attenuated form, probably because of a greater crystal thickness.

An important additional result followed from the comparison between Figs. 26(a) and (b), the Frenkel-pair resistivity $\rho_F^{\mathrm{Fe}} = (30 \pm 5)\times 10^{-4}\Omega$cm/FP.

d. Molybdenum

Molybdenum has been investigated quite extensively by the Orsay group. Biget *et al.* (1974) measured the resistivity change rates in single crystals of the orientations ⟨100⟩, ⟨110⟩, ⟨111⟩, and ⟨112⟩ in the energy range 0.8–1.7 MeV and found the lowest displacement energy threshold in the ⟨100⟩ direction: $T_d^{\langle 100\rangle} = 36 \pm 1$ eV (Fig. 27). A computer analysis of the data was undertaken (Maury *et al.*, 1975) using a threshold energy surface modeled according to geometrical considerations, similar to that of α-iron (cf. Fig. 24). In fact, a knocked-on atom in a bcc lattice "sees" a situation represented schematically in Fig. 28. The shaded "lenses" denote the potential barriers formed by nearest-neighbor atoms in the principal crystal directions, which favor an assisted focusing mechanism. In the ⟨111⟩ direction, there exists pure Silsbee focusing, which is assisted by the two triangular lenses L_3. The shapes and sizes of the various lenses being calculated in a straightforward way one can proceed with the integration of the displacement cross section σ [Eq. (1.9)], using $T_d^{\langle hkl\rangle}$ as a parameter. For simplicity, L_1 and L_3 are treated as circular potential wells with diameters of 44° and 52°, respectively, while the L_2 are elongated, with a width of 10° and a length of 40°. (Several other T_d surfaces were tried, varying the relative size of the lenses, but with less success.) The

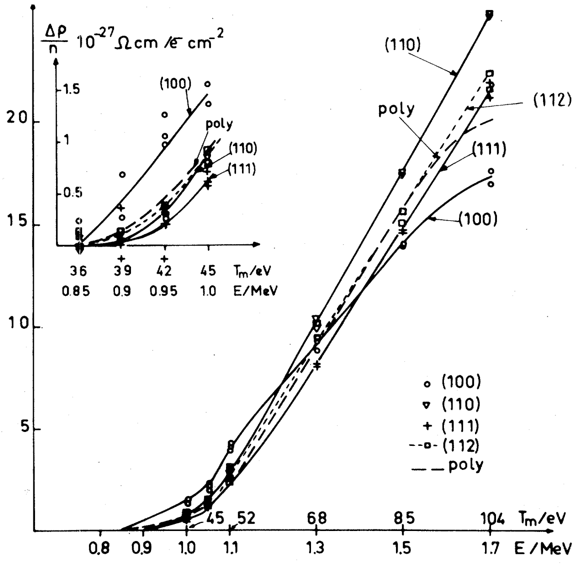

FIG. 27. Resistivity change rates of molybdenum in various crystallographic directions as a function of energy (Maury *et al.*, 1975).

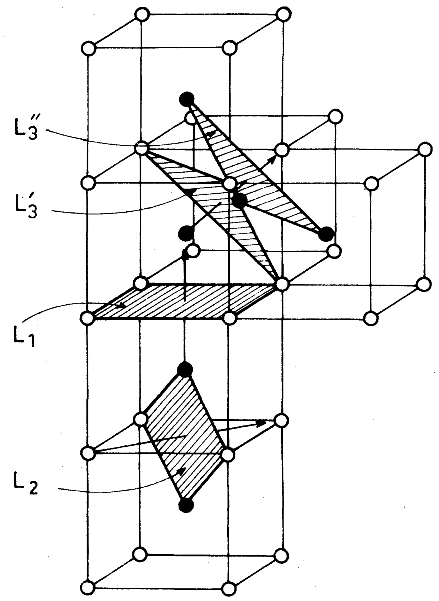

FIG. 28. Schematic representation of the displacements in the three principal directions of a bcc lattice. By L_1, L_2, L_3 are designated the "lenses" formed by the nearest-neighbor atoms in the ⟨100⟩, ⟨110⟩, and ⟨111⟩ direction. The full circles indicate the center-of-cube atoms (Maury *et al.*, 1975).

best fit to the experimental data of Fig. 26 was obtained with the following set of T_d's: $T_d^{\langle 100\rangle} = (35^{+1}_{-2})$ eV, $T_d^{\langle 111\rangle} = (45 \pm 3)$ eV, $T_d^{\langle 110\rangle} > 2T_d^{\langle 100\rangle}$. The cross sections calculated with such a T_d surface are shown in Fig. 29. In view of the certainly oversimplified picture for the threshold energy surface, the qualitative agreement is rather encouraging.

It is interesting to compare these results with existing data on polycrystalline molybdenum (Rizk *et al.*, 1973). There, a fit of a cross section to the experimental data was possible using a two-step displacement probability function with steps at (33 to 35) eV and (42 to 43) eV. An immediate correspondence is apparent: the first step is clearly related to the ⟨100⟩ displacements, the second is attributable to ⟨111⟩ collisions.

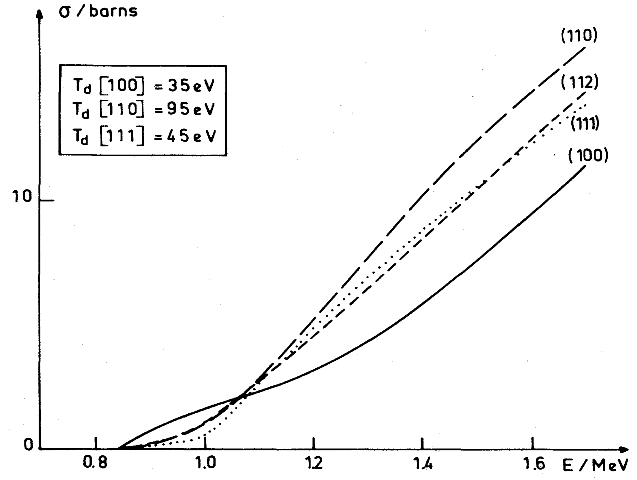

FIG. 29. Displacement cross sections for molybdenum calculated with the best-fit set of T_d's indicated in the insert, to match the data of Fig. 27 (Maury *et al.*, 1975).

A juxtaposition of the data of Figs. 27 and 29 results in an absolute value for the Frenkel-pair resistivity of molybdenum: $\rho_F^{\mathrm{Mo}} = (13 \pm 2) \times 10^{-4} \Omega\mathrm{cm/FP}$, which compares favorably with the one deduced from diffuse x-ray scattering experiments (Ehrhart, 1975): $(15 \pm 3) \times 10^{-4} \times \Omega\mathrm{cm/FP}$.

e. Tantalum

In a study similar to that of copper and platinum (Jung *et al.*, 1973) Jung and Schilling (1972) have investigated the threshold energy surface of tantalum. By rotating (110) specimens with respect to the incident electron beam, they obtained damage-rate curves such as those in Fig. 30; the electron energy was varied between 1.0 and 3.2 MeV. The energy dependence of crystals irradiated along the three principal axes is shown in Fig. 31. Theoretical displacement cross sections were calculated with various trial T_d surfaces and a good fit was obtained with the one depicted in Fig. 32. When comparing this surface with the one derived by Erginsoy *et al.* (1964) from the computer model of α-iron (Fig. 6), one notes their similarity with respect to 1) the local minima for the ⟨110⟩ and ⟨100⟩ orientations, and 2) the ring shaped minimum ~15° off the ⟨111⟩ direction. A closer look, however, shows major qualitative differences: the appearance of a deep minimum 10°–15° off ⟨100⟩ and, in particular, the fact that the lowest T_d is not in the ⟨100⟩ direction (as was the case for iron). The minimum T_d (~32 eV) was actually found in the ring region around ⟨111⟩, as can be seen in a T_d contour along the boundary of the fundamental triangle in Fig. 33. This is rather unexpected, since it had not been predicted by the computer findings. Jung and Schilling argue that the computer model might have led

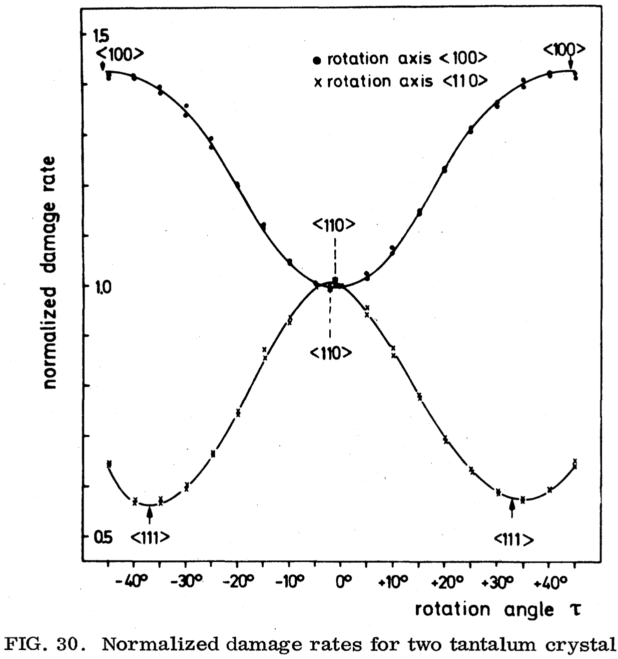

FIG. 30. Normalized damage rates for two tantalum crystals with different rotation axes (Jung and Schilling, 1972).

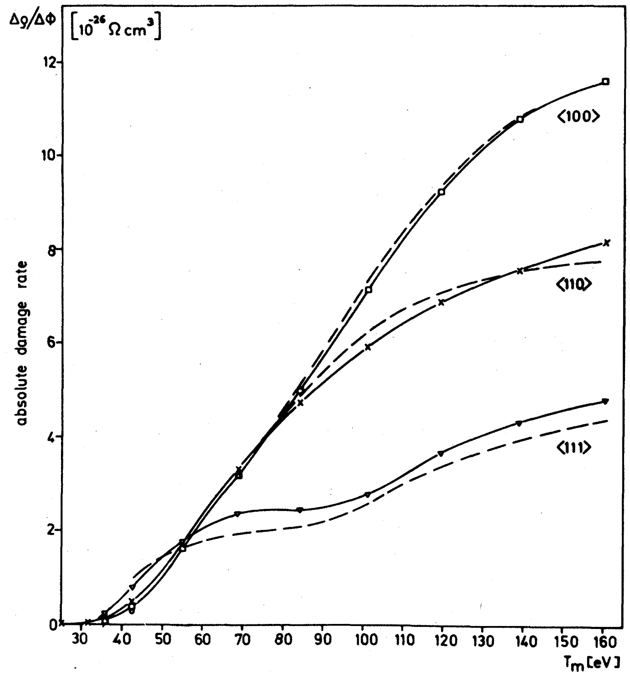

FIG. 31. Resistivity change rates in tantalum crystals bombarded along the main crystal directions; the dashed lines correspond to a multiple-scattering correction (Jung and Schilling, 1972).

to a different result when using another potential and that, in fact, it is not unreasonable to have the easiest displacements somewhere near the close-packed ⟨111⟩ row, since stable Frenkel pairs should be most easily created in replacement collisions. On the other hand, the independent experimental results on α-iron and on molybdenum confirm the computer predictions in that $T_d^{\min} = T_d^{\langle 100\rangle}$. The latter can be understood by the shape and size of the potential barrier in the ⟨100⟩ direction represented by the lens L_1 in Fig. 28. The Frenkel-pair resistivity determined as an additional result of this work is given by the authors as $\rho_F^{\mathrm{Ta}} = (17 \pm 3) \times 10^{-4} \Omega\mathrm{cm}/\mathrm{FP}$.

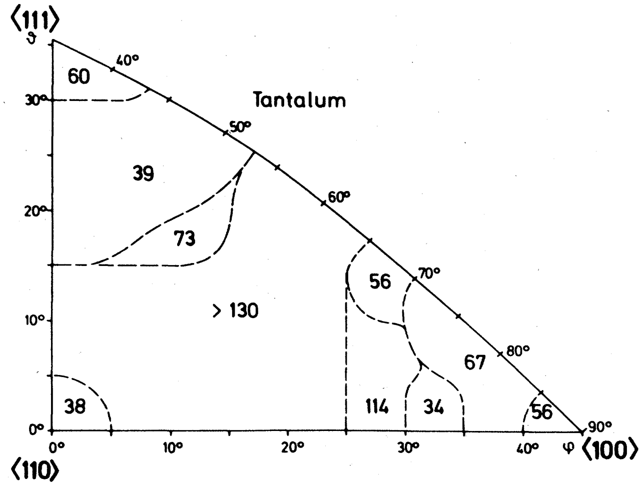

FIG. 32. Threshold energy profile of tantalum; the numbers indicate the T_d values in each particular region (Jung and Schilling, 1972).

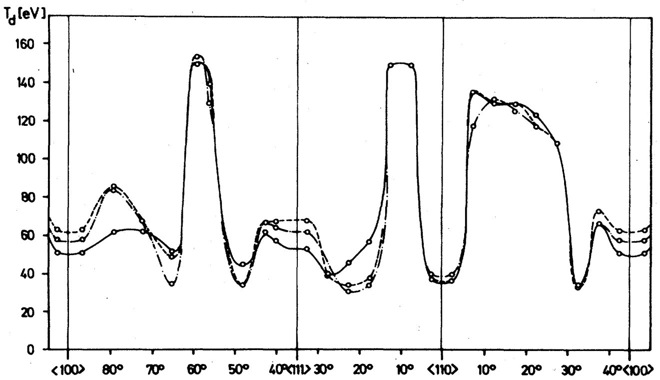

FIG. 33. Threshold energy contour along the borders of the fundamental triangle in tantalum; the curves pertain to three different fits (Jung and Schilling, 1972).

New experimental data very recently obtained at Orsay on the defect production in Ta crystals irradiated along the ⟨100⟩, ⟨110⟩, ⟨111⟩, and ⟨112⟩ directions seem to disprove the Jung-Schilling results. In fact, the authors find (Biget *et al.*, 1977a) $T_d^{\min} = T_d^{\langle 100\rangle}$, in perfect agreement with iron and molybdenum. The numerical analysis of the results gave $T_d^{\langle 100\rangle} = 33 \pm 1$ eV and $T_d^{\langle 111\rangle} \geq 55$ eV. The form of the defect production curve of the (100) crystal necessitated the assumption of a second threshold in the ⟨100⟩ direction, $T_d'^{\langle 100\rangle} = 38$ eV. The fit to the experiment was best when only a part of the ⟨100⟩ defects was created with a threshold of 33 eV, the displacement probability reaching a value of one only at 38 eV. This finds a satisfactory explanation when supposing a different stability of the resulting interstitial according to its configuration {e.g. [110] or [011]} as has been demonstrated on molybdenum, cf. the discussion in Sec. IV.B.2.*b*. Thus, in order to form an interstitial in a less stable configuration, a knock-on atom would have to travel farther than in the case where it would end up in a more stable configuration, implying a higher threshold for the former case and a lower one for the latter. As to the discrepancy with the Jung-Schilling data, it seems that it is due to a possible misorientation of their crystals as can be deduced from the presented Laue patterns [Fig. 18b/c in Jung, 1971].

The Frenkel-pair resistivity determined in the Orsay experiment $\rho_F^{\mathrm{Ta}} = (16 \pm 3) \times 10^{-4} \Omega\mathrm{cm}/\mathrm{FP}$, compares well with that of Jung and Schilling, which is not surprising since it is representative for the *total* defect concentration (i.e., produced in an angle of 4π) which is conserved with permuted crystals.

3. Hexagonal close-packed lattice

No computer simulations have been available up to now for the displacement processes in an hcp lattice. Because the symmetry properties of hcp lattices are different from the two cubic lattices discussed in the preceding sections, it is of particular interest to analyze the results for the three hcp metals cobalt, zinc, and cadmium. An additional interest stems from the fact that cobalt possesses a practically ideal c/a ratio, while for zinc and for cadmium it is much bigger, thus introducing a new parameter into the structure characterization.

a. Alpha-cobalt

The first hcp crystal to be investigated with respect to damage anisotropy was α-cobalt. Two simultaneous studies were performed: one by high-voltage electron microscopy, the other by electrical resistivity measurements.

As already mentioned in Sec. IV. A. 1. *d.*, Howe (1970) had irradiated both fcc and hcp cobalt grains in an electron microscope. He found the following threshold energies for observable damage in the hcp phase: $T_d^{\langle 11\bar{2}0\rangle} = (23 \pm 0.5)$ eV, $T_d^{\langle 10\bar{1}0\rangle} = (30 \pm 1)$ eV, and $T_d^{\langle 0001\rangle} = (33 \pm 1)$ eV. This compared in an interesting way with the thresholds in the fcc β phase, where $T_d^{\langle 110\rangle} = (23 \pm 0.5)$ eV and $T_d^{\langle 100\rangle} = (30 \pm 1)$ eV. Since both the $\langle 11\bar{2}0\rangle$ direction in the hcp lattice and the $\langle 110\rangle$ direction in the fcc lattice are the closest packed and, therefore, probably among the easiest orientations for displacement of an atom, it seems reasonable to suppose the existence of a local minimum there. To appreciate the other thresholds one has to go to a more extended analysis as has been done by the Orsay group (Maury *et al.*, 1970, 1973a).

Bombarding 20-μ thick foils perpendicular to the planes (0001), $(10\bar{1}0)$, $(11\bar{2}0)$, $(30\bar{3}4)$, and $(30\bar{3}8)$, Maury *et al.* (1973a) found minimum defect production rates in the whole investigated electron-energy range of 0.45–1.7 MeV for the $(11\bar{2}0)$ crystal, while they found that (0001) specimens always exhibited maximum damage rates (Fig. 34). The apparent thresholds for the investigated orientations were all situated in the interval 450 to 500 keV, $E_d^{\min}$ being in the $\langle 0001\rangle$ direction, and $E_d^{\max}$ in the $\langle 11\bar{2}0\rangle$ direction; the other apparent thresholds were intermediate. These experimental results have been analyzed in a "geometrical" model where possible propulsion mechanisms of a knocked-on atom in an hcp crystal were proposed (Maury *et al.*, 1973b). Figure 35 represents half the unit cell of an hcp crystal, specifying the principal directions which the central atom of the basal plane will take after being given sufficient knock-on energy. (Several of the orientations were indicated erroneously in the original paper.) To illustrate better the various collision mechanisms, two projections of the ideal hcp lattice—whose c/a ratio of $(8/3)^{1/2}$ corresponds very closely to that of cobalt, $c/a = 1.63$—are shown in Fig. 36; in the upper part the basal plane is viewed along the c axis, in the lower part the $(11\bar{2}0)$ plane is viewed perpendicular to the c axis.

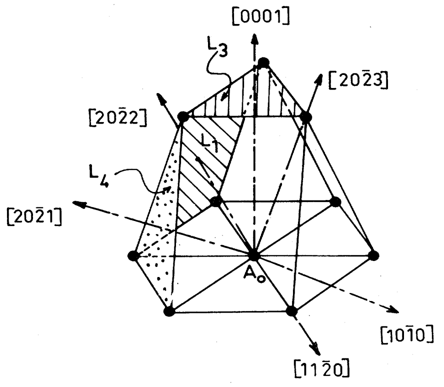

FIG. 35. Part of the hcp unit cell indicating several lenses and the corresponding propulsion directions of the atom A_0 across them (Maury *et al.*, 1973b).

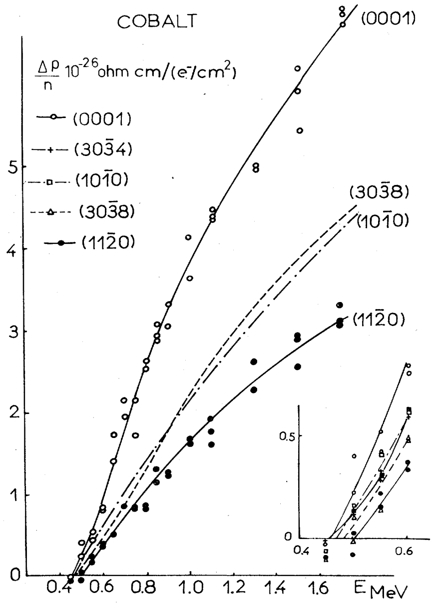

FIG. 34. Resistivity change rates of cobalt crystals of various orientations as a function of electron energy (Maury *et al.*, 1973a).

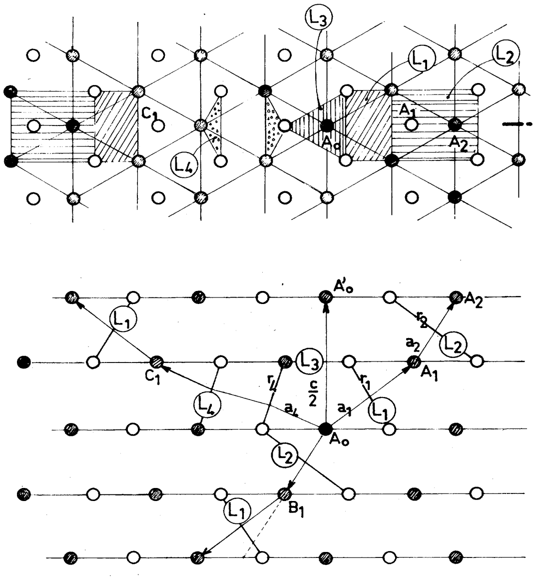

FIG. 36. Two views of the hcp lattice. Above: view along the c axis; below: view perpendicular to the c axis cut parallel to the $(11\bar{2}0)$ plane. Indicated are several of the lenses of Fig. 35. Filled circles represent atoms in the paper plane, open circles in the plane above or below it (Maury *et al.*, 1973b).

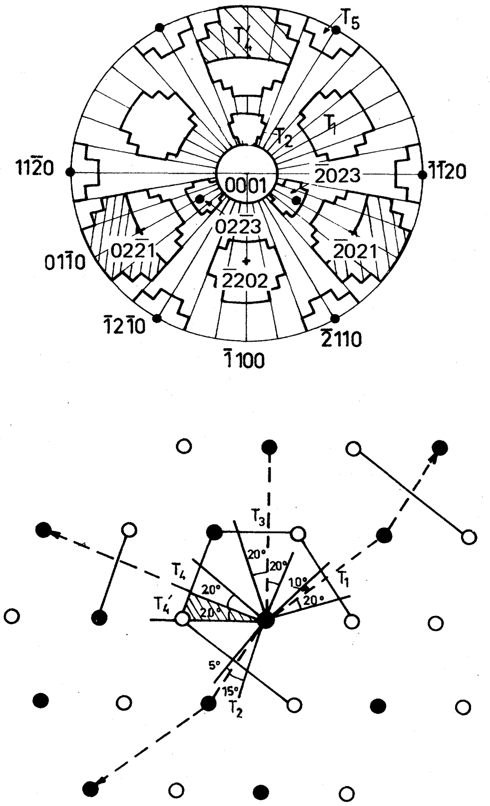

FIG. 37. Above: stereographic projection of the T_d surface in an hcp crystal viewed along the c axis. Below: cut parallel to $(11\bar{2}0)$ indicating the opening angles of the windows (Maury *et al.*, 1973b).

Indicated are the trajectories of the knocked-on atom A_0 across several of the lenses of Fig. 35. One notices among other things: (1) the symmetrical passage through the two rectangular lenses L_1 and L_2: $L_1-L_2-L_1$, etc; (2) the double passage through two triangular lenses L_4 before colliding with the next atom—a situation analogous to that of an atom knocked into the $\langle 111\rangle$ direction in an fcc lattice; (3) the close-packed $\langle 11\bar{2}0\rangle$ sequence.

Starting from this purely geometrical picture the authors constructed a trial threshold energy surface whose form and angular dimensions are shown in Fig. 37. (The shape of the potential windows is that used in the integration of the cross sections.) The T_i's are the depths of the potential minima of the lenses L_i corresponding to the true threshold energies for displacement through these lenses. As a next step, the displacement cross section σ was calculated; by varying the T_i's, the authors tried to reproduce the shapes and the relative positions of the experimentally determined resistivity change rates (Fig. 34). The best fit is shown in Fig. 38: the qualitative agreement in the main features is quite satisfactory. This fit was obtained using the T_d set indicated in the insert of the Fig. 38: $T_d^{\langle 0001\rangle} = T_3 = (40\pm 3)$ eV, $T_d^{\langle 20\bar{2}3\rangle} = T_2 = (23\pm 2)$ eV, $T_d^{\langle 20\bar{2}2\rangle} = T_1 = (22\pm 1)$ eV, $T_d^{\langle 20\bar{2}1\rangle} = T_4 = (40\pm 5)$ eV, and $T_d^{\langle 11\bar{2}0\rangle} = T_5 = (27\pm 2)$ eV; all intermediate orientations were given a $T_d > 150$ eV.

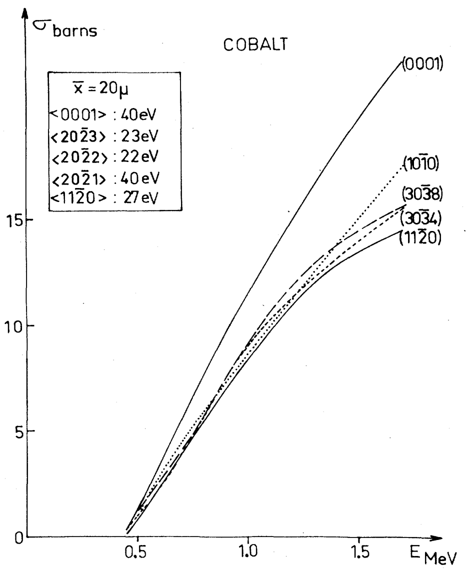

FIG. 38. Computed displacement cross sections in various directions of a cobalt crystal such as to match the experimental data of Fig. 34 (Maury *et al.*, 1973b).

Let us now discuss the physical meaning of these results. The easiest passages are those across the two big rectangular lenses L_1 and L_2. (Actually, L_2 is a quasi-focusing direction, in the sense that the distance between the knock-on atom A_0 and the next atom B_1 across L_2 is quite small; afterwards, however, the chain breaks loose, cf. Fig. 36.) As expected, the focusing direction $\langle 11\bar{2}0\rangle$ has also a relatively low T_d, though somewhat higher than in Howe's experiment (1970); this might be due to the rather high impurity concentration of the specimens, which could impede the propagation of long-range focusing chains. The thresholds for displacement across the two triangular lenses L_3 and L_4 are both quite high. In an ideal hcp lattice such as that of cobalt, their sizes are identical, justifying the same values for their T_d's. The greater distance to the second knock-on atom across $L_4, \overline{A_0C_1}$, as compared to $\overline{A_0A_0'}$ across L_3, is compensated by a second lens L_4, which narrows the effective opening angle of this passage. In fact, as is indicated in Fig. 37, the window L_4 is divided into two regions: one with a threshold T_4, the other with a threshold T_4', which can be larger or smaller than T_4, thus expressing the asymmetry of the passage through both lenses L_4 allowing it only for the right angular combination. (As will be shown below, the situation is quite different in the cases of zinc and of cadmium.) The apparent disagreement with Howe's measured $T_d^{\langle 0001\rangle} = 33$ eV is easily explainable by the $\cos^2$ effect: indeed, considering that $33 = 22/\cos^2 35°$, a $T_d = 33$ eV observed in the $\langle 0001\rangle$ direction can well be the manifestation of displacement processes initiated in the direction of the lens L_2, with a $T_d^{\langle 20\bar{2}3\rangle} \approx 23$ eV. Similarly, the $\langle 10\bar{1}0\rangle$ threshold observed at 30 eV can also be due to a real $T_d \approx 23$ eV in the $\langle 11\bar{2}0\rangle$ or in the $\langle 20\bar{2}2\rangle$ direction.

The fit between the computed displacement cross sections and the measured resistivity change rates being mainly qualitative, the determination of the Frenkel-pair resistivity is not very precise: the authors obtained $\rho_F^{\mathrm{Co}} = (15 \pm 5) \times 10^{-4} \Omega\mathrm{cm/FP}$. (The value of $30 \times 10^{-4} \times \Omega\mathrm{cm}$ given by Maury *et al.* (1973a) was estimated using an obsolete value of $\rho_0 = 10 \mu\Omega\mathrm{cm}$ for the specific resistivity of cobalt at room temperature as the basis for the determination of the sample-shape factor.)

b. Zinc

In the same series of experiments with cobalt, Maury *et al.* (1973a) investigated the threshold energy surface of zinc. They bombarded specimens cut parallel to the (0001), $(11\bar{2}0)$, and $(30\bar{3}4)$ planes, together with a polycrystalline specimen for comparison, with electrons in the energy range 0.4–0.9 MeV. The experimental results are presented in Fig. 39(a). In contrast to cobalt (Fig. 34), the (0001) sample exhibits the lowest resistivity change rates, while the $(30\bar{3}4)$ crystal shows the highest ones. The $(11\bar{2}0)$ sample and the polycrystal are nearly identical. A matching with cross sections, using the model described in the previous section, gave the best fit with the following set of basic thresholds: $T_d^{\langle 0001 \rangle} = T_3 = (19^{+2}_{-1})$ eV, $T_d^{\langle 20\bar{2}3 \rangle} = T_2 = (25 \pm 2)$ eV, $T_d^{\langle 20\bar{2}2 \rangle} = T_1 = (30 \pm 5)$ eV, $T_d^{\langle 20\bar{2}1 \rangle} = T_4' = (20 \pm 2)$ eV, and $T_d^{\langle 11\bar{2}0 \rangle} = T_5 = (14^{+2}_{-1})$ eV; for all intermediate directions $T_d > 55$ eV. The fit is shown in Fig. 39(b) and proves the agreement to be very close. One notes that, this time, the lowest threshold is $T_d^{\langle 11\bar{2}0 \rangle}$, conforming to expectations for displacements along this dense collision chain. T_3 and T_4 are again—as in the case of cobalt—practically the same; they are, however, now lower than the highest thresholds T_1 and T_2 for passage through the rectangular lenses L_1 and L_2 (Figs. 35 and 36). Thus, it seems that the lattice extension along the c axis in zinc favors displacements through the triangular lenses L_3 and L_4, probably acting upon the stability of the resulting Frenkel pairs. (More arguments, showing that the minimum vacancy-interstitial separation distance in the $\langle 20\bar{2}3 \rangle$ and $\langle 20\bar{2}2 \rangle$ directions is bigger in zinc than in cobalt, will be given in Sec. V.) The correlation between Figs. 39(a) and (b) led to a Frenkel-pair resistivity $\rho_F^{\mathrm{Zn}} = (20 \pm 3) \times 10^{-4} \Omega\mathrm{cm/FP}$. Reconsiderations of the potential window sizes in the Zn lattice indicate a lower ρ_F, of the order of $(15 \pm 5) \times 10^{-4} \Omega\mathrm{cm/FP}$.

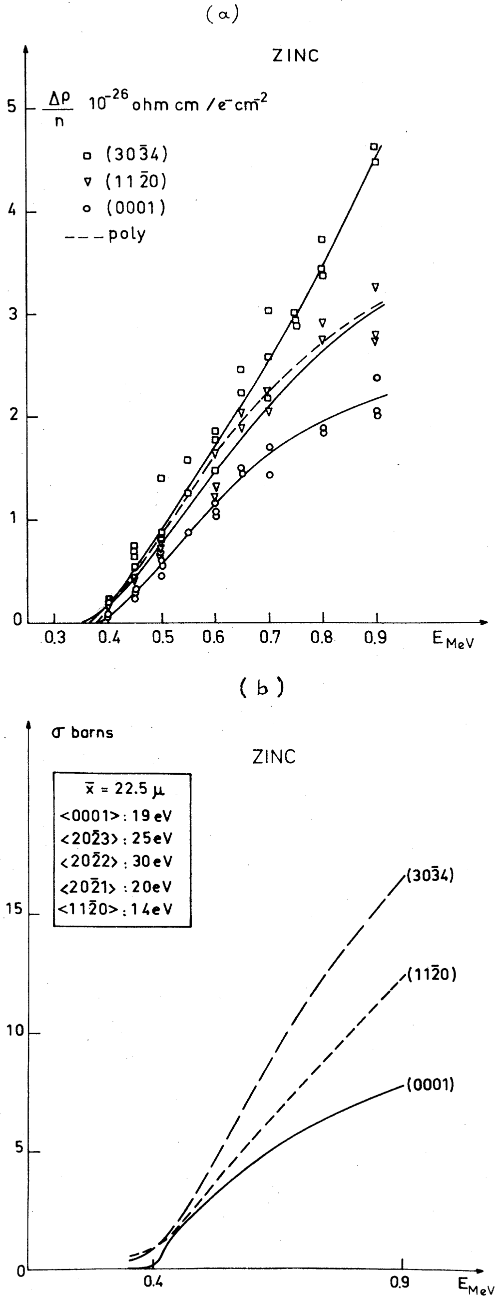

FIG. 39. (a) Experimental resistivity change rates for several zinc crystals as a function of electron energy (Maury *et al.*, 1973a); (b) corresponding computed displacement cross sections with the best-fit set of T_d's (Maury *et al.*, 1973b).

In their electron-microscope investigation, Mitchell *et al.* (1975) report preliminary results concerning the irradiation of a (0001) zinc specimen. Their measured E_d was 340 keV, corresponding to a threshold value of 15 eV. This is lower than the $T_d^{\langle 0001 \rangle} = 19$ eV of the Orsay experiment, but close to their $T_d^{\langle 11\bar{2}0 \rangle} = 14$ eV. Again, one wonders about the comparability of high-temperature microscope observations and low-temperature resistivity measurements.

c. Cadmium

Cadmium is the third hcp crystal investigated by Maury *et al.* (1973a, b). They irradiated (0001), $(11\bar{2}0)$, and $(30\bar{3}8)$ specimens with electrons of 0.6 to 1.0 MeV energy and measured the resistivity change rates. Because of the very high specimen purity (residual resistivity ratios of several 10 000) the damage rates had to be corrected for the varying influence of the size effect in conduction-electron scattering. The corrected results are shown in Fig. 40(a). As in the case of zinc, the (0001) sample exhibits the minimum damage rates, while now the $(11\bar{2}0)$ specimen is that with the highest damage rates. The corresponding matching with the theoretical displacement cross sections gave a best fit with the thresholds T_i indicated in the insert of Fig. 40(b): $T_d^{\langle 0001 \rangle} = T_3 \gtrsim 40$ eV, $T_d^{\langle 20\bar{2}3 \rangle} = T_2 \gtrsim 35$ eV, $T_d^{\langle 2022 \rangle} = T_1 \gtrsim 35$ eV, $T_d^{\langle 20\bar{2}1 \rangle} = T_4 = (19 \pm 1)$ eV, $T_d^{\langle 11\bar{2}0 \rangle} = T_5 = (21^{+2}_{-1})$ eV. In fact, it turned out that it was sufficient to adjust only T_4 and T_5, keeping the other T_i's above a certain value (35 to

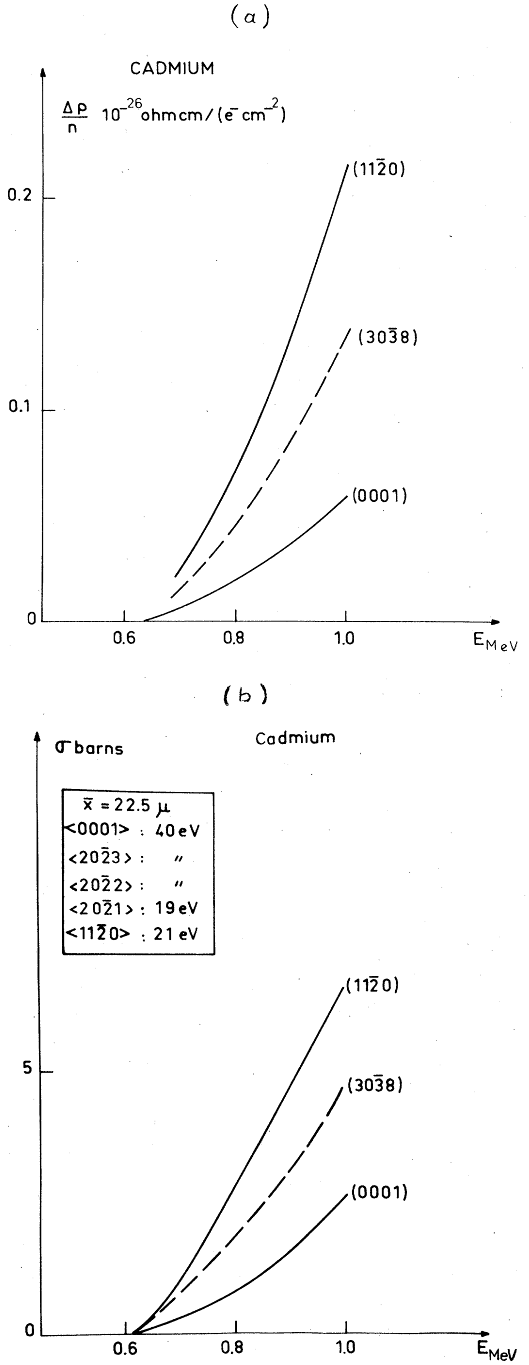

FIG. 40. (a) Size-effect corrected resistivity change rates for several cadmium crystals (Maury *et al.*, 1973a); (b) corresponding computed displacement cross sections with the best-fit set of T_d's (Maury *et al.*, 1973b).

40 eV), to obtain a satisfactory fit as shown in Fig. 40(b). Again, $(11\bar{2}0)$ is a local minimum in the threshold energy surface, together with a part of the triangular lens L_4; the other lenses do not show any noteworthy features.

This somewhat surprising result might be related to the abnormal recovery behavior of cadmium (see the discussion of this problem in Sec. IV.B.3.*c*.), which is similar to the behavior of gold (cf. Sec. IV.A.1.*c*); the very low recovery temperature of Frenkel pairs in cadmium might cause the annihilation of some particularly unstable pairs already during the irradiation—e.g., those created in the ⟨0001⟩ direction across L_3—giving a high apparent $T_d^{\langle 0001\rangle}$, while in reality the deduced T_3 represents a threshold for formation of a distant pair, separated by several L_3's. This is corroborated by the unusually low resistivity change rates [Fig. 40(a)] and the resulting low $\rho_F^{Cd} = (5 \pm 1)\times 10^{-4}\Omega$cm/FP, indicating the probable instantaneous annealing of a part of the damage.

B. Defect recovery

In this section, I shall discuss the results of annealing studies of irradiated crystals, giving particular emphasis to anisotropy manifestations in the recovery spectra of electron-bombarded crystals; some neutron radiation experiments giving pertinent information on defect symmetry will also be mentioned. Whenever possible the results will be compared with the defect production data taken from the preceding sections, in order to draw conclusions about the processes responsible for various substages of the recovery spectra.

1. Face-centered cubic lattice

a. Copper

The first attempt to observe an anisotropy in the resistivity-recovery spectrum of irradiated crystals was undertaken by Cusson *et al.* (1961) on copper whiskers. The results for (100) and (110) oriented specimens are shown in Fig. 41. Although the whisker thickness was rather large (125μ in diameter), one notes some anisotropy, namely a larger amount of total recovery during Stage I (supposed to be completed at ~60 K), as well as a larger substage I_B (at 25 to 28 K) for the (110) sample. Normalized to the total recovery at 60 K, the corresponding percentages annealed during the substages I_B, I_C (28 to 34 K), and I_{D+E} (34 to 60 K) amounted to: I_B, 10% for (100) and 18% for (110); I_C, 12% for (100) and 13% for (110); I_{D+E}, 78% for (100) and 69% for (110).

Additional data were obtained in the more detailed study by Sosin and Garr (1965), who had measured the percentages annealed during Stage I, for various bom-

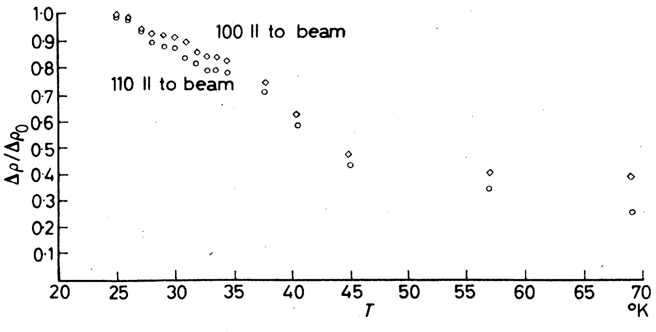

FIG. 41. Isochronal recovery of the damage in 1.2 MeV electron-irradiated copper whiskers (Cusson *et al.*, 1961).

TABLE III. Percentages annealed in Stage I of irradiated copper crystals (Sosin and Garr, 1965).

(*hkl*)	Anneal. stage	Energy/keV 900	750	750	650	600	500
(100)	I_A	1.4	1.0	0.7	2.8	5.1	2.9
	I_B	3.6	8.0	5.6	22.4	13.9	17.7
	I_C	11.0	12.2	13.1	8.5	17.7	15.4
	I_{total}	79.9	82.1	80.6	78.9	90.3	80.0
(110)	I_A	6.2	3.0		2.2	1.8	
	I_B	16.2	18.0		14.3	20.6	
	I_C	12.2	16.2		15.6	14.3	
	I_{total}	87.8	86.7		91.2	89.6	
(111)	I_A			1.8			0.8
	I_B			13.4			7.0
	I_C			11.7			17.3
	I_{total}			82.2			78.0

barding energies, as indicated in Table III. For the highest used electron energy of 900 keV, the results are qualitatively comparable to those of Cusson *et al.* (1961) in that they show a greater amount of recovery in I_{total} and in substage I_B for the (110) sample and similar values for the I_C recovery. More interesting is the energy dependence of the observed recovery anisotropy and, in particular, the data close to the threshold, at 500 and 600 keV. Except for the obviously anomalous measurements after the 650 keV irradiation, one notes in the case of the (100) crystal a strong decrease of the I_B substage with increasing energy, while the decreasing tendency of the I_C substage is much less pronounced. The (110) crystal exhibits a slowly decreasing I_B and a practically constant I_C substage, while the small I_A substage is clearly increasing with energy. In view of these qualitative observations, and in agreement with what we have learned from the anisotropy of defect production in copper (Sec. IV.A.1.*a*), it is tempting to attribute the I_B substage to the recovery of Frenkel pairs produced in the rather open and "easy" $\langle 100\rangle$ direction of the lattice. The I_C substage as well as the I_{D+E} substages would then be due to the annihilation of interstitials produced in the focusing $\langle 110\rangle$ direction. Close $\langle 110\rangle$ pairs would anneal in I_C, distant $\langle 110\rangle$ pairs in I_D, and interstitials which are too far removed from their own vacancies to be still correlated would disappear in I_E. Substage I_A is small and therefore might be attributed to close Frenkel pairs produced in "difficult" low-symmetry directions; hence their small separation distance resulting in a low activation energy and low annealing temperature, and also explaining the increasing importance of I_A with increasing atomic recoil energy. The preponderance of the I_{C+D+E} processes would stem from the great number of $\langle 110\rangle$ directions in the lattice and hence its easy accessibility for a knock-on. For a quantitative analysis and a less speculative attribution of the substages, one would have to irradiate even closer to the threshold (preferably not higher than 400 keV), in order to separate the two main displacement processes.

In a more recent study, Pruitt and Chaplin (1971) have also investigated the recovery of (100) and (110) copper crystals after 0.5 MeV electron irradiation. The differentiated spectra of Stage I recovery obtained in this work are shown in Fig. 42. The only clear manifestation of anisotropy is an enhanced I_B substage in the case of the (100) specimen. An immediate comparison with the Sosin and Garr (1965) data is not possible, since the latter authors had not irradiated (110) samples with 0.5 MeV electrons [in their discussion, Pruitt and Chaplin (1971) confused the (110) and (111) data of Sosin and Garr], but for their closest energy, 0.6 MeV, the effect is reversed as can be seen from Table III. It is not clear whether this is due to the much thicker specimens of Pruitt and Chaplin (~70μ), but it is certain that, for an assignment of I_B and I_C, one would have to irradiate at several different energies (including 0.4 MeV) and to use thinner crystals.

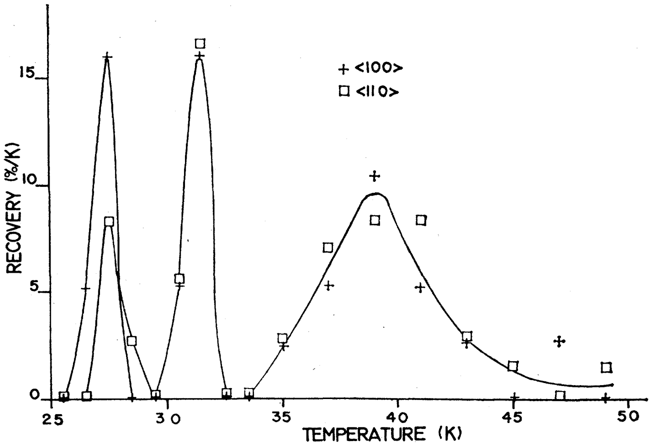

FIG. 42. Recovery spectra of two copper crystals after a 0.5 MeV electron irradiation (Pruitt and Chaplin, 1971).

As to the defect symmetry, diffuse x-ray scattering experiments (Ehrhart and Schlagheck, 1974) and measurements of the elastic constant changes (Rehn *et al.*, 1975) on irradiated copper crystals indicate that the probable stable form of the interstitial is the $\langle 100\rangle$ dumbbell configuration. These split interstitials would migrate towards the end of Stage I and agglomerate into clusters, unless annihilated.

b. Gold

The only annealing study performed with irradiated gold crystals was that by Ehrhart and Segura (1975) using diffuse x-ray scattering on 3-MeV electron bombarded specimens. In contrast to other fcc metals, the typical annealing Stage I ascribed to the recombination of Frenkel pairs and to the migration of interstitial atoms has not been observed in gold down to the lowest irradiation temperatures, 2 K (Gwozdz, 1973). It was, therefore, particularly interesting to learn whether individual interstitials were observed or not. Ehrhart and Segura (1975) showed clearly that no single interstitials (in particular, no $\langle 100\rangle$ split interstitials) existed in pure gold. Even for the lowest doses and at 5 K, they observed clusters of five to seven atoms. To explain this, they invoke either random interstitial diffusion during the irradiation or replacement collision chains of an average length of at least 25 lattice constants. The latter mechanism has been proposed as "radiation-induced diffusion" by Urban *et al.* (1974, 1975).

c. Aluminum

Exactly the type of experiment desired for an unambiguous assignment of substages in Stage I annealing was performed by Longshore and Chaplin (1969). These authors irradiated (100) and (110) aluminum crystals, together with a polycrystalline foil, with a series of electron energies starting right above the threshold of 16 eV, in the range 0.18 to 0.4 MeV. Two typical examples of the recovery spectrum of the induced resistivity change are shown in Fig. 43. The immediately striking feature is the strong anisotropy of the substage I_B (near 19 K): after low-energy irradiation [Fig. 43(a)], the (100) specimen recovers nearly five times more damage during I_B than the (110) sample; after the 0.3 MeV bombardment [Fig. 43(b)], the anisotropy is smaller but reversed—the (100) crystal has a smaller I_B substage than the (110) one; the polycrystal always exhibits an intermediate recovery.

To elucidate this energy dependence further, the authors plotted the percentage recovery during I_B as a function of the maximum transmitted energy to an aluminum atom during irradiation (Fig. 44). One notes that the amplitude of I_B decreases strongly with increasing T_m in the case of the (100) sample, while it increases for the (110) crystal. This tendency continues beyond the crossing point at $T_m \approx 28$ eV (corresponding to $E = 0.27$ MeV) until $T_m \approx 35$ eV, whereon both orientations exhibit slightly decreasing behavior analogous to the polycrystal. To account for this, the authors assume that the great majority of the displacements occur only along $\langle 100\rangle$ and $\langle 110\rangle$ directions. By irradiating a (100) sample with electrons only slightly above threshold one will create mainly $\langle 100\rangle$ defects; increasing the recoil energy will increase the opening angle of the accessibility cone around the direction of incidence, resulting in a greater number of $\langle 110\rangle$ defects and a corresponding decrease in the $\langle 100\rangle$ defect concentration. Analogously, if $\langle 110\rangle$ is the primary radiation direction, the number of $\langle 100\rangle$ defects will increase with increasing T_m. Because there are four (110) windows around a $\langle 100\rangle$ direction and only two (100) windows around a $\langle 110\rangle$ direction, the energy dependence of the (100) crystal will be twice as strong. For recoil energies $T_m \gtrsim 2T_d$, all the directions become accessible, the energy dependence loses its particularity, and all the orientations behave

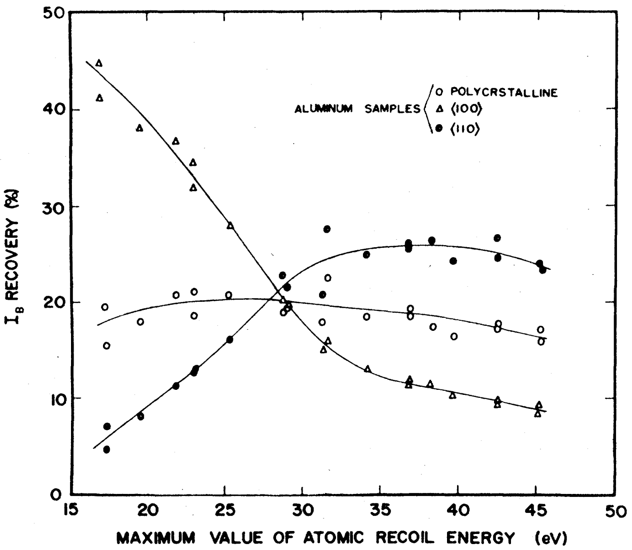

FIG. 44. Fractional amount of I_B recovery for various aluminum specimens as a function of the maximum transmitted energy (Longshore and Chaplin, 1969).

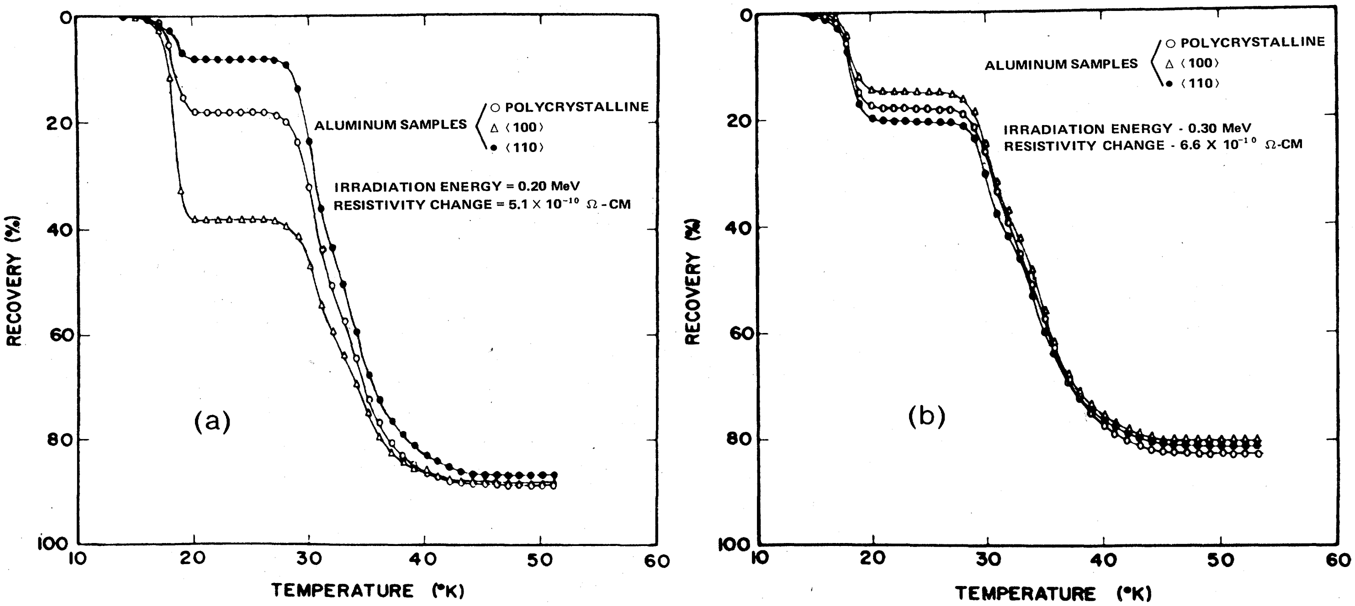

FIG. 43. Stage I recovery of mono- and polycrystalline aluminum samples following an irradiation with (a) 0.2 MeV, (b) 0.3 MeV electrons (Longshore and Chaplin, 1969).

like polycrystals. This is exactly the observed behavior for substage I_B (Fig. 44), qualifying I_B as a certain candidate for the annealing of ⟨100⟩ Frenkel pairs. The remaining I_{C+D+E} defects will then be due to displacements in the ⟨110⟩ directions. More recently, Chaplin (1974) has given a more explicit and quantitative analysis along the same lines.

It is rather comforting that the interpretation of the aluminum results by Longshore and Chaplin (1969) is consistent with the arguments developed in the preceding subsection for the understanding of the annealing results in copper obtained by Sosin and Garr (1965), in particular the attribution of I_B to the recovery of ⟨100⟩ Frenkel pairs.

Finally, Ehrhart *et al.* (1974) have determined by diffuse x-ray scattering experiments on irradiated crystals that the interstitial in aluminum had the symmetry of a ⟨100⟩ split dumbbell, and that the crowdion configuration could be excluded. The same conclusions were reached as a result of a study of the elastic aftereffect in electron-irradiated (100) and (111) crystals (Spirič *et al.*, 1975).

d. Nickel

The recovery spectrum of the induced resistivity change in nickel crystals was studied by Copé (1969), who irradiated the orientations ⟨100⟩, ⟨110⟩, and ⟨111⟩ at 20 K by electrons of 3 MeV energy. He applied a linear temperature elevation regime which, after comparison with a nonirradiated specimen, gave a recovery spectrum analogous to an isochronal one (Fig. 45). The substage I_B (~ 29 K) is too small for us to draw any conclusions, but the substage I_C (centered around 44 K) exhibits a rather pronounced anisotropy: 15.5% recovery in the case of the (100) sample, 13% for the (111), and 11.5% for the (110) crystals. There seems to be very little orientation dependence in Stage I_{D+E} (50–67 K). Using a model established by Peretto (1967) for the interpretation of his magnetic aftereffect measurements on polycrystalline nickel, which attributes the substage I_C to the annealing of a ⟨100⟩ dumbbell in a fifth-neighbor site [position (310) with respect to the vacancy], Copé assigns I_C to defects produced in the direction ⟨100⟩. It is not possible to confirm or to refute this assignment from his single-crystal experiments, since the electron energy of 3 MeV is far too high for selective defect production. As we have seen in the preceding sections on copper and on aluminum, the energy dependence of the recovery anisotropy is essential for the attribution of substages to specific processes.

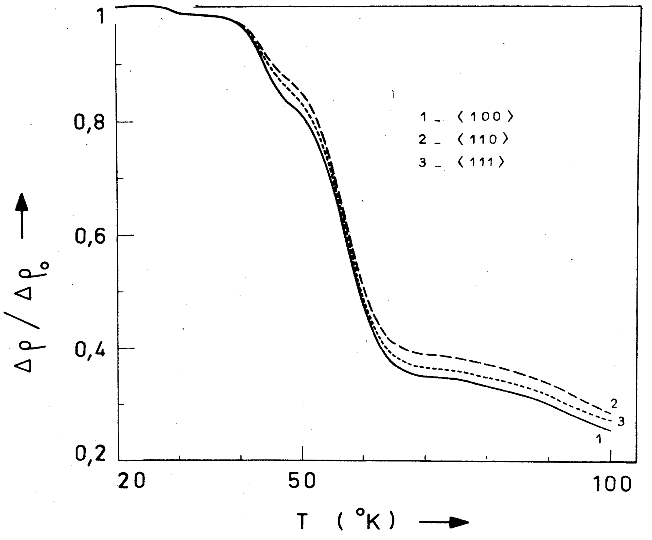

FIG. 45. Resistivity recovery of three different nickel crystals (Copé, 1969).

Through magnetic anisotropy measurements (cf. Sec. III.E), Forsch *et al.* (1974) were able to establish that in electron-irradiated nickel crystals the Stage I defects were ⟨100⟩ split interstitials. Subsequent recovery measurements throughout substages I_{C+D+E} also gave maximum signals when magnetizing in a ⟨100⟩ direction, suggesting that the dumbbells migrated freely by a three-dimensional jump mechanism.

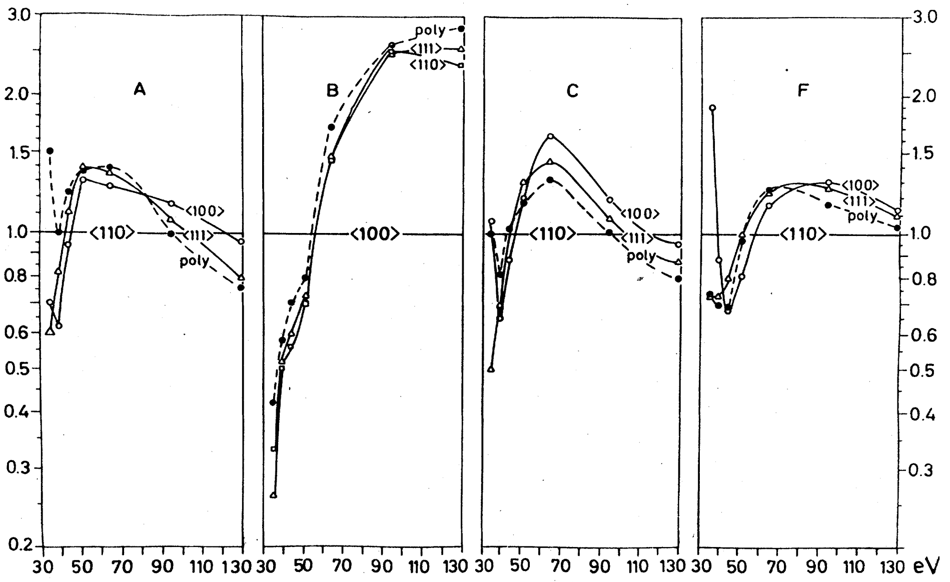

FIG. 46. Normalized production rates of defects recovering in substages I_A, I_B, I_C, and above I_C, respectively, in platinum as a function of maximum transmitted energy and of irradiation direction (Jung and Schober, 1975).

e. Platinum

Jung and Schober (1975) have irradiated platinum crystals of different orientations with electrons of energies between 1.4 and 3.0 MeV, i.e., in the recoil energy range 37 to 133 eV ($T_d^{\min}$ to $3.5T_d^{\min}$). Subsequent annealing experiments through Stage I showed a strong dependence of the recovery on energy and crystal orientation, as illustrated in Fig. 46. Here are plotted the normalized production rates of defects annealing in the substages at 9–11 K, 14–16 K, 19–22 K, and above 22 K, labeled A, B, C, and F, respectively. For recoil energies T_m below ~50 eV, the production of close-pair defects was strongly favored; moreover, Fig. 46 indicates that A and C defects are most probably created near the ⟨110⟩ directions, while B defects are rather ⟨100⟩-type pairs. The authors established a connection to the threshold energy surface (whose profile is shown in Fig. 22) and related the defects to the minimum regions (shaded areas) in the T_d surface. Thus, slightly above $T_d^{\min}$, $T \lesssim 40$ eV, defect B stems from a region 20° off ⟨100⟩ on the ⟨100⟩-⟨111⟩ boundary, while defects A and C lie in the ring 10° off ⟨110⟩. For higher T, 40-50 eV, defects A tend to vanish, while the rest (mainly F and C) increase.

2. Body-centered cubic lattice

a. Alpha-iron

Cusson *et al.* (1961) irradiated iron crystals in the form of whiskers with 1.2-MeV electrons incident parallel to the ⟨100⟩ and the ⟨110⟩ orientations. Figure 47 shows the resistivity recovery of the two orientations during Stage I. One notes enhanced recovery for the total Stage I of the (110) specimen, but the relative amplitudes of the four observed substages do not differ much for the two crystals. This is not too surprising, since the whisker thickness (125μ) is large enough and the transmitted energies high enough to smear out anisotropy manifestations.

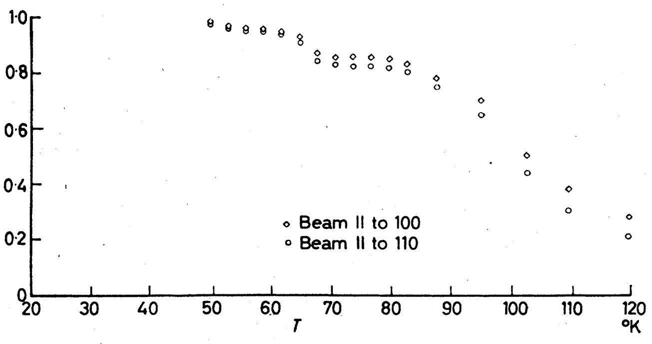

FIG. 47. Isochronal recovery of induced resistivity in oriented iron whiskers; the measurements were done at 20 K (Cusson *et al.*, 1961).

In their recent study of damage anisotropy in iron crystals, Maury *et al.* (1976) also investigated the recovery spectrum of the three principal orientations, ⟨100⟩, ⟨110⟩, and ⟨111⟩. They observed a strongly energy-dependent anisotropy of the first important substage, I_B, at 60–70 K. After irradiation with 0.4-MeV electrons—just above threshold—this substage was maximum for the (100) sample and minimum for (111), Fig. 48(c). Increasing the energy [Fig. 48(b)] gives less recovery for the (100), and more for the (111) crystal, leading to complete inversion for $E = 0.65$ MeV [Fig. 48(a)]. This means that substage I_B is caused by the recovery of close pairs created in the ⟨100⟩ direction. The next substage, I_C, does not depend much on the orientation, in contrast to the following, I_{D+E}, which, in fact, compensates the anisotropy of I_B. Furthermore, the width of I_D indicates that it is not a simple substage but consists of at least two subpeaks. Thus it is suggested that the correlated recovery, supposed to occur during I_D, stems from closer ⟨100⟩ pairs in its first part and from more distant ⟨111⟩ pairs in its second part (and probably during I_E). The authors tried to make substage attributions by comparing the respective annealed percentages to the calculated partial displacement cross sections (cf. the next section on molybden-

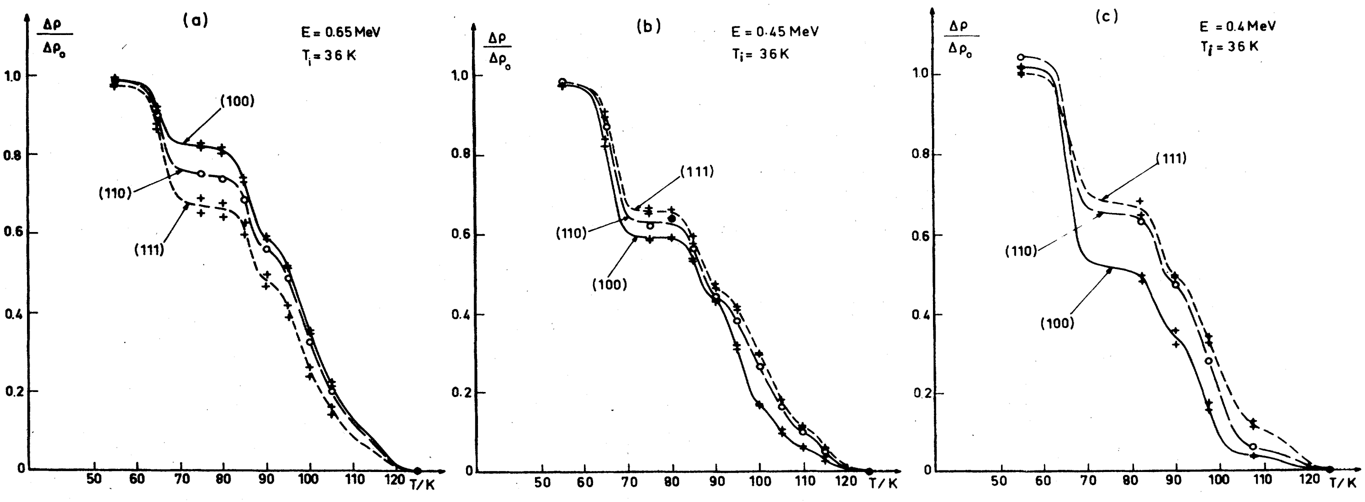

FIG. 48. Normalized recovery spectra of iron crystals irradiated with electrons of: (a) 0.65 MeV, (b) 0.45 MeV, and (c) 0.4 MeV energy (Maury *et al.*, 1976).

TABLE IV. The contributions of the ⟨111⟩ displacements to the total cross section for displacement computed with various $T_d^{\langle 100\rangle}$ and $T_d^{\langle 111\rangle}$ compared with the recovery (normalized to 125 K) during the second part of substage I_{D+E}: case (a), and with the recovery during the substage I_C *plus* the second part of I_{D+E}: case (b), for three iron crystals at various electron energies (Maury *et al.*, 1976).

		(a)		(b)	
E/MeV	(hkl)	$\sigma(111)$ in % with $T_d^{\langle 100\rangle}=17$ eV and $T_d^{\langle 111\rangle}=20$ eV	% $\Delta\rho/\Delta\rho_{125\text{ K}}$ at 100–125 K	$\sigma(111)$ in % with $T_d^{\langle 100\rangle}=16.5$ eV and $T_d^{\langle 111\rangle}=19$ eV	% $\Delta\rho/\Delta\rho_{125\text{ K}}$ at 75–90 K plus 100–125 K
0.4	(100)	9	8	18.5	26
	(110)	19.5	19	33.5	37
	(111)	32	25	47	43
0.45	(100)	30	17	36.5	33
	(110)	41.5	27	45.5	45
	(111)	49.5	30	50.5	49
0.65	(100)	69	35	71.5	59
	(110)	46.5	33	47.5	52
	(111)	35	25	36	44

um). Table IV represents such an attempt for the ⟨111⟩ displacements, slightly varying the basic thresholds. The agreement in case (b) being somewhat more satisfactory, this would imply that the defects which recover during I_C, at 75–90 K, are close pairs produced in the ⟨111⟩ direction.

Moser *et al.* (1973) have performed internal friction measurements on neutron-irradiated (100) and (110) iron crystals. As is seen in Fig. 49, the 125 K peak, which had been attributed to the three-dimensional migration of the free interstitial, shows up for both orientations and can, therefore, not be due to a ⟨100⟩ oriented defect. On the other hand, the authors observed in magnetic aftereffect experiments a strong ⟨100⟩ character of this peak. The discrepancy may be understood through the fact that elastic and magnetic measurements detect a local perturbation which has an interaction range varying according to the employed technique: the size and, especially, the shape of the perturbation volume will not be the same. Thus the ⟨110⟩ split interstitial results in a strain ellipsoid with the principal axes $\lambda_1 \neq \lambda_2 \neq \lambda_3$, while the magnetic perturbation is represented by a parallel ellipsoid whose principal axes are $\epsilon_1 = \epsilon_2 \neq \epsilon_3$, indicating an apparently higher defect symmetry.

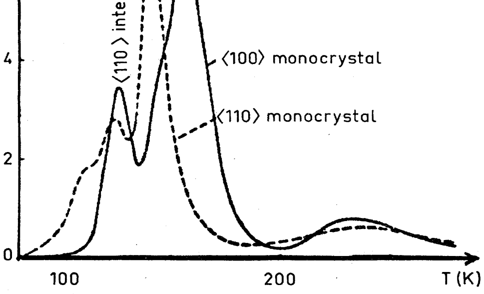

FIG. 49. Internal friction peaks of neutron-irradiated iron crystals (f=1 Hz) (Moser *et al.*, 1973).

b. Molybdenum

Subsequent to the detailed defect production study described in Sec. IV.A.2.*d*, Biget *et al.* (1974) also investigated the Stage I recovery spectra of various molybdenum crystals irradiated with 1.1-MeV and 1.7-MeV electrons. The recovery rates for the four irradiated orientations, ⟨100⟩, ⟨110⟩, ⟨111⟩, and ⟨112⟩, are shown in Fig. 50. The observed anisotropy of the substages, varying between the two extremes ⟨100⟩ and ⟨111⟩, is really striking: after the low-energy irradiation (1.1 MeV corresponds to $T_{\max}$= 52 eV, i.e., ~$1.5T_d^{\min}$), the substages I_1 (near 15 K) and I_4 (~40 K) have maximum amplitudes for the ⟨100⟩ orientation and minimum for the (111) crystal; substage I_2 (20 to 30 K) behaves inversely. For the high-energy case ($T_{\max}$= 3 $T_d^{\min}$), the whole situation is reversed.

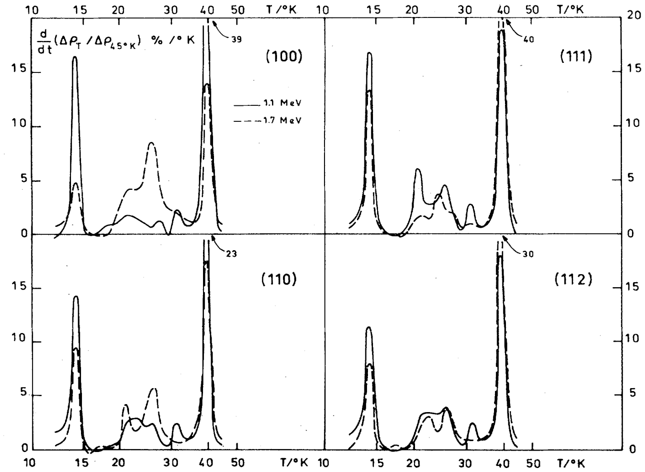

FIG. 50. Resistivity recovery rate spectra of various crystal orientations in molybdenum after irradiation with 1.1 and 1.7 MeV electrons (Biget *et al.*, 1974).

TABLE V. Recovery (normalized to 45 K) during substages I_1 to I_4 for various molybdenum crystals and the contributions of ⟨100⟩ and ⟨111⟩ displacements to the total cross sections in a given direction, in % (Maury *et al.*, 1975).

(*hkl*)	*E*/MeV	I_1 10–15 K	I_2 20–30 K	I_3 30–33 K	I_4 35–45 K	I_1+I_4	$\sigma(100)$	I_2+I_3	$\sigma(111)$
(100)	1.1	18	10	5.5	65.5	83.5	86.8	15.5	13.2
	1.7	7.5	48.5	2	36.5	44	19.5	50.5	80.4
(110)	1.1	17.5	18.5	6	54.5	72	72.5	24.5	27.5
	1.7	9.5	32	2	53	62.5	55.3	34	44.4
(112)	1.1	17.5	25.5	7	49	66.5	69.3	32.5	30.7
	1.7	10.5	22	2	62	72.5	64.2	24	35.6
(111)	1.1	16.5	30.5	7.5	42.5	59	56.7	38	43.3
	1.7	12.5	18.5	2.5	63.5	76	87.9	21	12.1

One can try to relate the percentages annealed during the various substages of Stage I with the cross sections for defect production in various crystal directions, since the amplitudes of the recovery peaks should depend directly on the concentration of interstitials created in certain configurations of more or less distant Frenkel pairs. This has been done using the T_d surface of Sec. IV.A.2.*d*, and the result is presented in Table V. As it followed from the displacement model that defect production was based on only two major displacement mechanisms [across the (100) and the (111) windows], the substages showing analogous energy dependence were grouped together. If one considers the low-energy results, one is immediately struck by the very strong correspondence between the measured percentages and the computed cross-section ratios. This induced the authors to attribute substages I_1 and I_4 to the annealing of ⟨100⟩ pairs, while I_2 and I_3 would correspond to ⟨111⟩ displacements. For high transmitted energies, the agreement is much less satisfactory, though the qualitative trends are maintained. The discrepancy is not surprising, since the rather idealized displacement model does not take into account secondary displacements which might occur in directions different from that of the initial knock-on. Thus, in the (100) crystal, there are more ⟨100⟩ pairs and fewer ⟨111⟩ pairs produced than predicted; for the (111) specimen, the effect is reversed. This is readily understood if one considers the relative cross sections in the two directions, which are related to the number and size of the corresponding windows, and the fact that $T_d^{\langle 100\rangle} < T_d^{\langle 111\rangle}$. The results for the (110) and (112) crystals are intermediate and form a smooth transition between the two extremes.

The above data give rise to an interesting question: why is there more than one substage related to each of the displacement mechanisms? A qualitative interpretation has already been given by Maury *et al.* (1975), who suggested that the resulting ⟨110⟩ split interstitial can assume various configurations. Thus a [100] displacement may give rise to a [110] dumbbell, at 45° from [100], or to a [011] configuration, at 90° from [100]. It seems plausible that the two interstitials—though at the same distance from their vacancies—will need different activation energies to move towards them. Similarly, a [111] event may lead either to a configuration $[1\bar{1}0]$ (perpendicular to [111]) or to [110] (*not* perpendicular). Very recently, this idea was confirmed by computer calculations of the configurational energy of various types of Frenkel pairs in a molybdenum crystal (Maury, Lucasson, 1976). In particular, it was found that, for pairs created in the [100] direction, the [011] configuration has a decreasing energy as the interstitial gets closer to the vacancy, while in the case of the [110] configuration the energy decreases as the interstitial moves away from it. Hence, substage I_1 was attributed to the annihilation of the former pairs; the latter configurations, tending to move away from their vacancies, would be eventually converted into more stable but distant pairs, which would give rise thereafter to correlated or free migration of interstitials. Substage I_4 is then attributable to the correlated interstitial migration. A qualitatively similar picture was observed for the ⟨111⟩ pairs, though the situation is somewhat complicated by the appearance of a possibility for the interstitial to exist in a body-centered position.

Further evidence for the ⟨110⟩ dumbbell as the interstitial configuration in Stage I of molybdenum has been presented by Okuda (1973, 1975) from dislocation pinning experiments on neutron-irradiated crystals and by Ehrhart (1975) from diffuse x-ray scattering measurements on electron-bombarded crystals.

c. Tungsten

In a detailed investigation of the resistivity recovery in 3-MeV electron-bombarded tungsten, Dausinger and Schultz (1975) have—among other parameters—also varied the crystal orientation with respect to the incident beam. The entire annealing spectrum up to room temperature is presented in Fig. 51. One notices clear anisotropy manifestations for the substages at 11 K, 17 K, and 30 K, and somewhat less pronounced evidence at ~40 K. The anisotropy is strongest for the important peak at 17 K: here, the (100) orientation exhibits the largest amplitude and the (111) crystal the smallest. For the other substages, the anisotropy is reversed: the (111) specimens always show maximum recovery and the (100) orientation minimum values. It is a pity that the authors could not irradiate closer to the threshold (3 MeV corresponds to $T_{\max} = 140$ eV

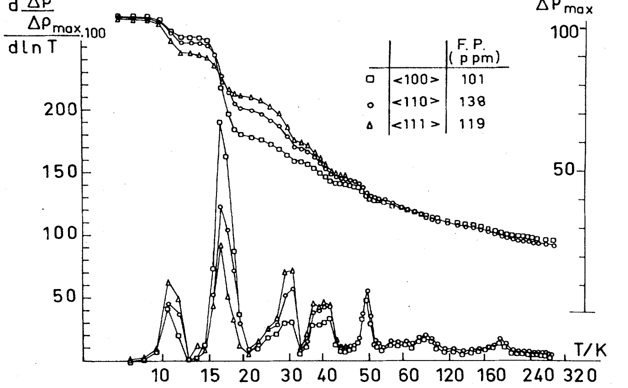

FIG. 51. Resistivity recovery rates of various crystal orientations in tungsten after 3 MeV electron irradiation (Dausinger and Schultz, 1975).

$\approx 3T_d^{min}$), in order to show the energy dependence of this anisotropy, but we can at least compare their results with the high-energy values obtained for molybdenum as presented in Fig. 50. It is interesting to note that in both cases one has anisotropy inversion for the second main substage when compared to the first and to the third ones. The W peaks at 11 and 30 K and the Mo peaks at 15 and 40 K behave quite similarly. Since Dausinger's experiments established all of the mentioned anisotropic tungsten substages as due to first-order processes, there is good reason to transpose the molybdenum analysis of the preceding section to tungsten: the peaks at 11 and 30 K would be due to the recovery of ⟨100⟩ pairs of different configurations; the substage around 17 K would be attributable to the annealing of ⟨111⟩ pairs. Such a transposition is also supported by the fact that configuration analysis (Maury and Lucasson, 1976) has shown the results to depend very little on the actual interatomic potential chosen for the calculations, i.e., the results are typical for the lattice structure of the crystal. It would, of course, be desirable to have a complete orientation- and energy-dependent defect production study in tungsten, to be able to compare the partial displacement cross sections with substage amplitudes as has been done for molybdenum, but already the 3-MeV data prove that the damage anisotropy follows the same order as for molybdenum (cf. insert of Fig. 51).

Preliminary data obtained recently by Biget *et al.* (1977b) on *W* crystals irradiated by 1.75 MeV electrons, i.e., very close to the threshold, confirm the above analysis. In particular, they show an inverse anisotropy as compared with Dausinger's results: the two peaks at 11 K and 30 K are biggest for the (100) orientation, while the recovery during the 17 K substage is strongest for the (111) crystal—exactly as in the case of molybdenum.

As for the defect symmetry, internal friction experiments (Okuda, 1975) on fast-neutron-irradiated tungsten crystals show that the interstitial has the form of the ⟨110⟩ dumbbell, though there is some controversy as to the substage in which it performs its long-range migrations (Dausinger *et al.*, 1975a,b,c; Okuda, 1975; Seidman *et al.*, 1975).

3. Hexagonal close-packed lattice

The only detailed anisotropy investigation of recovery in irradiated hcp crystals has been performed by the Orsay group following their defect production study on cobalt, zinc, and cadmium (treated in Sec. IV.A.3.); their results are presented below.

a. *Alpha-cobalt*

The first observation of orientation dependence of recovery in an hcp crystal was made on cobalt (Maury *et al.*, (1970). There it was shown that the two extremal orientations were $\langle 11\bar{2}0\rangle$ and ⟨0001⟩, the former exhibiting predominant recovery during the earlier substages of Stage I, the latter towards the end of it. The subsequently obtained detailed results (Maury *et al.*, 1973a) are presented in Fig. 52. They are plotted in order of growing angle between the incident electron direction and the *c* axis of the crystal: (0001), $(30\bar{3}8)$, $(30\bar{3}4)$, $(10\bar{1}0)$, and $(11\bar{2}0)$. This happens also to be the order in which the substage anisotropy develops (and, by the way, also the order of the defect production curves, cf. Fig. 34); the total recovery at ~50 K is strongest for the (0001) crystals and weakest for the $(11\bar{2}0)$ one. The behavior of the most important recovery peak I_C, centered at 33 K is significant. This peak is itself decomposable into two subpeaks, which conduct themselves in an interesting way when going from one orientation to another: at 0.7 MeV, one observes the appearance of a shoulder for the $(30\bar{3}8)$ and $(30\bar{3}4)$ samples, which develops to a distinct peak at 31 K for $(10\bar{1}0)$ and becomes preponderant in the case of the $(11\bar{2}0)$ crystal. A regular evolution is also seen for the 26 K peak, which has its maximum amplitude for the $(11\bar{2}0)$ orientation and its minimum for the (0001) crystal; the peak at 38 K is greatest for the (0001) and $(30\bar{3}8)$ crystals and smallest

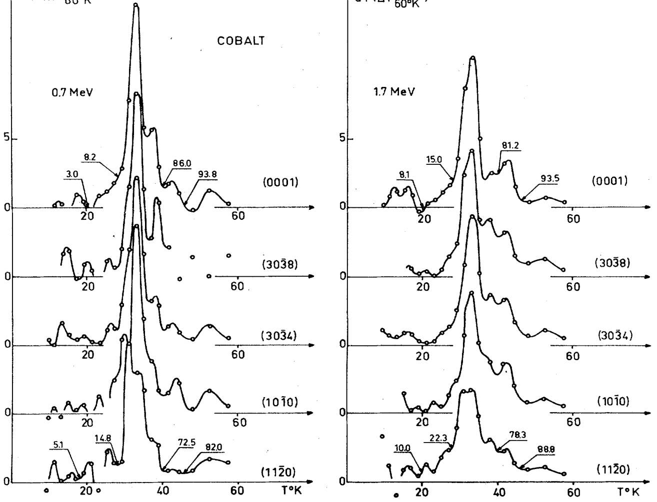

FIG. 52. To 60 K normalized resistivity recovery rate spectra of various crystal orientations in cobalt after 0.7 and 1.7 MeV electron bombardment. The numbers indicate the normalized percentage annealed at the corresponding temperature (Maury *et al.*, 1973a).

TABLE VI. Percentages annealed (normalized to 60 K) of induced resistivity change in 0.7 MeV electron-irradiated cobalt crystals, together with the partial cross sections for displacement through the various windows of the T_d surface (Maury *et al.*, 1973a, b).

Sample	10–20 K	20–28 K	28–32 K	32–35 K	35–40 K	40–60 K	$\langle hkil\rangle$	T_d/eV	$\sigma^{\langle hkil\rangle}/\%$
(0001)							$\langle 0001\rangle$	40	9
							$\langle 20\bar{2}3\rangle$	23	44
	3	5	15	47	16	14	$\langle 20\bar{2}2\rangle$	22	46
							$\langle 20\bar{2}1\rangle$	40	0
							$\langle 11\bar{2}0\rangle$	27	1
$(11\bar{2}0)$							$\langle 0001\rangle$	40	0
							$\langle 20\bar{2}3\rangle$	23	10.5
	5	13	27	20	7	28	$\langle 20\bar{2}2\rangle$	22	77
							$\langle 20\bar{2}1\rangle$	40	2
							$\langle 11\bar{2}0\rangle$	27	10.5

for the $(11\bar{2}0)$ specimen. At higher energies, the anisotropy is reduced.

This separation in annealing behavior occurring right through the I_C peak might be a qualitative indication as to the origin of the various substages. In Table VI are assembled, for the crystals of (0001) and of $(11\bar{2}0)$ orientation, the normalized percentages annealed in various recovery regions and the partial cross sections for displacement into the different windows of the (0001) and the $(11\bar{2}0)$ crystal, respectively. (The latter values were taken from calculations using the T_d surface of Sec. IV.A.3.*a*.) Although electrons of an energy of 0.7 MeV transmit a $T_{\max}=44$ eV, i.e., twice the minimum threshold energy, one can still observe some qualitative correlations between the cross sections and the experimental annealing data. It is clear that most defects are produced through the two rectangular windows with the lowest T_d, L_1 and L_2, (i.e., in the directions $\langle 20\bar{2}3\rangle$ and $\langle 20\bar{2}2\rangle$), $\sigma\langle 20\bar{2}3\rangle+\sigma\langle 20\bar{2}2\rangle\approx 90\%$, while the directly accessible window perpendicular to the incident beam contributes in each case only about 10% of the damage. Moreover, about twice as many defects in the $(11\bar{2}0)$ sample as in the other one recover below 32 K, i.e., including the first part of substage I_C. One is thus tempted to attribute this earlier temperature range to the annealing of defects produced close to the L_1 window (mainly into the directions $\langle 20\bar{2}2\rangle$ and $\langle 11\bar{2}0\rangle$), and the later part of Stage I, above 32 K, to the annealing of defects stemming from displacements close to the L_2-window (mainly along $\langle 20\bar{2}3\rangle$ and $\langle 0001\rangle$). The rather poor quantitative agreement is probably caused by the overlapping of both displacement mechanisms due to the mutual proximity of the L_1 and L_2 windows and the relatively high recoil energy, enabling the $\cos^2$ effect to take place. (Remember also the symmetry of the knock-on atom passage through both windows: $L_1-L_2-L_1$ etc. and $L_2-L_1-L_2$ etc.)[3]

b. Zinc

As we saw in Sec. IV.A.3.*b*, in zinc the thresholds for displacement into the directions $\langle 0001\rangle$ and $\langle 20\bar{2}2\rangle$—through the triangular windows L_3 and L_4—are lower than those through the rectangular windows L_1 and L_2; still lower is the threshold for displacement into the closest-packed direction $\langle 11\bar{2}0\rangle$. This was explained by the anomalously large c/a ratio in zinc favoring the stability of closer $\langle 0001\rangle$ and $\langle 11\bar{2}0\rangle$ pairs than would be the case for the ideal hcp cobalt. It is interesting to see how this might affect the recovery spectrum. The results for the three orientations used and a simultaneously irradiated polycrystal are presented in Table VII. The main observation—apart from the maximum total Stage I recovery for the (0001) crystal—is the reciprocal behavior of the substages I_C and I_D: I_C is largest and I_D smallest for the (0001) orientation, $(30\bar{3}4)$ exhibits the inverse dependence, at least for the lower energies. In general, $(11\bar{2}0)$ is rather close to $(30\bar{3}4)$ in percentage annealed, and the polycrystal is intermediaiate. Though no computed cross sections are available for a quantitative comparison analogous to that of cobalt, the I_C substage is tentatively proposed for the annealing of $\langle 0001\rangle$ oriented Frenkel pairs, while the I_D substage could be due to the recovery of defects in longer range collisions along $\langle 11\bar{2}0\rangle$ and through the close-lying windows L_4 and L_1. We note also that, for all orientations, the I_{C+D} annealing decreases to the benefit of substage I_A caused by an apparently more "difficult" pair, when one increases the electron energy. (One has, however, to be very cautious when discussing annealing stages that are close to the irradiation temperature.)

Furthermore, Ehrhart (1975) has observed in diffuse x-ray scattering measurements a strain field of the defect strongly oriented along the c axis. This would imply a split interstitial configuration along $\langle 0001\rangle$.

c. Cadmium

In view of the great experimental difficulties caused by the very low annealing temperatures in cadmium (cf. Sec. IV.A.3.*c*), the recovery data are rather scarce and not always reproducible. To give an idea of the observed anisotropy, Table VIII presents the annealing percentages obtained by Maury *et al.* (1973a) in the two

---

[3] In a recent study of the magnetic after-effect spectrum in cobalt crystals after 3-MeV irradiation at 4.2 K [(K. E. Schaeffer and W. Dander, 1976) established that at least six different Frenkel-pair configurations were responsible for the observed phenomena during Stage I, among which are the dumbells $\langle 1\bar{1}00\rangle$, $\langle 11\bar{2}0\rangle$, $\langle 2\bar{2}01\rangle$, $\langle 2\bar{2}02\rangle$, and $\langle 2\bar{2}03\rangle$.

TABLE VII. Stage I resistivity recovery of zinc crystals irradiated with various electron energies, in % (Maury *et al.*, 1973a).

Substage / T/K / Sample	0.5 MeV					0.6 MeV					0.9 MeV				
	I_A	I_B	I_C	I_D	I_E	I_A	I_B	I_C	I_D	I_E	I_A	I_B	I_C	I_D	I_E
	6	8	11	14	20	6	8	11	14	20	6	8	11	14	20
(0001)	1	0.5	46	50	2.5	0	0	40.5	53.5	4	10.5	1.5	34.5	35	5.5
$(11\bar{2}0)$	0	0.5	29	57.5	5	1	1	29	55	8	11	1	27.5	44.5	7.5
$(30\bar{3}4)$	1	0.5	27.5	61	···	0	0	29	56.5	···	10.5	0	31.5	43	···
Poly	1	0.5	36.5	55	···	0	1	36	53	4	11	2	33.5	42.5	6

main recovery regions above 4.2 K, for three different energies. One remarks two main features: (1) At lower energies, there is very little or no recovery above 6 K, while at 1.7 MeV the situation is reversed—the substage at 6–9 K is larger than that at 4–6 K. (2) At lower energies, the $(30\bar{3}8)$ crystal exhibits a smaller recovery stage at 4–6 K and a larger one at 6–9 K than the other orientations; at higher energy, both substages are more pronounced for this crystal. It does not seem possible to make a particular assignment to the observed substages, since, at low energies, the two crystallographic extremes, (0001) and $(11\bar{2}0)$, recover the same percentage of damage. This can only be understood through the fact that the specific Frenkel pairs giving rise to recovery anisotropy anneal at temperatures below that of the irradiation and, thus, did not show up in this study.

Coltman *et al.* (1971) observed recovery anisotropy in isotropically (neutron-) bombarded monocrystalline specimens at 3.6 K, when the angle between the direction of the measuring current and the *c* axis was varied. This anisotropy could possibly give an indication as to a specific configuration of the created interstitial, but the results were not really conclusive.

V. DERIVATION OF INTERATOMIC POTENTIALS FROM DISPLACEMENT-THRESHOLD DETERMINATIONS

It is quite obvious—and was recognized rather early—that knowledge of the threshold energies for atomic displacements into specific crystallographic directions could give us information about the interatomic potential in the interaction-energy range 1 to 10^3 eV. Indeed, the computed minimum energy which has to be imparted to an atom in a head-on collision when passing it through a certain lens (or several of them) to provoke the formation of a Frenkel pair will correspond to the respective T_d, provided the interatomic potential had been chosen correctly. Lucasson and Lucasson (1963) were the first to make an evaluation of this type. They used the effective threshold energies determined for a series of polycrystalline fcc metals (Cu, Ag, Au, Ni) and the computer results of Gibson *et al.* (1960), who had found that $T_d^{\langle 110\rangle} \approx T_d^{\langle 100\rangle}$ in copper, to deduce the correction factor α for the screening radius a_B in Bohr's screened Coulomb potential

$$V(r) = (Z^2e^2/r)\exp(-r/\alpha a_B)\,. \tag{5.1}$$

They noted that the uncertainties in α were remarkably small, even for big variations in T_d.

TABLE VIII. Resistivity recovery of cadmium crystals irradiated with various electron energies, in % (Maury *et al.*, 1973a).

E/MeV	T/K	Orientation (0001)	$(30\bar{3}8)$	$(11\bar{2}0)$
0.7	4–6	100	55–65	90
	6–9	1	10	0
0.9	4–6	80–100	70–85	80–100
	6–9	5–10	5–10	7–10
1.7	4–6	30	40	27
	6–9	35	47	43

Andersen and Sigmund (1965) went further in this direction, employing a Born–Mayer potential of the form (1.16) and using the single-crystal results of Sosin and Garr (1965) which had become available in the meantime, in addition to the computer findings by Gibson *et al.* (1960) on copper and by Erginsoy *et al.* (1964) on iron. Applying various scaling procedures, they concluded that the steepness of the potential, i.e., the parameter b in (1.16), was about the same for all metals, and proposed a Z-dependent universal Born–Mayer potential

$$V(r) = A_0Z^{3/2}\exp(-br)\,, \tag{5.2}$$

with $A_0 = 52$ eV and $b = 4.56$ Å^{-1}. Using this potential, they predicted $T_d^{\langle ijk\rangle}$ for the main displacement directions in a series of fcc and bcc metals, with varying success, as comparison with subsequently obtained experimental data has shown. (In most cases, the calculated values for the $T_d^{\min}$ are too small.)

Substantial progress in this field has been made by the Orsay group, who applied the threshold energies obtained from their single-crystal experiments to deduce interatomic potentials. Actually, they employed the inverse procedure, namely, they derived expressions for the T_d's where the potential showed up as an adjustable parameter. In the following, the procedure will be described in some detail; a Born–Mayer potential of the form (1.16) has been used.

For each lens passage (Fig. 53), two cases are to be distinguished: (1) when the moving atom loses its total kinetic energy and becomes interstitial immediately after passage through the lens, and (2) when the knock-

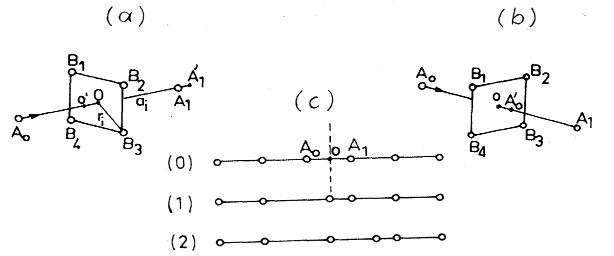

FIG. 53. (a) Last sequence and (b) penultimate sequence of a passage across a lens; (c) focusing collision sequence (Maury *et al.*, 1973b).

on atom has retained enough energy to push the atom in front out of its lattice site and replace it. In case (1), also called the "last sequence" [Fig. 53(a)], the energy T_d' dissipated during the passage across a lens consists of three terms

$$T_d' = V_1 + V_2 + E_{\text{kin}}' . \qquad (5.3)$$

Here V_1 is the energy needed to arrive at the saddle point 0 of Fig. 53(a), which is the center of a lens consisting of n atoms $B_1, \ldots, B_n$, so that

$$V_1 = n\, V(\overline{OB_i}) = n\, V(r_i) , \qquad (5.3\text{a})$$

where $V(r_i)$ is the energy of a pair of atoms at a distance r_i. V_2 is the interaction energy with the knocked-on atom A_1, so that $V_2 = V(a_i)$, where a_i is corrected by Lehmann and Leibfried's (1961) Δ [cf. Eq. (1.17)] since the interatomic shock is not a hard-core collision:

$$V_2 = V(\overline{O'A_1'}) . \qquad (5.3\text{b})$$

Moreover, the atom A_0 transmits kinetic energy to the atoms B_i and to A_1 in the direction of its motion

$$E_{\text{kin}}' \approx (V_1 + V_2)/(n+2) , \qquad (5.3\text{c})$$

the mass ratio being $1/(n+2)$. In the "penultimate sequence" of case (2), Fig. 53(b), the atom A_0 has to transmit to the atom A_1 at least the energy calculated for case (1), T_d'. An atom possessing such an energy can be described by a hard-core radius r_{hc}, through $V(r_{\text{hc}}) = \frac{1}{2} T_d'$, since only half of the available kinetic energy is transformed in potential energy for equal masses. Again, due to the correction term Δ, the actual position of A_0 during the collision will be $(\overline{OA_0'}) = a_i - \Delta - r_{\text{hc}}$, hence

$$V_3 = n\, V(\overline{A_0'B_i}) . \qquad (5.4\text{a})$$

A further corrective term is the kinetic energy communicated to B_i perpendicular to the direction of motion of A_0

$$E_{\text{kin}}'' = n b^2 (\overline{OA_0'})^2 V^2(r_i)/(T_d' + V_3) . \qquad (5.4\text{b})$$

Here use was made of the fact that, for an exponential form of the potential, $V = A\exp(-br)$, the derived force is $f = -dV/dr = b\,V(r)$. After subtraction of the zero-point energy, which is the interaction of a lattice atom with its m neighbors (at a distance a) and is liberated by the formation of a vacancy during the first collision (neglecting the contraction around it), $E_0 = m\,V(a)$, one obtains finally

$$T_d'' = V_3 + E_{\text{kin}}'' - E_0 , \qquad (5.4)$$

and

$$T_d = T_d' + T_d'' . \qquad (5.5)$$

A special case is the propagation of a focused collision chain [Fig. 53(c)]. Here, the atom A_0 has to traverse the saddle point 0; this "compression wave" continues to proceed without losing energy, except to the surrounding atoms B_i. The compression energy can be expressed as

$$E_{\text{comp}} = 2V\left(\frac{a}{2} + \Delta\right) - E_0 , \qquad (5.6\text{a})$$

and the energy lost to the n lens atoms B_i, $V_{1,n} = n\,V(r_i)$, or after l collisions

$$V_1 = l\,V_{1,n} . \qquad (5.6\text{b})$$

Thus the total energy spent in a focusing chain is

$$T_d^f = E_{\text{comp}} + V_1 . \qquad (5.6)$$

Numerical results have been obtained for several metals and are presented in the following.

A. Alpha-iron

The principal displacement thresholds deduced in Sec. IV.A.2.*c* by Maury *et al.* (1976) were $T_d^{\langle 100\rangle} = 17$ eV, $T_d^{\langle 110\rangle} = 30$–$35$ eV, and $T_d^{\langle 111\rangle} = 20$ eV. In order to arrive at these values using the expressions (5.3) to (5.6) one has to assume a specific number of passages into each direction. Calculations were made for two and for three $\langle 100\rangle$ passages. Computing the number n of replacement collisions in the $\langle 111\rangle$ direction needed to yield $T_d^{\langle 111\rangle}$

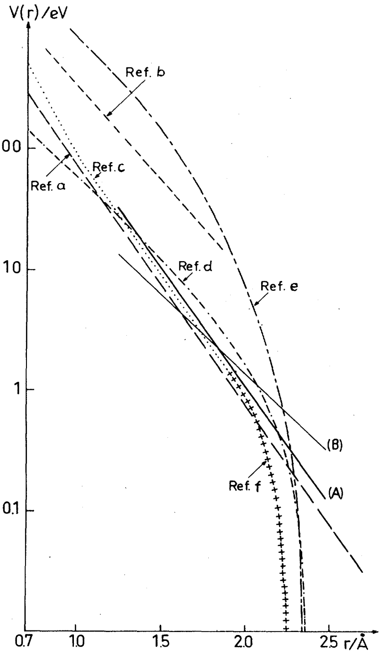

FIG.54 Various interatomic potentials for α-iron. (*A*) and (*B*) are the potentials delimiting the possible choice according to Maury *et al.* (1976); (*A*) is the preferred potential. References (a) Erginsoy *et al.*, 1964; (b) Andersen and Sigmund, 1965; (c) Girifalco and Weizer, 1959; (d) Johnson, 1964; (e) Bullough and Perrin, 1969; (f) Abrahamson, 1969 (Maury *et al.*, 1976).

$=20$ eV, one gets a maximum value of $n=6$ in the case of two $\langle 100\rangle$ passages. This leads to an instability region around the vacancy of roughly 60 at. vol., too small a value for the recombination volume in iron (cf. Biget, Rizk *et al.*, 1975). This leaves us with three $\langle 100\rangle$ passages and a corresponding n varying between five and nine $\langle 111\rangle$ collisions. The two extremes were obtained using Born–Mayer potentials $V/\mathrm{ev}=570\exp(-3r/\text{Å})$ and $8900\exp(-4.5r/\text{Å})$. Both potentials are presented in Fig. 54 together with various iron potentials used in the literature. The steeper potential (curve A) comes rather close to Erginsoy's choice (1964), obtained by fitting the elastic constants of iron, to the empirical potential by Andersen and Sigmund (1965), and, in the interesting range 1 to 10 eV, to Johnson's potential (1964). Thus, a preference is accorded to

$$V^{\mathrm{Fe}}(r/\text{Å})/\mathrm{eV}=8900\exp(-4.5r)\,.$$

B. Molybdenum

The matching procedure of Sec. IV.A.2.*d*. gave a best fit to the experiment using $T_d^{\langle 100\rangle}=35$ eV, $T_d^{\langle 111\rangle}=45$ eV, and $T_d^{\langle 110\rangle}>2T_d^{\langle 100\rangle}$. The application of formulae (5.3) to (5.6) is straightforward, and we present in Table VIII the T_d's in the three directions calculated for a varying number of lens passages with several sets of potential constants. [The constants A and b in Eq. (1.16) cannot be determined independently, as there is an exponential relation between them.) The left half of Table IX gives the results obtained when $T_d^{\langle 100\rangle}=35$ eV after two passages through (100) windows, while the right half represents the calculations giving $T_d^{\langle 100\rangle}=35$ eV after three passages. As one can see, there is still quite a choice left as to the number of $\langle 111\rangle$ passages to yield $T_d^{\langle 111\rangle}=45$ eV, so we have to look for additional information. This is available in the form of the spontaneous recombination volume of a Frenkel pair, α_r, which is an indication of the elastic forces acting around point defects. Now, α_r has been determined for a series of metals, in particular for molybdenum (Vajda and Biget, 1974) in which $\alpha_r^{\mathrm{Mo}}=200$ to 250 atomic volumes. For two (100) passages, α_r is always too small. On the other hand, for three (100) passages one obtains a reasonable agreement with a spontaneous recombination volume of the form depicted in Fig. 55, i.e., with six to seven (111) passages. The potential giving these results can be found in the range

$$3000\exp(-3.2r)\leqslant V^{\mathrm{Mo}}(r/\text{Å})/\mathrm{eV}\leqslant 11.000\exp(-3.8r)\,.$$

Fig. 56 shows the above potential together with several others deduced by various means: (a) Andersen and Sigmund's empirical Born–Mayer potential (1965); (b) Varshni and Bloore's Rydberg-type potential (1963); (c) Kenny and Heald's cubic polynomial (1974) obtained by matching to the elastic constants and to the vacancy formation energy of molybdenum for $r\geqslant 1.8$ Å, while fitting to Abrahamson's Thomas–Fermi–Dirac potential (1969) for smaller distances.

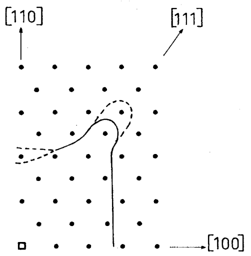

FIG. 55. View of a (110) plane in molybdenum indicating the region of spontaneous recombination around the vacancy in the lower left corner of the figure (Maury *et al.*, 1975).

C. Tantalum

The conditions $T_d^{\langle 100\rangle}=33$eV, $T_d^{\langle 111\rangle}\gtrsim 55$ eV (cf., Sec. IV.A.2.*e*.) and the size of the spontaneous recombination volume under irradiation given by Biget, Rizk *et al.* (1975) as $\alpha_r\gtrsim 200$ atomic volumes lead to three lens passages in the $\langle 100\rangle$ direction and to seven passages in the $\langle 111\rangle$ direction. The interatomic potential with which one obtains the above values can be found in the range $(A,b)=(21\,500$ eV, -4.0 Å$^{-1})$ to $(175\,000$ eV, -5.0 Å$^{-1})$, with the best choice

$$V^{\mathrm{Ta}}(r/\text{Å})/\mathrm{eV}=61\,000\exp(-4.5r)\,.$$

This potential is compared in Fig. 57 to the one proposed by Andersen and Sigmund, 1965, $V_{AS}/\mathrm{eV}=32\,400\exp(-4.56r)$, and to that deduced from recent work by Wilson, *et al.* (1977) giving a universal average potential for the calculation of ranges of low-energy projectiles ($\gtrsim 1$ eV), V_{WHB}.

The fact that the ratio $T_d^{\langle 111\rangle}/T_d^{\langle 100\rangle}$ is higher in Ta, $\gtrsim 55/33$, than in Mo, 45/35, with a comparable size of the spontaneous recombination volume, leads to a steeper

TABLE IX. Threshold energies for displacement in different directions in molybdenum, calculated for a varying number of lens passages, in eV (Maury *et al.*, 1975).

$b/\text{Å}^{-1}$ A/eV	2.0 330	2.5 940	3.0 2700	3.5 7500	4.0 20 800	2.0 235	2.5 690	3.0 2000	3.5 5800	4.0 16 200
Passage										
2 × (100)	35.6	35.0	35.2	34.8	35.0	25.4	25.7	26.1	26.9	27.3
3 × (100)	49.4	47.7	47.1	45.5	44.7	35.2	35.0	34.9	35.2	34.8
1 × (110)	44.6	54.2	67.4	82.0	100.7	31.7	39.8	49.9	63.4	78.4
2 × (110)	80.2	96.6	118.8	142.6	172.1	57.1	70.9	88.0	110.2	134.0
1 × (111)	17.1	20.7	26.8	35.2	47.5	12.2	15.2	19.9	27.2	37.0
3 × (111)	29.7	30.8	35.0	41.6	52.4	21.1	22.6	25.9	32.2	40.8
5 × (111)	42.2	40.9	43.2	48.0	57.4	30.1	30.0	32.0	37.1	44.7
7 × (111)	54.8	51.0	51.4	54.4	62.4	39.0	37.4	38.0	42.0	48.6
9 × (111)	67.4	61.1	59.6	60.8	67.4	48.0	44.8	44.1	46.9	52.5

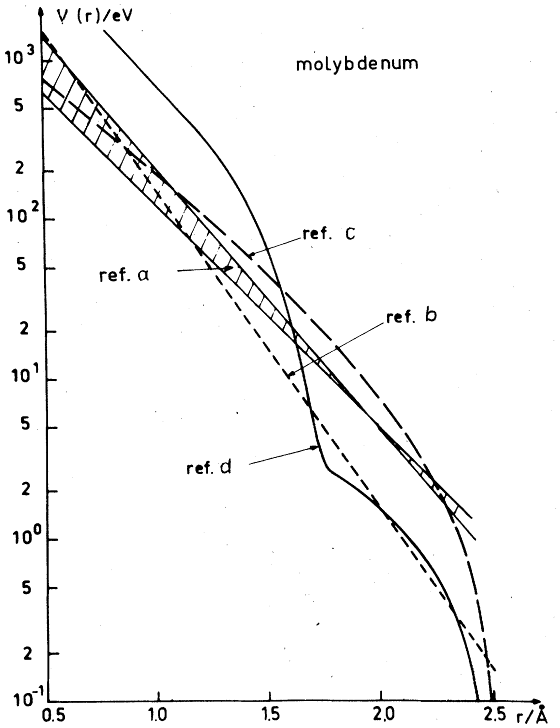

FIG. 56. Various interatomic potentials for molybdenum. References: (a) region of possible choice according to Maury *et al.*, 1975; (b) Andersen and Sigmund, 1965; (c) Varshni and Bloore, 1963; (d) Kenny and Heald, 1974 (Maury *et al.*, 1975).

interatomic potential [in order to increase the energy needed to build up the "compressed configuration" along ⟨111⟩ cf. Eq. (5.6a)].

D. Cobalt

The close values obtained for the threshold energies in the ⟨20$\bar{2}$2⟩ and ⟨20$\bar{2}$3⟩ directions (cf. Sec. IV.A.3.*a*.) imply a collision sequence through the two rectangular lenses L_1 and L_2 of three to four passages. Table X gives the thresholds for displacement in the investigated directions for three pairs of potential constants. Stability arguments for the close pairs in the ⟨0001⟩ and ⟨20$\bar{2}$1⟩ directions led to a best choice of

$$V^{\mathrm{Co}}(r/\text{Å})/\text{eV} = 3300\exp(-4.1r)\,.$$

This potential is plotted together with other ones from the literature in Fig. 58. [The potential of Lucasson

TABLE X. Threshold energies for displacement in different directions in cobalt calculated for different lens combinations and various pairs of BM constants, in eV (Maury *et al.*, 1973b).

⟨*hkil*⟩	T_d^{expt}	Passage	A/eV	8000	2800	1400
			b/Å^{-1}	4.6	4.0	3.6
⟨0001⟩	40	L_3		39.1	31.8	27.6
		L_3-L_3		68.2	55.8	48.9
⟨20$\bar{2}$3⟩	23	$L_2-L_1-L_2$		24.5	21.3	19.8
		$L_2-L_1-L_2-L_1$		23.4	23.7	24.1
⟨20$\bar{2}$2⟩	22	$L_1-L_2-L_1$		22.1	22.1	22.1
⟨20$\bar{2}$1⟩	40	L_4		39.4	32.0	27.8
		L_4-L_1		45.0	38.1	34.4
⟨11$\bar{2}$0⟩	27	9 Collisions		26.0	26.0	27.1
		10 Collisions		27.6	28.0	29.5

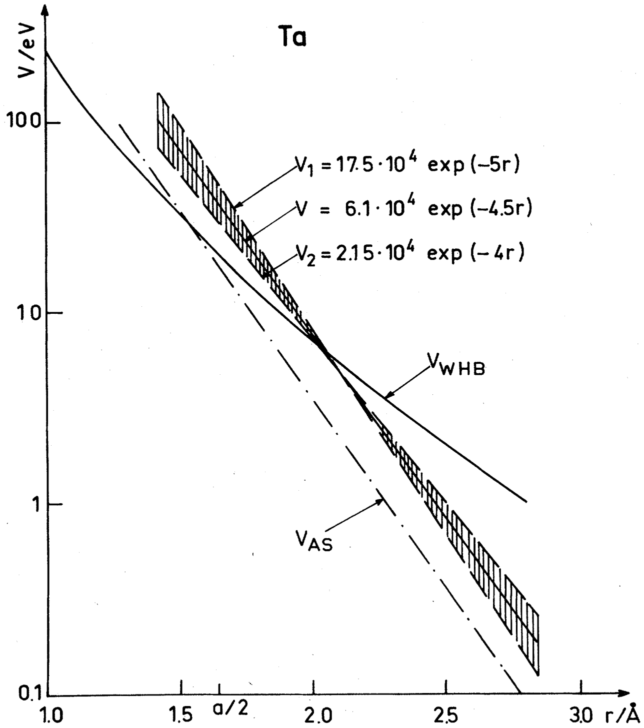

FIG. 57. Various interatomic potentials for tantalum. References: shaded area, region of possible choice according to Biget *et al.* 1977a; V_{AS}, Andersen and Sigmund 1965; V_{WHB}, Wilson, W. D., L. G. Haggmark and J. P. Biersack 1977, Phys. Rev. B 15, 2458.

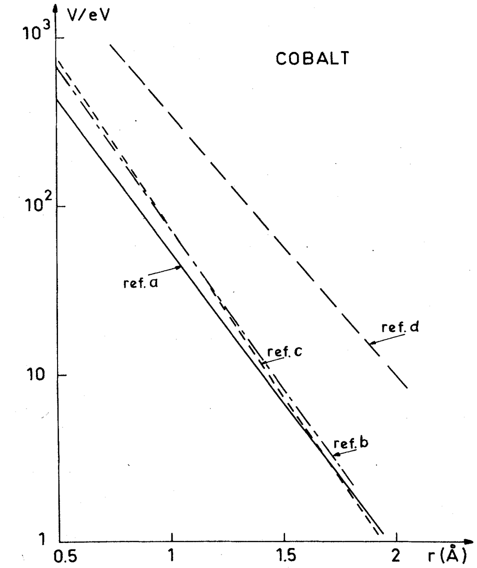

FIG. 58. Various interatomic potentials for cobalt. References: (a) Maury *et al.*, 1973b; (b) Lucasson and Lucasson, 1963; (c) Andersen and Sigmund, 1965; (d) Abrahamson, 1969.

(1963) was obtained by matching a Born–Mayer form to their Bohr potential so as to yield T_d in one of the easy displacement directions.] The overall agreement is very close; only Abrahamson's TFD potential fit (1969) is too high.

E. Zinc

The relatively low $T_d^{\langle 0001\rangle}$ for zinc (cf. Sec. IV.A.3.*b*.) implies just one passage through a (0001) window to produce a stable Frenkel pair. When taking this into consideration, Table XI gives the calculated thresholds for three combinations (A, b). One sees that softening the potential by decreasing b favors passage through triangular lenses L_3 and L_4 over passage through rectangular ones, L_1 and L_2. Assuming the same stability in zinc as in cobalt (three passages in the $\langle 20\bar{2}3\rangle$ direction) would imply a $b = 2.0$ Å^{-1}, while lesser stability in zinc, i.e., five passages across L_1 and L_2, would tend towards $b = 2.5$ Å^{-1}. The potential range thus covered is

$$280 \exp(-2.5r) < V^{\mathrm{Zn}}(r/\text{Å})/\mathrm{eV} < 155 \exp(-2r)\,.$$

This range is represented in Fig. 59. For comparison, I have added the composite potential derived by Benedek (1975) by interpolation between a Thomas–Fermi term at higher energies and a screened Coulomb + core-overlap (Born-Mayer) contribution at low energies; this and the other theoretical or empirical potentials are all steeper and, in the interesting range above T_d, also much higher.

Finally, as was pointed out by Maury *et al.* (1973b), one has to view the results derived by means of a Born–Mayer potential with some caution, since the use of a spherically symmetric potential for highly anisotropic crystals such as zinc (and also cadmium) remains to be justified.

F. Cadmium

After making the same reservations concerning the choice of the potential form as in the case of zinc and recalling the fact that the computed cross sections (Sec. IV.A.3.*c*.) were not very sensitive to the values of T_1, T_2, and T_3 as long as the latter were large enough, we give in Table XII the thresholds calculated with the potential

$$V^{\mathrm{Cd}}(r/\text{Å})/\mathrm{eV} = 300 \exp(-2r)\,.$$

The potentials of Lucasson 1963, Andersen and Sigmund 1965, and Abrahamson 1969 are as far off for cadmium as they were for zinc.

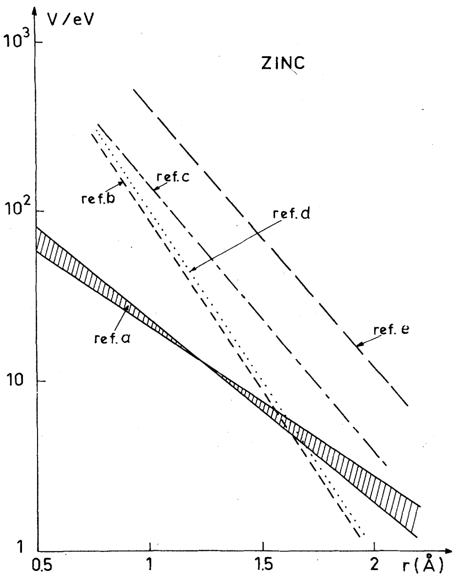

FIG. 59. Various interatomic potentials for zinc. References: (a) region of possible choice according to Maury *et al.*, 1973b; (b) Andersen and Sigmund, 1965; (c) Lucasson and Lucasson, 1963; (d) Benedek, 1975; (e) Abrahamson, 1969.

TABLE XI. Threshold energies for displacement in different directions in zinc, calculated for different lens combinations and various pairs of BM constants, in eV (Maury *et al.*, 1973b).

$\langle hkil\rangle$	T_d^{expt}	Passage	A/eV	550	280	155
			b/Å^{-1}	3.0	2.5	2.0
$\langle 0001\rangle$	19	L_3		18.6	18.5	18.5
$\langle 20\bar{2}3\rangle$	25	$L_2-L_1-L_2-L_1$		14.9	20.0	29.0
		$L_2-L_1-L_2-L_1-L_2$		18.7	24.4	35.1
$\langle 20\bar{2}2\rangle$	30	$L_1-L_2-L_1$		13.3	17.2	23.8
		$L_1-L_2-L_1-L_2$		17.0	21.5	29.7
		$L_1-L_2-L_1-L_2-L_1$		21.1	28.3	41.3
$\langle 20\bar{2}1\rangle$	20	L_4		13.9	14.2	14.3
		L_4-L_1		18.4	20.9	25.1
$\langle 11\bar{2}0\rangle$	14	4 Collisions		9.4	11.6	16.5
		5 Collisions		11.0	14.3	21.6

VI. CONCLUSIONS

As a kind of summary, I recapitulate in Tables XIIIa to c the data concerning threshold energies for displacement. Care has been taken to use only results which, at this stage, seemed reliable—both with respect to the kind of experiment employed and to the corresponding analysis. Thus, I have only included "true" threshold energies, not taking into account observed apparent thresholds in various directions, which had not been treated in an adequate model. Some of the data given in parentheses are to be viewed with caution. For completeness, the displacement thresholds determined in polycrystalline metals have been added. The last column gives, when available, the reasonably well estab-

TABLE XII. Threshold energies for displacement in different directions in cadmium, calculated with the potential $V/\mathrm{eV} = 300 \exp(-2r/\text{Å})$, in eV (Maury *et al.*, 1973b).

$\langle hkil\rangle$	T_d^{expt}	Passage	T_d^{calc}
$\langle 0001\rangle$	$\gtrsim 40$	L_3-L_3	52
$\langle 20\bar{2}3\rangle$	$\gtrsim 35$	$L_2-L_1-L_2-L_1$	34
$\langle 20\bar{2}2\rangle$	$\gtrsim 35$	$L_1-L_2-L_1-L_2$	36
$\langle 20\bar{2}1\rangle$	19	L_4	20
$\langle 11\bar{2}0\rangle$	21	4 Collisions	20
		5 Collisions	25

lished values for the fundamental quantity ρ_F, whose knowledge is, among others, essential for the deduction of the spontaneous recombination volume of Frenkel pairs, α_r, from saturation-resistivity measurements (Biget, Rizk *et al.*, 1975). The spontaneous recombination volumes, on the other hand, can give valuable information—as we have seen in Sec. V—on the number of passages in certain directions made by a recoil atom before resulting in a stable interstitial. In a kind of feedback, the interatomic potential, the derivation of which has been favored by this information, permits us to establish the shape of α_r, itself a very interesting characteristic.

TABLE XIII. True threshold energies for displacement and Frenkel-pair resistivities in (a) fcc, (b) bcc, and (c) hcp metals, in eV and $10^{-4}\Omega$ cm/F.P.

(a) fcc metals

Metal	$T_d^{\langle 100\rangle}$	$T_d^{\langle 110\rangle}$	$T_d^{\langle 111\rangle}$	T_d^{Poly}	ρ_F
Al				16[a]	3.9
β-Co		23			
Ni	(38)	21	(>60)	24[b]	
Cu	20	19	45	19[c]	1.7
Pd				34[d]	
Ag		(23)		26[e]	
Pt	36	38	75	37[f]	9.5
Au	36–40	36–40		40[g]	3.2
Pb				12[h]	
Th				35[i]	

(b) bcc metals

Metal	$T_d^{\langle 100\rangle}$	$T_d^{\langle 110\rangle}$	$T_d^{\langle 111\rangle}$	T_d^{Poly}	ρ_F
V	(30)			26[j]	
Cr	(28)			28[k]	
α-Fe	17	30–35	20	22[l]	30
Nb				28[m]	
Mo	35	$\gtrsim$70	>45	35[n]	13
β-Sn[r]				22[o]	
Ta	33	>55	$\gtrsim$55	32[p]	16
W				50.5[q]	

(c) hcp metals

Metal	$T_d^{\langle 0001\rangle}$	$T_d^{\langle 20\bar{2}3\rangle}$	$T_d^{\langle 20\bar{2}2\rangle}$	$T_d^{\langle 20\bar{2}1\rangle}$	$T_d^{\langle 11\bar{2}0\rangle}$	T_d^{Poly}	ρ_F
Mg						10[s]	
Ti						19[t]	
α-Co	40	23	22	40	27	22.5[u]	15
Zn	19	25	30	20	14	13.5[v]	15
Ga[bb]						12[w]	
Zr						21[x]	
Cd	$\gtrsim$40	$\gtrsim$35	$\gtrsim$35	19	21	19[y]	
Lu						17[z]	
Re						$\gtrsim$40[aa]	

[a] Neely and Bauer, 1966.
[b] Lucasson and Walker, 1962.
[c] Lucasson, Lucasson, and Walker, 1961.
[d] Jimenez *et al.*, 1967.
[e] Rizk *et al.*, 1977.
[f] Jung *et al.*, 1973.
[g] Hancock, 1974.
[h] Birtcher and Koehler, 1976.
[i] Guinan, Snead, and Goland, 1973.
[j] Miller and Chaplin, 1974.
[k] Biget and Vajda, 1975.
[l] Lucasson, Lucasson, and Walker, 1961.
[m] Jung and Lucki, 1975.
[n] Rizk *et al.*, 1973.
[o] McIlwain *et al.*, 1975.
[p] Youngblood, Myhra, and de Ford, 1969.
[q] Vajda *et al.*, 1977.
[r] bc tetragonal.
[s] O'Neal and Chaplin, 1972.
[t] Shirley and Chaplin, 1972.
[u] Maury, Lucasson, and Lucasson, 1974.
[v] Maury, Lucasson, and Lucasson, 1971.
[w] Myhra and Gardiner, 1975.
[x] Biget *et al.*, 1971.
[y] Maury, Lucasson, and Lucasson, 1969.
[z] Daou *et al.*, 1977.
[aa] Vandenborre *et al.*, 1974.
[bb] Pseudohexagonal.

The importance of the Frenkel-pair resistivity quite early incited the search for a correspondence between ρ_F and other specific properties of a metal. Thus, Lucasson and Walker (1962) proposed the relationship $\rho_F \approx 100\rho_{0\,^\circ\mathrm{C}}$ (within a factor of 2), which they derived from a step-function analysis of electron damage rate data in polycrystals. Another empirical rule was suggested by Wenzl (1970), who preferred the Debye temperature θ as characteristic reference: $\rho_F \approx 100\rho_\theta$. The latest proposal stems from Benedek (1973), who has found a correlation between the electric resistivity of vacancies as determined from quenching experiments and the lattice resistivity at the melting point; after discussing the origin of this behavior in the framework of pseudopotential theory he suggests: $\rho_F \approx 15\rho(T_m)$. Though the two latter relationships are more satisfactory than the first one from a physical point of view, since no special meaning is attributable to a temperature of 0 °C, their success is no greater. Wenzl's rule often predicts too small a ρ_F, while Benedek's rule does not work for the low-melting point metals. The only observations we can make from Tables XIII are:

(a) for fcc metals $\rho_F \approx (100\text{–}150)\rho_{0\,^\circ\mathrm{C}}$;

(b) for bcc metals $\rho_F \approx (150\text{–}300)\rho_{0\,^\circ\mathrm{C}}$;

(c) for hcp metals $\rho_F \approx (250\text{–}300)\rho_{0\,^\circ\mathrm{C}}$.

Any generalization seems premature. From the above discussion, we can see a special need for future irradiation experiments with single crystals which include determinations of ρ_F employing electrical resistivity and/or diffuse x-ray measurements. It would also be useful if, in the analysis of the damage production and recovery data, interatomic potentials were deduced using models for Frenkel-pair formation, and recovery substages were assigned by juxtaposition of displacement cross sections and annealing percentages, and by calculating configurational energies.

ACKNOWLEDGMENTS

I wish to thank all the authors who gave their permission to use the material presented here, as well as the publishers of the journals concerned. Special thanks are extended to Drs. J. N. Lomer, P. Jung, P. Ehrhart, and F. Dausinger for making available unpublished data. The results of the work at Orsay were obtained in close collaboration with F. Maury, M. Biget, A. and P. Lucasson, to all of whom I am much indebted.

REFERENCES

Abrahamson, A. A., 1969, Phys. Rev. **178**, 76.

Agranovitch, V. M., and V. V. Kirsanov, 1970, Fiz. Tverd. Tela **12**, 2671 [Sov. Phys.—Solid State **12**, 2147 (1971)].

Agranovitch, V. M., and V. V. Kirsanov, 1976, Uspeki-Fiz. Nauk. **118**, 3 [Sov. Phys. Uspeki **19** (1977)].

Akita, H., and N. F. Fiore, 1973, J. Appl. Phys. **44**, 20.

Andersen, H. H., and P. Sigmund, 1965, Risø-Report No. 103 (Danish AEC).

Balarin, M., 1962, Phys. Status Solidi **2**, 60.

Baranov, A. I., V. I. Panov, L. S. Smirnov, and S. A. Sokolov, 1972, Fiz. Tekh. Poluprovodn. **6**, 2276 [Sov. Phys.—Semicond. **6**, 1920 (1973)].

Bauer, W., A. I. Anderman, and A. Sosin, 1969, Phys. Rev. **185**, 870.

Bauer, W., and A. Sosin, 1964, J. Appl. Phys. **35**, 703.

Bauer, W., and A. Sosin, 1966, J. Appl. Phys. **37**, 1780.

Benedek, R., 1973, Rep. No. 2029, Materials Science Center, Cornell Univ. and private communication.

Benedek, R., 1975, paper presented at the International Conference on the Fundamental Aspects of Radiation Damage in Metals, Gatlinburg, Tenn., USERDA Conf.–751006–Pl, p. 207.

Bethe, H., and W. Heitler, 1934, Proc. R. Soc. A **146**, 83.

Biget, M., F. Maury, P. Vajda, A. Lucasson, and P. Lucasson, 1971, Radiat. Eff. **7**, 223.

Biget, M., F. Maury, P. Vajda, A. Lucasson, and P. Lucasson, 1977a, Phys. Rev. unpublished.

Biget, M., F. Maury, P. Vajda, A. Lucasson, P. Lucasson, 1977b, unpublished.

Biget, M., R. Rizk, P. Vajda, and A. Bessis, 1975, Solid State Commun. **16**, 949.

Biget, M., P. Vajda, A. Lucasson, and P. Lucasson, 1974, Radiat. Eff. **21**, 229.

Biget, M., P. Vajda, F. Maury, A. Lucasson, and P. Lucasson, 1975, paper presented at the International Conference on the Fundamental Aspects of Radiation Damage in Metals, Gatlinburg, Tenn., USERDA Conf.–751006–Pl, p. 66.

Birtcher, R. C., and J. S. Koehler, 1976, Phys. Rev. B **13**, 2314.

Bourret, A., 1971, Phys. Status Solidi A **4**, 813.

Bullough, R., and R. C. Perrin, 1969, Radiation Damage in Reactor Mat. (IAEA, Vienna), Vol. II.

Chadderton, L. T., 1965, *Radiation Damage in Crystals* (Methuen, London).

Chadderton, L. T., and I. McC. Torrens, 1965, Nature **208**, 880.

Chaplin, R. L., 1974, Radiat. Eff. **22**, 117.

Coltman, R. R., C. E. Klabunde, J. K. Redman, and A. L. Southern, 1971, Radiat. Eff. **7**, 235.

Copé, R., 1969, CEA-R-3854, Saclay (France).

Corbett, J. W., 1966, *Electron Radiation Damage in Semiconductors and Metals* (Academic, New York).

Cusson, Y., P. Lucasson, and R. M. Walker, 1961, in *Proceedings of the International Conference on the Properties of Reactor Materials*, edited by D. J. Littler (Butterworths, London), p. 92.

Daou, J. N., J. E. Bonnet, P. Vajda, M. Biget, A. Lucasson, and P. Lucasson, 1977, Phys. Status Solidi A **40**, 101.

Dausinger, F., 1975, Ph.D. thesis, University of Stuttgart (Germany).

Dausinger, F., and H. Schultz, 1975, paper presented at the International Conference on the Fundamental Aspects of Radiation Damage in Metals, Gatlinburg, Tenn., USERDA Conf.–751006–Pl, p. 438.

Dausinger, F., and H. Schultz, 1975, Phys. Rev. Lett. **35**, 1773.

Dautreppe, D., 1969, "Radiation Effects in Magnetic Materials" in *Studies in Radiation Effects in Solids*, Vol. 3, edited by G. J. Dienes (Gordon and Breach, New York), p. 1.

Dearnaley, G., J. H. Freeman, R. S. Nelson, and J. Stephen, 1973, *Ion Implantation* (North-Holland, Amsterdam).

Dworschak, F., H. Schuster, H. Wollenberger, and J. Wurm, 1967, Phys. Status Solidi **21**, 741.

Dworschak, F., W. Sassin, J. Wick, and J. Wurm, 1969, Jül.–575–FN, KFA–Jülich (Germany).

Ehrhart, P., 1975, paper presented at the International Conference on the Fundamental Aspects of Radiation Damage in Metals, Gatlinburg, Tenn., USERDA Conf.–751006–Pl, p. 302.

Ehrhart, P., H. G. Haubold, and W. Schilling, 1974, Festkoerperprobleme (Adv. Solid State Phys.) ***XIV***, 87.

Ehrhart, P., and W. Schilling, 1973, Phys. Rev. B **8**, 2604.

Ehrhart, P., and U. Schlagheck, 1974, J. Phys. F. **4**, 1575.

Ehrhart, P., and E. Segura, 1975, paper presented at the International Conference on the Fundamental Aspects of Radiation Damage in Metals, Gatlinburg, Tenn., USERDA Conf.–751006–Pl, p. 295.

Erginsoy, C., G. H. Vineyard, and A. Englert, 1964, Phys. Rev. **133**, A595.

Forsch, K., 1970, Phys. Status Solidi **42**, 329.

Forsch, K., J. Hemmerich, H. Knöll, and G. Lucki, 1974, Phys. Status Solidi A **23**, 223.

Gettys, W. E., 1966, Phys. Rev. **146**, 480.

Gibson, J. B., A. N. Goland, M. Milgram, and G. H. Vineyard, 1960, Phys. Rev. **120**, 1229.

Girifalco, L. G., and W. G. Weizer, 1959, Phys. Rev. **114**, 687.

Granato, A., and K. Lücke, 1956, J. Appl. Phys. **27**, 583.

Guinan, M. W., C. L. Snead, and A. N. Goland, 1973, Radiat. Eff. **20**, 33.

Gwozdz, P. S., and J. S. Koehler, 1973, Phys. Rev. B **8**, 3616.

Hancock, J. S. N., 1974, Ph.D. thesis, University of Reading (England).

Hancock, J. S. N., and J. N. Lomer, 1975, private communication.

Hebbard, D. F., and P. R. Wilson, 1955, Aust. J. Phys. **8**, 90.

Howe, L. M., 1970, Phil. Mag. **22**, 965.

Jan, R. v., and A. Seeger, 1963, Phys. Status Solidi **3**, 465.

Jimenez, C. M., L. F. Lowe, E. A. Burke, and C. H. Sherman, 1967, Phys. Rev. **153**, 735.

Johnson, R. A., 1964, Phys. Rev. **134**, 1329A.

Jung, P., R. L. Chaplin, H. J. Fenzl, K. Reichelt, and P. Wombacher, 1973, Phys. Rev. B **8**, 553.

Jung, P., 1971, Kernforschungsalage Jülich Report Jül.–729–FF.

Jung, P., and G. Lucki, 1975, Radiat. Eff. **26**, 99.

Jung, P., and W. Schilling, 1972, Phys. Rev. B **5**, 2046.

Jung, P., and T. Schober, 1975, paper presented at the International Conference on the Fundamental Aspects of Radiation Damage in Metals, Gatlinburg, Tenn., USERDA Conf.–751006–Pl, p. 418.

Kamada, K., Y. Kazumata, and S. Suda, 1964, Phys. Status Solidi **7**, 231.

Kenik, E. A., and T. E. Mitchell, 1975, Phil. Mag. **32**, 815.

Kenny, P. N., and P. T. Heald, 1974, Phil. Mag. **29**, 1137.

Kinchin, G. H., and R. S. Pease, 1955, Rep. Prog. Phys. **18**, 1.

Landau, L., 1944, J. Phys. USSR **8**, 201.

Lehmann, C., and G. Leibfried, 1961, Z. Phys. **162**, 203.

Leibfried, G., 1959, J. Appl. Phys. **30**, 1388.

Lomer, J. N., and M. Pepper, 1967, Phil. Mag. **16**, 1119.

Longshore, R. E., and R. L. Chaplin, 1969, J. Appl. Phys. **40**, 351.

Lucasson, A., P. Lucasson, and R. M. Walker, 1961, in *Proceedings of the International Conference on the Properties of Reactor Materials*, edited by D. J. Littler (Butterworths, London), p. 83.

Lucasson, P., 1975, paper presented at the International Conference on the Fundamental Aspects of Radiation Damage in Metals, Gatlinburg, Tenn., USERDA Conf.–751006–Pl, p. 42.

Lucasson, P., and A. Lucasson, 1963, J. Phys. (Paris) **24**, 503.
Lucasson, P. G., and R. M. Walker, 1962, Phys. Rev. **127**, 1130.
Makin, M. J., 1970, in *Proceedings of the International Conference on Atomic Collision Phenomena in Solids, Sussex*, edited by D. W. Palmer *et al.* (North Holland, Amsterdam), p. 205.
Maury, F., M. Biget, P. Vajda, A. Lucasson, and P. Lucasson, 1976, Phys. Rev. B **14**, 5303.
Maury, F., A. Lucasson, and P. Lucasson, 1969, Radiat. Eff. **1**, 241.
Maury, F., A. Lucasson, and P. Lucasson, 1971, Cryst. Lattice Defects **2**, 47.
Maury, F., A. Lucasson, and P. Lucasson, 1974, Radiat. Eff. **21**, 65.
Maury, F., and P. Lucasson, 1976, Phys. Status Solidi A **34**, 513.
Maury, F., G. Roux, P. Vajda, C. Minier, A. Lucasson, and P. Lucasson, 1970, Cryst. Lattice Defects **1**, 361.
Maury, F., P. Vajda, M. Biget, A. Lucasson, and P. Lucasson, 1975, Radiat. Eff. **25**, 175.
Maury, F., P. Vajda, A. Lucasson, and P. Lucasson, 1973a, Phys. Rev. B **8**, 5496.
Maury, F., P. Vajda, A. Lucasson, and P. Lucasson, 1973b, Phys. Rev. B **8**, 5506.
Maury, F., P. Vajda, A. Lucasson, P. Lucasson, G. Roux, and C. Minier, 1970, Phil. Mag. **22**, 1265.
McIlwain, J., R. Gardiner, A. Sosin, and S. Myhra, 1975, Radiat. Eff. **24**, 19.
McKinley, W. A., and H. Feshbach, 1948, Phys. Rev. **74**, 1759.
Miller, M. G., and R. L. Chaplin, 1974, Radiat. Eff. **22**, 107.
Mitchell, T. E., G. Das, and E. A. Kenik, 1975, paper presented at the International Conference on the Fundamental Aspects of Radiation Damage in Metals, Gatlinburg, Tenn., USERDA Conf.–751006–Pl, p. 73.
Moser, P., J. Verdone, W. Chambron, V. Hivert, and R. Pichon, 1973, paper presented at the Fifth International Conference on Int. Friction and Ultrasonic Attenuation in Crystal Solids, Aachen (Germany).
Mott, N. F., 1929, Proc. R. Soc. A **124**, 426.
Mott, N. F., 1932, Proc. R. Soc. A **135**, 429.
Mott, N. F., and H. S. W. Massey, 1949, in *The Theory of Atomic Collisions* (Clarendon, Oxford), p. 195.
Myhra, S., and R. B. Gardiner, 1975, Radiat. Eff. **27**, 35.
Neely, H. H., and W. Bauer, 1966, Phys. Rev. **149**, 535.
Nelson, R. S., 1968, *The Observation of Atomic Collisions in Crystalline Solids* (North-Holland, Amsterdam).
Oen, O. S., 1973, ORNL–Rep. 4897.
Okuda, S., 1975, paper presented at the International Conference on the Fundamental Aspects of Radiation Damage in Metals, Gatlinburg, Tenn., USERDA Conf.–751006–Pl, p. 361.
Okuda, S., and H. Mizubayashi, 1973, Cryst. Lattice Defects **4**, 75.
Okuda, S., and H. Mizubayashi, 1975a, Phys. Rev. Lett. **34**, 815.
Okuda, S., and H. Mizubayashi, 1975b, Phys. Rev. Lett. **35**, 1043.
O'Neal, T. N., and R. L. Chaplin, 1972, Phys. Rev. B **5**, 3810.
Peretto, P., 1967, Ph.D. thesis, University of Grenoble (France).
Pruitt, A. B., and R. L. Chaplin, 1971, Radiat. Eff. **11**, 119.
Pugatscheva, T. S., 1967, Fiz. Tverd. Tela **9**, 102 [Sov. Phys.—Solid State **9**, 75 (1967)].
Pugatscheva, T. S., and I. Safarbaev, 1967, Fiz. Tverd. Tela **9**, 659 [Sov. Phys.—Solid State **9**, 508 (1967)].
Rehn, L. E., K. H. Robrock, and V. Spirič, 1975, paper presented at the International Conference on the Fundamental Aspects of Radiation Damage in Metals, Gatlinburg, Tenn., USERDA Conf.–751006–Pl, p. 234.
Rizk, R., P. Vajda, A. Lucasson, and P. Lucasson, 1973, Phys. Status Solidi A **18**, 241.
Rizk, R., P. Vajda, F. Maury, A. Lucasson, and P. Lucasson, 1977, J. Appl. Phys. **48**, 481.
Sanders, J. B., and J. M. Fluit, 1964, Physica **30**, 129.
Schaeffer, K.E., and W. Dander, 1976, Phys. Status Solidi B **78**, 139.
Seidman, D. N., K. L. Wilson, and C. H. Nielsen, 1975, Phys. Rev. Lett. **35**, 1041.
Shirley, C. G., and R. L. Chaplin, 1972, Phys. Rev. B **6**, 2027.
Silsbee, R. H., 1957, J. Appl. Phys. **28**, 1246.
Sosin, A., 1962, Phys. Rev. **126**, 1698.
Sosin, A., and W. Bauer, 1969, "Atomic Displacement Mechanisms in Metals and Semiconductors" in *Studies in Radiation Effects in Solids*, edited by G. J. Dienes (Gordon and Breach, New York), Vol. 3, p. 153.
Sosin, A., and K. Garr, 1965, Phys. Status Solidi **8**, 481.
Spirič, V., K. H. Robrock, and L. E. Rehn, 1975, paper presented at the International Conference on the Fundamental Aspects of Radiation Damage in Metals, Gatlinburg, Tenn., USERDA Conf.–751006–Pl, p. 240.
Thompson, M. W., 1969, *Defects and Radiation Damage in Metals* (Cambridge University, London).
Urban, K., 1972, J. of Microscopy **97**, 121.
Urban, K., and W. Jäger, 1975, Phys. Status Solidi B **68**, K1.
Urban, K., and A. Seeger, 1974, Phil. Mag. **30**, 1395.
Vajda, P., 1974, Fiz. Tekh. Poluprovodn. 8, 632 [Sov. Phys.—Semicond. 8, 408 (1974)].
Vajda, P., and M. Biget, 1974, Phys. Status Solidi A **23**, 251.
Vajda, P., M. Biget, A. Lucasson, P. Lucasson, 1977, J. Phys. F **7**, L123.
Varshni, Y. P., and F. J. Bloore, 1963, Phys. Rev. **129**, 115.
Vandenborre, H., L. Stals, J. Cornelis, and J. Nihoul, 1974, Radiat. Eff. **21**, 137.
Vook, F. L., H. K. Birnbaum, T. H. Blewitt, W. L. Brown, J. W. Corbett, J. H. Crawford, Jr., A. N. Goland, G. L. Kulcinski, M. T. Robinson, D. N. Seidman, and F. W. Young, Jr., 1975, "Report to the American Physical Society by the study group on physics problems relating to energy technologies: Radiation effects on materials," Rev. Mod. Phys. **47**, Suppl. No. 3.
Wenzl, H., 1970, in *Vacancies and Interstitials in Metals*, edited by A. Seeger *et al.* (North-Holland, Amsterdam), p. 353.
Wilson, W. D., L. G. Haggmark and J. P. Biersack, 1977, Phys. Rev. B **15**, 2548.
Wollenberger, H., and J. Wurm, 1965, Phys. Status Solidi **9**, 601.
Yang, C. N., 1951, Phys. Rev. **84**, 599.
Youngblood, G., S. Myhra, and J. W. deFord, 1969, Phys. Rev. **188**, 1101.